



Universität Hamburg

DER FORSCHUNG | DER LEHRE | DER BILDUNG

Enhancing the Physicochemical and Biological Properties of Anisotropic Nanoparticles by Rational Surface Engineering

DISSERTATION

Submitted in partial fulfillment of the requirements
for the degree of Doctor of Natural Sciences

(Doktor der Naturwissenschaften, Dr. rer. nat)

Department of Chemistry

Faculty of Mathematics, Computer Science and Natural Sciences

University of Hamburg

Submitted by

M.Sc. Mustafa ElGharib

Hamburg, 2020

The presented work conducted under the supervision of Prof. Dr. Wolfgang Parak and Dr. Indranath Chakraborty at Phillips University of Marburg (from April 2017 to December 2017) and at the Center for Hybrid Nanostructure (CHyN) of the University of Hamburg (from January 2018 to July 2020).

Thesis Committee:

Prof. Dr. Wolfgang Parak

Prof. Dr. Holger Lange

Evaluation Committee:

Prof. Dr. Wolfgang Parak

Prof. Dr. Volker Abetz

Prof. Dr. Wolfgang Maison

Disputation Date:

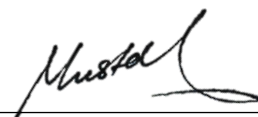
14. 08. 2020

Declaration of Authenticity

I hereby declare upon oath that I have written the present dissertation independently without assistance from external parties and have not used further resources and aids than those stated. The ideas, materials and the included work in the dissertation have not been previously submitted for grading at this or any other academic institution.

Hamburg, 08.05.2020

Place, Date



Mustafa ElGharib

List of Publications

Published manuscripts

- Zhu, L.,[#] **Gharib, M.**,[#] Becker, C., Zeng, Y., Ziefuß, A.R., Chen, L., Alkilany, A.M., Rehbock, C., Barcikowski, S., Parak, W.J. and Chakraborty, I. **Synthesis of Fluorescent Silver Nanoclusters: Introducing Bottom-Up and Top-Down Approaches to Nanochemistry in a Single Laboratory Class.** *Journal of Chemical Education* 97.1 (2019): 239-243.
- Roy, S., Liu, Z., Sun, X., **Gharib, M.**, Yan, H., Huang, Y., Megahed, S., Schnabel, M., Zhu, D., Feliu, N. and Chakraborty, I. **Assembly and Degradation of Inorganic Nanoparticles in Biological Environments.** *Bioconjugate Chemistry* 30.11 (2019): 2751-2762.
- **Gharib, M.**, Kornowski, A., Noei, H., Parak, W.J. and Chakraborty, I. **Protein-Protected Porous Bimetallic AgPt Nanoparticles with pH-Switchable Peroxidase/Catalase-Mimicking Activity.** *ACS Materials Letters* 1.3 (2019): 310-319. (Featured on the front cover)
- **Gharib, M.**, Khalaf, M., Afroz, S., Feliu, N., Parak, W.J. and Chakraborty, I. **Sustainable synthesis and improved colloidal stability of popcorn-shaped gold nanoparticles.** *ACS Sustainable Chemistry & Engineering* 7.11 (2019): 9834-9841.
- Zeng, Y., Chang, Y.H., **Gharib, M.**, Parak, W.J. and Chakraborty, I. **Understanding the Interaction of Glutamate Salts with Serum Albumin Protected Prism-Shaped Silver Nanoparticles toward Glutamate Sensing.** *Particle & Particle Systems Characterization* 36.1 (2019): 1800229. (Featured on the front cover)
- Ziefuß, A.R., Reichenberger, S., Rehbock, C., Chakraborty, I., **Gharib, M.**, Parak, W.J. and Barcikowski, S. **Laser fragmentation of colloidal gold nanoparticles with high-intensity nanosecond pulses is driven by a single-step fragmentation mechanism with a defined educt particle-size threshold.** *The Journal of Physical Chemistry C* 122.38 (2018): 22125-22136.

Submitted manuscripts

- Ziefuß, A.R., Haxhijaj, I., Müller, S., **Gharib, M.**, Gridina, O., Rehbock, C., Chakraborty, I., Peng, B., Muhler, M., Parak, W.J., Barcikowski, S., Reichenberger, S. **Radical-mediated design of surfactant-free ultra-small gold nanoparticles for catalytic applications through pulsed laser fragmentation.**

Manuscripts in preparation

- **Gharib, M.**, Galchenko, M., Klinke, C., Parak, W.J., Chakraborty, I. **Mechanistic Insights and Selected Synthetic Routes of Atomically Precise Metal Nanoclusters.**
- Zeng, Y., Havenridge, S., **Gharib, M.**, Baksi, A., Ziefuß, A.R., Strelow, C., Rehbock, C., Mews, A., Barcikowski, S., Kappes, M., Parak, W.J., Aikens, C., Chakraborty, I. **Towards Understanding the Origin of Photoluminescence: The case of Ag₂₉(DHLLA)₁₂ Nanocluster.**

- **Gharib, M.**, Gebauer, J., Kornowski, A., Nonappa, Ziefuß, A.R., Rehbock, C., Barcikowski, S., Parak, W.J. and Chakraborty, I. **Plasmonic and Fluorescent-Based Nanoassembly of Gold Nanoclusters Encapsulated Gold Nanorods Improves Their Physicochemical Properties.**
- Chen, L.,[#] Gharib, M.,[#] Zeng, Y., Parak, W.J. and Chakraborty, I. **The Biological Significance of Au@BSA Nanoclusters.**

[#] Both authors contributed equally.

Conference Contributions

In context with this work, the following contributions have been presented at conferences:

- NaNaX 9: Nanoscience with Nanocrystals, University of Hamburg, Hamburg, Germany, 17-20 September 2019. **(Poster titled as “Biocompatible Porous Bimetallic Alloy Nanozyme with pH-Switchable Peroxidase-/Catalase-Like Activity and Cargo Loading Capabilities”)**. **Website:** <https://www.chemie.uni-hamburg.de/fachbereich/veranstaltungen/nanax9/welcome.html>
- Nanotechnology in Cancer: Engineering for Oncology, Cambridge, UK: 12-14 September 2019. **(Poster titled as “Biocompatible Porous Bimetallic Alloy Nanozyme with pH-Switchable Peroxidase-/Catalase-Like Activity and Cargo Loading Capabilities”)**. **Poster Prize Award.** **Website:** <http://magazine.eacr.org/nanotechnology-in-cancer-2019-a-wonderful-platform-to-learn/>
- Translational Trends in Nanomedicine, Beilstein Nanotechnology Symposium, Ruedesheim, Germany, 17-19 September 2018. **(Poster titled as “Protein-mediated synthesis of anisotropic nanoparticles and their application as ROS scavengers”)**. **Website:** <https://www.beilstein-institut.de/symposien/archiv/nanotechnology/nano-medicine-2018>

Abstract

The unique physicochemical properties of anisotropic nanoparticles (NPs) that originate from the spatial and restricted confinement of their oscillating conduction band electrons, holes and electric fields around the characteristic anisotropic shape of such nanostructures render them potential candidates for a host of various applications including catalysis, sensing, bioimaging and different biomedical applications. Synthesis of such nanostructures usually involves the use of surfactants that function as capping agents that protect the resultant NPs from aggregation and render them colloiddally stable. These capping agents take also a part in directing the growth and hence dictating the shape of the resultant nanostructures. One of the most commonly reported capping agents is the cationic surfactant cetyltrimethylammonium bromide (CTAB) which has been used to synthesize various anisotropic NPs with different morphologies including nanorods, nanostars, nanoprisms, nanocubes, popcorn-shaped NPs, among others. It has been shown that CTAB can be cytotoxic to enormous cell types. The positively charged CTAB capping agents can bind non selectively to the negatively charged cell membranes by electrostatic interactions. Indeed, these interactions could be the primary determining factor of its cytotoxicity. At the point when CTAB interacts with the cell surfaces, it constructs blebs and holes on the cell surfaces, and ultimately leads to cell death. Therefore, the idea of this work was focused on using biocompatible ligands either as capping agent or surface passivating agent to solve the many problems associated with the hazardous nature of surface capping agents usually employed in the synthesis of anisotropic nanoparticles.

With the purpose of synthesizing highly stable and multifunctional biocompatible anisotropic NPs, this work describes the use of benign and biocompatible surface ligands in such a way they serve either as surface capping agents in order to direct the growth of different anisotropic NPs (popcorn-shaped gold (Au) NPs as well as prism-shaped bimetallic NPs) or as surface passivating agent to passivate the surface of an already synthesized gold nanorods (GNRs). In either way the resultant nanoparticles retain their physicochemical properties and gain new properties in addition to their biocompatible nature.

In this work bovine serum albumin (BSA) as biotemplate and shape-directing agent for the synthesis of anisotropic gold nanopopcorn (GNPCs) as well as porous silver-platinum (AgPt) nanoprism. The BSA-coated GNPCs exhibit the same optical and morphological properties of the

CTAB-protected nanopopcorn with more enhanced colloidal stability and biocompatibility. The BSA-coated monometallic Ag and bimetallic AgPt nanoprism retain their optical and morphological properties and gain new functionalities such as its porous structure making it a good candidate for cargo loading as well as its unprecedented pH switchable dual catalytic activity as artificial peroxidase and catalase. Moreover, the biocompatible porous nanoprism exhibit pH-responsive cargo release activity.

On the other hand, a biocompatible fluorescent gold nanocluster (GNCs) functionalized plasmonic antenna nanocomposite have been obtained via surface passivation of CTAB-protected GNRs using different silica (SiO_2) shell thicknesses. The silica layer not only passivate the surface of CTAB-protected gold nanorods (screen the noxious CTAB effects) rendering them biocompatible but also makes the GNRs amenable to post coating functionalization with a wide variety of functional groups, cross linkers and bioconjugates. The GNRs@ SiO_2 nanostructure as well as GNRs@ SiO_2 @GNCs plasmonic nanoantenna exhibit enhanced thermal and photothermal stability over the CTAB-protected GNRs besides the fluorescence behavior of the latter. Besides enhancing the photophysical and biological properties of the core GNRs, this work also describes a way of enhancing the fluorescence of GNC fluorophores by adjusting the distance between the plasmonic cores and the deposited GNCs through tuning the thickness of the silica dielectric spacer.

Zusammenfassung

Die einzigartigen physikalisch-chemischen Eigenschaften anisotroper NPs, die aus der räumlichen Beschränkung ihrer Elektronen, Löcher und elektrischen Felder im oszillierenden Leitungsband um die charakteristische anisotrope Form solcher Nanostrukturen herrühren, machen sie zu potenziellen Kandidaten für eine Vielzahl verschiedener Anwendungen wie Katalyse, Sensorik, Bioimaging und verschiedene biomedizinische Anwendungen. Bei der Synthese solcher Nanostrukturen werden in der Regel Tenside verwendet, die als Verkappungsmittel fungieren, welche die resultierenden NPs vor Aggregation schützen und sie kolloidal stabil machen. Diese Verkappungsmittel sind auch an der Steuerung des Wachstums beteiligt und bestimmen somit die Form der resultierenden Nanostrukturen. Eines der in der Literatur am häufigsten genannten Verkappungsmittel ist das kationische Tensid Cetyltrimethylammoniumbromid (CTAB), das zur Synthese verschiedener anisotroper NPs mit unterschiedlichen Morphologien verwendet wurde, unter anderem Nanostäbe, Nanosterne, Nanoprismen, Nanowürfel, popcornförmige NPs und andere. Es hat sich gezeigt, dass CTAB für viele Zelltypen zytotoxisch sein kann. Die positiv geladenen CTAB-Verkappungsmittel können sich durch elektrostatische Wechselwirkungen wahllos an negativ geladene Zellmembranen binden. Diese Wechselwirkungen könnten in der Tat der primäre Bestimmungsfaktor für ihre Zytotoxizität sein. An dem Punkt, an dem CTAB mit den Zelloberflächen interagiert, bildet es Sickerstellen und Löcher auf den Zelloberflächen, was schließlich zum Zelltod führen kann. Daher konzentrierte sich die Idee dieser Arbeit auf die Verwendung biokompatibler Liganden entweder als Verkappungsmittel oder als Oberflächenpassivierungsmittel, um die vielen Probleme zu lösen, die mit der Gefährlichkeit von Oberflächenverkappungsmitteln verbunden sind, die normalerweise bei der Synthese anisotroper Nanopartikel eingesetzt werden.

Mit dem Ziel, hochstabile und multifunktionelle biokompatible anisotrope NPs zu synthetisieren, beschreibt diese Arbeit die Verwendung von gutartigen und biokompatiblen Oberflächenliganden in einer Weise, dass sie entweder als Oberflächenverkappungsmittel dienen, um das Wachstum verschiedener anisotroper NPs (sowohl popcornförmige Au NPs als auch prismenförmige bimetallische NPs) zu steuern, oder als Oberflächenpassivierungsmittel, um die Oberfläche bereits synthetisierter Au-Nanostäbe zu passivieren. In beiden Fällen behalten die entstandenen

Nanopartikel ihre physikalisch-chemischen Eigenschaften und erhalten zusätzlich zu ihrer Biokompatibilität neue Eigenschaften.

In dieser Arbeit wurde Rinderserumalbumin (BSA) als Biotemplate und formleitendes Agens für die Synthese von anisotropem Au-Nanopopcorn sowie von porösem AgPt-Nanoprism verwendet. Das BSA-beschichtete Au-Nanopopcorn weist die gleichen optischen und morphologischen Eigenschaften wie das CTAB-geschützte Nanopopcorn auf, mit verbesserter kolloidaler Stabilität und Biokompatibilität. Die BSA-beschichteten monometallischen Ag und bimetallic AgPt-Nanoprismen behalten ihre optischen und morphologischen Eigenschaften bei und gewinnen neue Funktionalitäten, wie z.B. ihre poröse Struktur, die sie zu einem guten Kandidaten für die Drug-Delivery-Systeme macht, sowie ihre beispiellose pH-schaltbare duale katalytische Aktivität als künstliche Peroxidase und Katalase. Darüber hinaus weisen die biokompatiblen porösen Nanoprismen eine auf den pH-Wert reagierende Ladungsfreisetzungsaktivität auf.

Desweiteren, wurde ein biokompatibles fluoreszierendes Goldnanocluster (GNC) funktionalisiertes plasmonisches Antennen-Nanokomposit durch Oberflächenpassivierung von CTAB-geschützten Goldnanorod unter Verwendung verschiedener Schalenstärken von Siliziumdioxid (SiO_2) erhalten. Die Siliciumdioxidschicht passiviert nicht nur die Oberfläche der CTAB-geschützten Goldnanorods (schirmt die schädlichen CTAB-Effekte ab) und macht sie biokompatibel, sondern ermöglicht auch die Funktionalisierung der GNRs mit einer Vielzahl von funktionellen Gruppen, Vernetzern und Biokonjugaten. Sowohl die GNR@ SiO_2 -Nanostruktur als auch die plasmonische GNR@ SiO_2 @GNC-Nanoantenne weisen neben dem Fluoreszenzverhalten der CTAB-geschützten GNRs eine verbesserte thermische und photothermische Stabilität gegenüber den CTAB-geschützten GNRs auf. Neben der Verbesserung der photophysikalischen und biologischen Eigenschaften der Kern-GNRs wird in dieser Arbeit auch eine Möglichkeit beschrieben, die Fluoreszenz von GNC-Fluorophoren zu verstärken, indem der Abstand zwischen den plasmonischen Kernen und den abgeschiedenen GNCs durch die Abstimmung der Dicke des dielektrischen Siliziumdioxid-Abstandshalters angepasst wird.

TABLE OF CONTENTS

Declaration of Authenticity	i
List of Publications	ii
Conference Contributions	iv
Abstract	v
Zusammenfassung	vii
Table of Contents	ix
List of Abbreviations	xi
List of Figures	xii
Introduction	1
Chapter 1: Surface passivation of CTAB-coated GNRs using biocompatible silica shell and fluorescent GNCs	7
1.1 Introduction and aim of the work.....	7
1.2 Results and discussion.....	10
1.2.1 Characterization of GNR@CTAB, GNR@LBL@GNC, GNR@GNC and GNR@SiO ₂ @GNC.....	10
1.2.2 Colloidal stability of GNR@CTAB, GNR@LBL@GNC, GNR@GNC and GNR@SiO ₂ @GNC.....	11
1.2.3 Tuning silica shell thickness of GNRs@SiO ₂	14
1.2.4 Functionalization of GNRs@SiO ₂ with GNCs@GSH.....	16
1.2.5 Electron tomography of GNR, GNR@SiO ₂ and GNR@SiO ₂ @GNC.....	17
1.2.6 SiO ₂ shell thickness-dependent fluorescence enhancement of GNCs@GSH.....	21
1.2.7 Enhancement of thermal stability of GNRs upon silanization and coating with GNCs.....	24
1.2.8 Photothermal behavior of GNRs upon silanization and coating with GNCs.....	29
Chapter 2: BSA-directed synthesis of colloidal stable and biocompatible Au nanopopcorn	37
2.1 Introduction and aim of the work.....	37
2.2 Results and discussion.....	38
2.2.1 Characterization of NPs.....	38
2.2.2 Colloidal stability of NPs.....	47
2.2.3 Biocompatibility studies of NPs.....	51
Chapter 3: BSA-directed synthesis of porous bimetallic AgPt NPs with pH-switchable nanozyme activity and cargo loading capability	53
3.1 Introduction and aim of the work.....	53

3.2 Results and discussion.....	54
3.2.1 Characterization of NPs.....	54
3.2.2 Colloidal stability of AgPt NPs.....	70
3.2.3 Enzyme-mimic activity of AgPt NPs.....	71
3.2.4 Cargo-loading capacity of porous AgPt NPs	89
4. Conclusion and Outlook	94
5. Appendix	96
5.1 Materials	96
5.2 Characterization of NPs.....	96
5.3 Experimental Design.....	98
5.3.1 Surface passivation of CTAB-coated GNRs using biocompatible silica shell and fluorescent GNCs	98
5.3.1.1 Synthesis of GNRs@CTAB.....	98
5.3.1.2 Synthesis of fluorescent GSH-capped GNCs.....	99
5.3.1.3 Synthesis of GNRs@GNCs and GNRs@LBL@GNCs.....	99
5.3.1.4 Silanization of GNRs@CTAB.....	100
5.3.1.5 Functionalization of GNRs@SiO ₂ with GNCs.....	101
5.3.1.6 Colloidal stability studies.....	102
5.3.1.7 Evaluating plasmon-enhanced fluorescence of GNRs@SiO ₂ @GNCs as a function of distance from plasmonic GNRs	102
5.3.1.8 Evaluating the thermal stability of GNRs.....	102
5.3.1.9 Evaluating the photothermal stability of GNRs.....	103
5.3.2 BSA-directed synthesis of colloidally stable and biocompatible Au nanopopcorn	103
5.3.2.1 Synthesis of NPs.....	103
5.3.2.2 Colloidal stability Studies.....	105
5.3.2.3 Biocompatibility studies of NPs.....	105
5.3.3 BSA-directed synthesis of Porous Bimetallic AgPt NPs with pH-switchable nanozyme activity and cargo loading capability	106
5.3.3.1 Synthesis of NPs.....	106
5.3.3.2 Concentration determination of NPs.....	107
5.3.3.3 Colloidal stability studies.....	109
5.3.3.4 Peroxidase-like activity of AgPt NPs.....	109
5.3.3.5 Catalase-like activity of AgPt NPs.....	110
5.3.3.6 Cargo-loading/controlled-release into/from the AgPt NPs.....	111
5.4 List of hazardous substances used in the work.....	112
References	115
Acknowledgements	126

List of Abbreviations

NP	Nanoparticle
GNR	Gold nanorod
GNPC	Gold nanopopcorn
CTAB	cetyltrimethylammonium bromide
EDC	1-Ethyl-3-(3-dimethylaminopropyl)carbodiimide
AA	Ascorbic acid
SiO ₂	Silica
GNC	Gold nanocluster
Au	Gold
Ag	Silver
Pt	Platinum
BSA	Bovine serum albumin
PBS	Phosphate buffered saline
HeLa	Human cervical adenocarcinoma cells
FBS	Fetal bovine serum
DMEM	Dulbecco's Modified Eagle's medium Minimum
RPMI	Roswell Park Memorial Institute
LSPR	longitudinal surface plasmon resonance
TSPR	transverse surface plasmon resonance
FWHM	Full width at half maximum
UV-vis	ultraviolet–visible
TEM	Transmission electron microscopy
HRTEM	High-resolution transmission electron microscopy
CD	Circular dichroism
AR	Aspect ratio
NIR	Near-infrared
DLS	Dynamic light scattering
ICP-MS	Inductively coupled plasma mass spectrometry

List of Figures

Figure 1	Characterization of GNRs and GNRs nanocomposites.....	11
Figure 2	Colloidal stability of GNRs and GNRs nanocomposites in NaCl solution.....	13
Figure 3	Colloidal stability of GNRs and GNRs nanocomposites in biological media.....	14
Figure 4	Tuning the thickness of silica shell.....	15
Figure 5	Tuning the thickness of silica shell as a function of final CTAB concentration in GNR solution.....	16
Figure 6	Schematic illustration of the synthetic procedure of GNRs@SiO ₂ @GNCs.....	18
Figure 7	UV-vis spectra of the functionalization of GNRs with GNCs.....	19
Figure 8	TEM images of the functionalization of GNRs with GNCs.....	19
Figure 9	Characterization of GNC-functionalized GNRs@SiO ₂	20
Figure 10	3D reconstructed TEM images of GNRs.....	21
Figure 11	Plasmon-enhanced fluorescence of GNCs.....	24
Figure 12	Thermal stability of GNRs@CTAB.....	27
Figure 13	Thermal stability of GNRs@SiO ₂	28
Figure 14	Thermal stability of GNRs@SiO ₂ @GNCs.....	29
Figure 15	TEM results of the photothermal shape transformation of low AR GNRs and GNRs nanocomposites upon ns laser irradiation.....	34
Figure 16	UV-vis spectra of the photothermal shape transformation of low AR GNRs and GNRs nanocomposites upon ns laser irradiation.....	34
Figure 17	TEM results of the photothermal shape transformation of high AR GNRs and GNRs nanocomposites upon ns laser irradiation.....	35
Figure 18	UV-vis spectra of the photothermal shape transformation of high AR GNRs and GNRs nanocomposites upon ns laser irradiation.....	35
Figure 19	Retained Fluorescence properties of GNCs after irradiation of GNRs@SiO ₂ @GNCs with 9000 ns laser pulses.....	36
Figure 20	Synthesis and characterization of GNPC@BSA.....	40
Figure 21	Characterization of GNPs synthesized by different proteins other than BSA.....	41
Figure 22	Absorption spectrum of spherical GNPs formed without the use of BSA.....	41
Figure 23	UV-vis absorption spectra of GNPs formed by using different ligands other than BSA.....	42
Figure 24	TEM ad size distribution of sponge-like structures formed using CTAB of BSA.....	42
Figure 25	UV-vis absorption spectra of GNPs formed by tuning different synthetic parameters.....	43
Figure 26	Understanding the structural changes of BSA during GNPC synthesis.....	45
Figure 27	Table representing the deconvoluted protein structures from the corresponding CD spectra.....	46
Figure 28	Fluorescence emission spectra of GNPC@BSA and native BSA under different synthetic conditions.....	47
Figure 29	Effects of surface ligands on the colloidal stability of different GNPs in biological media.....	49
Figure 30	Hydrodynamic diameter (d _h) of GNPCs@BSA, GNPCs@CTAB, GNS, and GNP@citrate.....	50
Figure 31	Zeta potential of GNPCs@BSA, GNPCs@CTAB, GNS, and GNP@citrate.....	50
Figure 32	Effects of surface ligands on the biocompatibility of GNPs.....	52
Figure 33	Synthetic route and characterization of AgPt NPs.....	56
Figure 34	Characterization of the porous AgPt NPs.....	57

Figure 35	HRTEM and SAED pattern of AgPt NPs.....	58
Figure 36	Role of BSA in directing the shape towards porous prism-shaped AgPt NPs.....	59
Figure 37	Kinetics of AgPt NPs formation using different surface ligands.....	59
Figure 38	Effect of using different concentrations of Pt precursor (H_2PtCl_6) on the synthesis product.....	60
Figure 39	Effect of changing the Ag:Pt molar ratio on the NP shape and composition.....	61
Figure 40	XPS survey spectra of Ag NPs and AgPt NPs.....	62
Figure 41	Deconvolution of XPS spectra of Ag NPs@BSA and AgPt NPs@BSA.....	63
Figure 42	Characterization of AgM@BSA NPs.....	65
Figure 43	Characterization of AgPd@BSA NPs.....	66
Figure 44	Characterization of AgAu@BSA NPs.....	67
Figure 45	Effect of pH on the synthesis of AgPt NPs.....	68
Figure 46	Deconvolution of CD results.....	69
Figure 47	The structural changes of BSA during the synthesis of Ag NPs and AgPt NPs.....	70
Figure 48	Colloidal stability of Ag NPs and AgPt NPs.....	71
Figure 49	Peroxidase-like activity of AgPt NPs and steady-state kinetics of the catalytic reaction.	73
Figure 50	Peroxidase-like activity of AgPt NPs at different pH.....	74
Figure 51	Kinetics of OPD oxidation using AgPt@BSA NPs.....	75
Figure 52	Intrinsic peroxidase-like activity of AgPt NPs as a function of their elemental composition.....	76
Figure 53	Peroxidase-like activity of Ag NP@SC and AgPt@SC NPs.....	77
Figure 54	Kinetics of OPD oxidation using Ag NPs@SC and AgPt NPs@SC.....	78
Figure 55	Apparent kinetics of AgPt NPs as peroxidase mimics using different concentrations of OPD.....	80
Figure 56	Apparent kinetics of AgPt NPs as peroxidase mimics using different concentrations of H_2O_2	81
Figure 57	Catalase-like activity of AgPt NPs and steady-state kinetics of the catalytic reaction...	84
Figure 58	Catalase-like activity of Pt NPs@SC.....	85
Figure 59	Catalase-like activity of Ag NPs@SC and AgPt NPs@SC.....	86
Figure 60	Apparent kinetics of AgPt NPs as catalase mimics.....	87
Figure 61	pH-switchable catalytic activity and the selectivity of AgPt NPs in different pH environment.....	88
Figure 62	Cargo loading into porous AgPt NPs and their oxidative stress-triggered release.....	91
Figure 63	Calcein standard curve.....	92
Figure 64	Calcein loading efficiency of NPs.....	92
Figure 65	UV-vis absorption spectra of different calcein concentrations (a) before and (b) after reacting with AgPt NPs.....	93
Figure 66	Controlled release of calcein after loading AgPt NPs with different concentrations of calcein.....	93

Introduction

The term “*nano*” is derived from the Greek word “*nanos*” which means dwarf and implies very small. The nanoparticles are in principle a group of naturally-occurring or manufactured materials that have most commonly at least one dimension of approximately 1-100 nm.[1] The science that deals with the design, manipulation and applications of matter in the nanoscale size regime is called *Nanotechnology*. [2] The term *Nanotechnology* has been firstly used in the mid of 1980s by Norio Taniguchi [3] after being initially conceptualized by Richard Feynman in his famous and visionary talk “There's plenty of room at the bottom” in 1959. [4] Since then, various developments in the field of nanotechnology have been achieved.

Materials in the nanoscale size regime act distinctively in comparison with their bulk scale counterparts and exhibit unprecedented properties that have drawn much attention for centuries and extensive work on NPs have been done dates back at least to 1857 when Michael Faraday reported the first chemical synthesis of Au NPs. [5] The significance of NPs was recognized when researchers observed the great impact of the size on the physiochemical properties of a substance, such as, surface area, optical properties, chemical reactivity, mechanical, electrical and magnetic properties. For instance, metal NPs exhibit apparent tunable ultraviolet-visible (UV-Vis) extinction band(s) which largely depends on the NPs size and shape, whereas bulk metals show no extinction band in the UV-Vis region. Gold nanoparticles (GNPs) of ~100 nm diameters have a characteristic red color while gold at bulk scale is inert and has a distinctive golden color. Zhang and his colleagues found that the chemical reactivity of substances correlates to their size and their complementary surface area. [6] It is become now well known that as the size of the particle decreases, the surface area of the particles expands which in turn enhances their chemical reactivity. Moreover, the optical properties of silver and gold NPs are tunable over the visible and near-infrared (NIR) wavelengths depending on the NPs' size, shape, among others. [7] Furthermore, gold NPs likewise demonstrate orders of magnitude strong surface plasmon resonance in comparison to the strongly absorbing organic dyes which offers superior detection sensitivity of NPs-based sensors. [8] On the other hand, some metals and metal oxides NPs such as silver, iron, titanium oxide and iron oxide have antibacterial potential against various bacterium strains. [9] Such biological properties of NPs are derived from the interaction of NPs with proteins,

DNA, cell membranes, and organelles and hence the resulting protein corona, cellular uptake, as well as biocatalysis.[10]

Size control of NPs can be obtained thermodynamically, kinetically or stoichiometrically. A typical strategy for controlling NPs size is the using of capping agents, which will be adsorbed on the surface of NPs rendering them thermodynamically stable. It has been reported that changing the type of capping agent or its quantity (stoichiometry) results in the formation of NPs with different sizes. For instance, excessive amounts of dodecylthiol yield monodisperse GNPs with particle size of 4.5 ± 0.4 nm,[11] Whereas, dodecylamine generates NPs of 8.6 ± 1.3 nm with narrow size distribution.[12] NPs of smaller size could be generated via the reduction method, in this method a strong reducing agent like NaBH_4 in presence of a stabilizing agent like sodium citrate (SC) are used. Whereas larger NPs with narrow size distribution could be obtained via the seed-mediated growth.[13, 14] In this strategy, small size NPs are used as seeds and the particle growth induced through the repetitive addition of the metal precursor. Thermal decomposition of iron precursors in organic solvents in the presence of surfactant capping agents is one of the approaches used in order to generate size-controlled iron oxide nanoparticles with narrow size distribution.[15]

Nanoparticles of different sorts of shapes, such as, spherical-, rod-, star-, cubic-, popcorn-, prism-shaped NPs, among others, have been reported. The majority of reported NPs take the spherical structure. Various shapes and assemblies of NPs with particular physical, chemical and optical properties have been developed with the aid of state-of-the-art nanofabrication approaches. For example, GNRs with various aspect ratios (AR) have been reported with tunable distinctive transverse and longitudinal plasmon bands with application in surface-enhanced Raman scattering (SERS) and biomedicine[16, 17] and branched GNPs, (for instance, nanostars and nanoflower)[18, 19] with applications in electrocatalysis, chemical catalysis, SERS, and analyte sensing [20, 21]. The shape evolution of NPs could be controlled by the thermodynamics and/or the kinetics of the synthetic reaction which considered as deciding factors in determining the final shape of NPs.[20]

The shape of NPs is crucial for their proposed biological applications. For instance, GNRs with appropriate ARs have been used as novel nanocontrast agents for bioimaging and as a hyperthermia agents[22] and iron oxide-nanoworms could selectively target malignant tissues.[23] Furthermore, filament-shaped NPs could excellently avoid the nonspecific uptake by the reticulo-

endothelial system (RES), which increases the circulation time of these NPs for up to 1 week after intravenous infusion.[24]

The synthesis of different shaped nanomaterials have drawn much attention since the discovery of the helical 1D nanostructure of carbon nanotubes with their unprecedented physical and chemical properties.[25] When compared to the isotropic 0D spherical nanoparticles, the unique physicochemical properties of anisotropic NPs originate from the spatial and restricted confinement of oscillating electrons, holes and electric fields around the characteristic anisotropic shape of such nanostructures. The collective oscillation of the conduction band electrons of metallic nanostructures as a result of absorbing a quantized photon energy gives rise to the localized surface plasmon resonance (LSPR).[26] Tuning the resulting shape of nanostructures for instance from the 0D spherical GNPs to the 1D GNRs results in two different modes of interaction between electromagnetic waves and the GNRs and hence the subsequent generation of two different LSPR called transverse localized surface plasmon resonance (*t*-LSPR), corresponding to the absorption and scattering of light along the transverse direction or the short axis of the GNRs and longitudinal localized surface plasmon resonance (*l*-LSPR), corresponding to the absorption and scattering of light along the longitudinal direction or the long axis of the GNRs, the latter could be tuned by adjusting the AR of the GNRs.[27] Furthermore, tuning the shape of the nanostructures as well as the location of their plasmon peaks allow for a host of various applications including catalysis, sensing, bioimaging and various biomedical applications.[22, 28-31] For instance, tuning the AR of GNRs and therefore their *l*-LSPR band position allows for the synthesis of GNRs which can absorb light in the near-infrared (NIR) therapeutic window (also called water window) which ranges from 650 to 900 nm where light has its maximum penetration depth through biological tissues as a result of the minimum absorption of incident light by the intrinsic chromophores, such as hemoglobin and water,[32, 33] a property that could not be achieved in case of 0D spherical NPs as their plasmon resonances span only small electromagnetic wavelength range.[34] Such fine tuning properties as well as the strong absorption and scattering cross section of GNRs make them superior candidates in many bioimaging and biomedical applications.[35] Furthermore, the sharp edges or tips of anisotropic prism- and popcorn-shaped NPs exhibit unique spatial confinement of electromagnetic fields which is of enormous value for SERS applications.[34, 36] Such excellent SERS substrates with tunable plasmonic band position,

intrinsic hot spots as well as reactive facets make the anisotropic NPs superior compared to the isotropic counterparts.[34]

Synthesis of such nanostructures usually involves the use of surfactants that function as capping agents that protect the resultant NPs from aggregation and render them colloidally stable. Surface ligands of NPs play an extremely remarkable part in regulating the size and physicochemical properties of the synthesized NPs,[37, 38] serve as a guide for the assembly of NPs[39-41] and preserve their colloidal stability from surrounding ambience.[42] These capping agents take also a part in directing the growth and hence dictating the shape of the resultant NPs by preferentially adsorbing into specific crystal facets hindering their growth in a certain direction while facilitating the growth of other crystal facets. One of the most commonly reported capping agents is the CTAB cationic surfactant which has been used to synthesize various anisotropic NPs with different morphologies including nanorods, star-shaped, prism-shaped, cubic-shaped, popcorn-shaped NPs.[36, 43]

For nanobiomaterials, surface ligands play a major role in determining their cytotoxicity,[44, 45] cell penetrability[46, 47] and even their ultimate in vivo destiny.[48, 49] Because of that, the NPs can be enriched and equipped with a wide range of functionalities suitable for different applications. It has been shown that CTAB can be cytotoxic to enormous cell types,[33, 50-53] similar to the cytotoxic activity of many polycationic materials.[33] In addition, considering that CTAB is positively charged, it can bind non selectively to negatively charged cell membranes by electrostatic interactions.[54] Indeed, these interactions could be the primary determining factor of its cytotoxicity. At the point when CTAB interacts with the cell surfaces, it constructs blebs and holes on the cell surfaces, and ultimately leads to cell death.[54]

Post-synthesis surface modification of anisotropic nanostructures coated with toxic surface ligands is an essential step in order to passivate their surfaces and eliminate their cytotoxicity. This is usually achieved via ligand exchange using nontoxic surface ligands or via surface coating of the nanostructures with more benign biocompatible surface coatings, such as, consecutive polymeric layer-by-layer (LBL) coating or surface coating with natural organic matter or silica coating.[55] For instance, post-synthesis PEGylation of GNRs (i.e. ligand exchange of surface CTAB on GNRs with polyethylene glycol (PEG)) results in an abrupt reduction of the zeta-potential of GNRs which in turn delimitate the non-specific interactions with proteins and cell surfaces.[33] Usually,

NPs are cleared too quickly by RES which restrains their utility and reduces their circulation time.[56] It has been reported that the PEG modification of GNRs increases the circulation half-life of GNRs of around 1 hour.[33] Natural biomolecules such as polynucleotides, polypeptides and polysaccharides are broadly utilized for the surface modification of NPs. Compared to synthetic polymers such as PEG, polypeptides and polysaccharides offer considerably favourable attributes as they are metabolizable by digestive enzymes into harmless biomonomers, whereas synthetic polymers may be accumulated in the body which could be lethal to some extent.[57, 58] Moreover, some biocompatible polymers such as proteins display drug-loading capabilities via covalent, electrostatic and hydrophobic interactions. In addition, surface modification of protein-coated NPs is very facile because of the existence of various functional groups on the surfaces of NPs, this attributes could be utilized in different biomedical applications. Furthermore, the surfaces of NPs can also be modified by overcoating on top of already existing surface ligands, for instance previous studies have reported the LBL consecutive deposition of polyelectrolytes to passivate the surface of CTAB-capped nanostructures.[59-61]

Another alternative approach to eliminate the surface ligand-associated toxicity is the usage of biocompatible molecules as the capping and shape directing agents for the synthesis of anisotropic nanostructures without the need of the post-synthesis surface modification procedures. This synthesis approach is often referred to as the “green synthesis”, which implies the use of innocuous biomolecules, plant extracts, or microorganism for the synthesis of nanomaterials.[62, 63] A couple of different biomolecules such as peptides, proteins, polynucleotides, etc have been used for the synthesis of different shapes of nanostructures.[64-66] Such biomolecules not only offer harmless surface coatings and biocompatible nanoparticles but also can dictate the shapes of the resultant NPs thanks to their preferential adsorption sites onto the crystal facets of the metal.[67, 68]

Using biocompatible ligands either as capping agents or surface passivating agents may solve the many problems associated with the hazardous nature of surface capping agents usually employed in the synthesis of anisotropic NPs. This work aims at eliminating the environmental, ecological and nanotoxicological concerns usually associated with CTAB-protected anisotropic NPs. In an attempt to synthesize biocompatible NPs, benign and biocompatible surface ligands have been employed in such a way that they serve either as surface passivating agents to passivate the surface

of an already synthesized CTAB-coated GNRs (Chapter 1) or as surface capping agents in order to direct the growth of different anisotropic NPs such as popcorn-shaped GNPs (Chapter 2) and prism-shaped bimetallic NPs (Chapter 3). In either way the resultant NPs not only retain their original physicochemical properties of CTAB-capped NPs but also gain new properties in addition to their newly acquired biocompatible nature.

This work is divided into three chapters. In the first chapter biocompatible fluorescent GNCs-functionalized plasmonic antenna have been synthesized via surface passivation of CTAB-protected GNRs using different silica (SiO_2) shell thicknesses. The silica layer not only passivate the surface of CTAB-protected GNRs (screen the noxious CTAB effects) rendering them biocompatible but also makes the GNRs amenable to post coating functionalization with a wide variety of functional groups, cross linkers and bioconjugates. The GNR@ SiO_2 nanostructure as well as GNRs@ SiO_2 @GNCs plasmonic nanoantenna exhibit enhanced thermal and photothermal stability over the CTAB-protected GNRs in addition to the plasmon-enhanced fluorescence behavior of the latter.

The second and third chapter show how could BSA used as biotemplate and shape-directing agent for the synthesis of anisotropic GNPCs as well as porous AgPt nanoprism, respectively. The BSA-coated GNPCs exhibit the same optical and morphological properties of the CTAB-protected nanopopcorn with more enhanced colloidal stability and biocompatibility. The BSA-coated bimetallic AgPt nanoprism retain their optical and morphological properties and gain new functionalities such as its porous structure making it a good candidate for cargo loading as well as its unprecedented pH switchable dual catalytic activity as artificial peroxidase and catalase. Moreover, the biocompatible porous nanoprism exhibit pH-responsive cargo release activity.

Chapter 1: Surface passivation of CTAB-coated GNRs using biocompatible silica shell and fluorescent GNCs

1.1 Introduction and aim of the work

The fascinated optical properties of gold nanorods (GNRs) which originate from the interaction of their localized conduction band electrons with the electromagnetic radiation have gained a tremendous attention in many applications such as SERS,[69] sensing,[70] photovoltaics[71-73] as well as in many biomedical applications such as bioimaging, photothermal and photodynamic therapy (PTT and PDT), drug and gene delivery systems. Due to their many applications in the nanomedicine field, GNRs could allow for a theranostic platform which offer a simultaneous diagnostic and therapeutic tool in many diseases. The photothermal activity and effective light to heat conversion properties exhibited by GNRs allows them to be superior candidate in PTT applications. The strong absorption and scattering induced by illuminating GNRs with incident light of resonant wavelengths results in the delocalization and the collective oscillation of the free conduction band electrons of GNRs, such feature is known as the localized surface plasmon resonance. In comparison to the isotropic nanoparticles (NPs) whose electrons oscillate along one axis, the oscillation of conduction band electrons of the anisotropic GNRs occurs in two directions, along the short axis of the GNR and results in the transverse LSPR and along the long axis and results in the longitudinal LSPR. This leads to the splitting of SPR of GNRs into two extinction band one at the visible range (*t*-LSPR) and the other is tunable between visible and NIR regions of the electromagnetic spectrum (*l*-LSPR). The *l*-LSPR position could be tuned by adjusting the AR of the GNRs.[27] Tuning the AR of GNRs and therefore their *l*-LSPR band position allows for the synthesis of GNRs which can absorb light in the NIR therapeutic window (also called water window) which ranges from 650 to 900 nm where light has its maximum penetration depth through biological tissues as a result of the minimum absorption of incident light by the intrinsic chromophores,[32, 33] such as hemoglobin and water, a property that could not be achieved in case of 0D spherical NPs as their plasmon resonances span only small electromagnetic wavelength range.[34]

Synthesis of anisotropic nanostructures, such as GNRs, usually involves the use of surfactants that function as capping agents which protect the resultant NPs from aggregation and can dictate their physicochemical properties such as size, AR, surface charge, surface chemistry, etc. One of the

mostly adopted synthesis routes of GNRs is the seed-mediated method, during which large amount of the cationic CTAB surfactant is utilized as the surface capping agent.[36, 43] Several studies have reported the cytotoxicity of CTAB to various cell types,[33, 50-53] similar to the cytotoxic activity showed by many polycationic materials.[33] Moreover, the photothermal reshaping of GNRs usually occurring during laser irradiation results from the densely packed CTAB layer around GNRs which forms a protective barrier against heat diffusion that normally accompanies laser irradiation, a feature that compromises the photothermal stability of GNRs and their subsequent diminished NIR light absorption. Such drawbacks can reduce the uses of GNRs in many biological applications.

Surface passivation of CTAB-capped GNRs has been reported to reduce their cytotoxicity as well as to enhance their photothermal stability. Post-synthesis surface modification usually achieved via ligand exchange using benign surface ligands or via surface coating of the NPs with benign biocompatible surface coatings, such as, consecutive polymeric LBL coating or surface coating with natural organic matter or silica coating.[55] It has been shown that overcoating the CTAB-capped GNRs with silica passivate the cytotoxic character of CTAB and renders the GNRs more biocompatible, and enhances their drug loading capability as well as their photothermal stability.

Apart from their surface coating-induced toxicity, thermal and photothermal reshaping of CTAB-capped GNRs is another common problem during the thermal heating and laser irradiation of GNRs, respectively. When subjected to thermal heating, the structural and shape transformation of GNRs started to take place at 250° C[74] which is apparently lower than their bulk melting temperature (1064° C).[75] The thermal reshaping of GNRs is assigned to the diffusion of surface atoms from the high curvature ends of GNRs towards their low curvature side regions. Similar mechanism of curvature-driven surface diffusion of atoms[76] from the ends of GNRs towards their waist region has been proposed during photothermal reshaping, such structural deformation takes place in order to reduce the surface energies at the high-curvature ends of GNRs resulting in the gradual shape transformation into the more thermodynamically stable spherical NPs. Coating of GNRs with silica shells enhances their thermal and photothermal stability[77, 78] and allows for their easy surface functionalization with different terminal groups that dictate the hydrophilicity or hydrophobicity of GNRs.[79, 80]

Conjugation of GNRs with fluorescent moieties add another functionality to the GNRs and the combined presence of the highly light scattering GNRs and a fluorescent moiety in a single multifunctional platform is of great importance for a precise bioimaging of subcellular compartments by the dual colocalization of scattered light by dark field imaging as well as by fluorescence imaging.[81] However, two major problems facing such dual imaging platform, first is the apparent toxicity of the classical fluorescent moieties such QDs or organic dyes usually used as the fluorescent probe in fluorescence imaging, and second is the high sensitivity of such fluorescent molecules upon frequent illumination or via functionalization by surface modification which compromises their fluorescence properties.[82] Whereas, biocompatible GNCs with their bright fluorescence and non-toxic surfaces may offer a powerful alternative to the classical fluorescent probes.

This work reports the successful and facile synthesis of composite GNRs platform composed of GNCs-functionalized silica-overcoated GNRs (GNR@SiO₂@GNC) to decrease the cytotoxicity of CTAB-coated GNRs and to construct a biocompatible fluorescent GNRs system that is thermally and photothermally stable. The multifunctional composite GNRs showed enhanced colloidal, thermal and photothermal stability while retaining the original optical properties of GNRs@CTAB and the fluorescence behavior of GNCs. The photothermal as well as the fluorescence behavior of GNRs composites could be tuned by adjusting the silica shell thickness. The biocompatible GNR@SiO₂@GNC nanocomposites offer great platform for multimodal imaging, PTT and the high surface area of silica coating facilitates efficient drug loading capability. To the best of our knowledge, this is the first time to synthesize GNCs-functionalized GNRs composites taking the advantage of silica spacer of different thickness. Furthermore, the mechanism of thermal stability and photothermal reshaping of GNRs upon GNCs conjugation was studied in details.

Functionalization of GNRs@CTAB with biocompatible SiO₂ enhances the colloidal stability, photothermal stability and photothermal efficiency of GNRs. Whereas, conjugating the GNRs@SiO₂ with GNCs affects the fluorescence of conjugated GNCs as a function of SiO₂ distance and also changes the mode of photothermal reshaping of GNRs upon laser irradiation. In this work we aim at studying the colloidal stability of GNC-functionalized GNRs@SiO₂, their

thermal stability, photothermal behavior upon ns laser irradiation, as well as the silica thickness-dependent fluorescence behavior of GNC.

1.2 Results and discussion

1.2.1 Characterization of GNRs@CTAB, GNRs@LBL@GNCs, GNRs@GNCs and GNRs@SiO₂@GNCs

The GNRs@CTAB was synthesized by the previously reported seed-mediated approach where binary surfactants of sodium oleate and CTAB were used to obtain GNRs of different aspect ratios.[83] Then, the surface chemistry of the obtained GNRs@CTAB was modified using different approaches. Three different approaches were employed to find out whether they are applicable for the functionalization of GNRs with the biocompatible glutathione-capped GNCs (GNCs@GSH). Firstly, we tried to functionalize GNRs with the GNCs via the direct interaction taking the advantage of the electrostatic interaction between the positively charged surfaces of GNRs@CTAB (ζ -potential $\sim +18$ mV) and the negatively charged GNCs@GSH (ζ -potential ~ -15 mV). The LBL technique has been also employed to incorporate the GNCs to the GNRs by overcoating the GNRs by a negatively charged polyelectrolyte layer of poly(styrene sulfonate) (PSS) followed by a layer of the positively charged poly(diallyldimethylammonium chloride) (PDADMAC) and then incubated with the GNCs. However, these approaches did not yield effective and homogeneous distribution of GNCs around the GNRs cores (Figure 1). Therefore we decided to firstly overcoat the CTAB-capped GNRs with silica layer and then to conjugate the GNCs to the SiO₂ layer via EDC chemistry. The transmission electron microscopy (TEM) images reveal an effective and homogeneous distribution of the GNCs@GSH around the silica-coated GNRs (Figure 1). The UV-vis spectra of GNRs@SiO₂@GNCs did not show aggregation neither any broadening of the peak, whereas a significant broadening of GNRs@GNCs as well as GNRs@LBL@GNCs was observed compared to that of GNRs@CTAB (Figure 1).

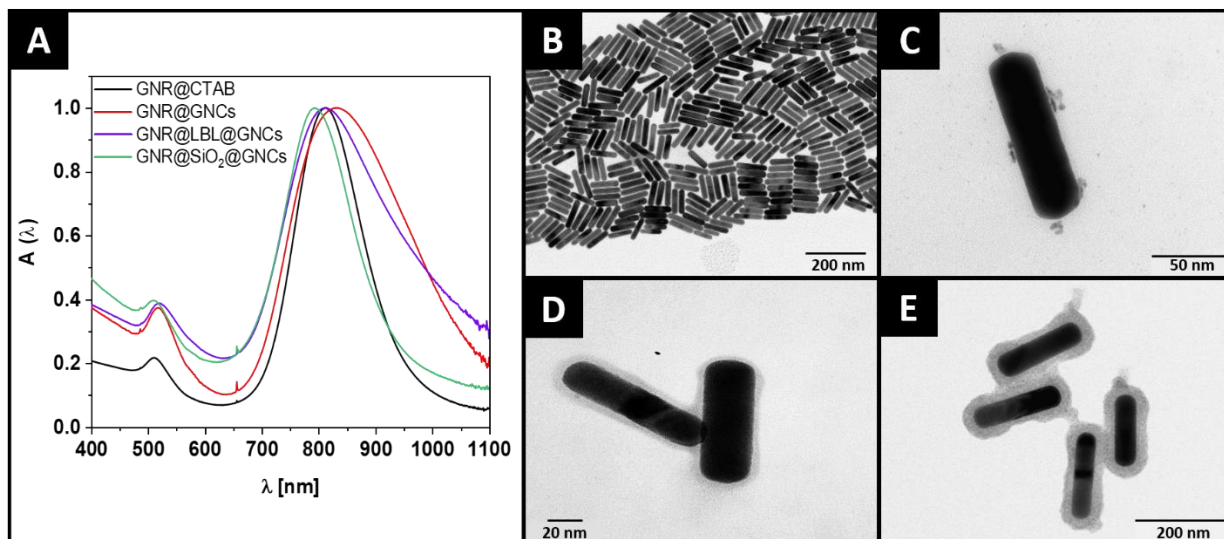


Figure 1. Characterization of GNRs and GNRs nanocomposites. A) UV-vis spectra of GNRs@CTAB, GNRs@GNCs, GNRs@LBL@GNCs, and GNRs@SiO₂@GNCs and (B-E) their corresponding TEM images, respectively.

1.2.2 Colloidal stability of GNRs@CTAB, GNRs@LBL@GNCs, GNRs@GNCs and GNRs@SiO₂@GNCs

As the colloidal stability of nanostructures is a determinant factor for their applicability in diverse applications especially for biomedical applications, the colloidal stability of GNRs@CTAB, GNRs@GNC, GNRs@LBL@GNCs, and GNRs@SiO₂@GNCs in sodium chloride (NaCl) solutions of different ionic strength as well as in different biological media was studied. As could be seen from (Figure 2), GNRs@SiO₂@GNCs are colloiddally stable when incubated with NaCl solution of different ionic strength for up to 24 h, whereas GNRs@CTAB started to aggregate after 6 h incubation in relatively higher concentration of NaCl (~ 600 mM) and start to lose their characteristic LSPR after 24 h. The GNRs@GNCs showed instant broadening of the LSPR peak as well as very poor colloidal stability after 6 h incubation with NaCl and completely lose their plasmonic peaks after 24 h of incubation. The GNRs@LBL@GNCs although exhibiting aggregations at relatively higher NaCl ionic strength after incubation for 6 h and 24 h, they still retain their optical properties at lower concentrations of NaCl. This results showed that silica and polyelectrolyte layers overcoating render the GNRs more colloiddally stable by reducing their aggregation susceptibility, this effect may be ascribed to the passivation of the CTAB layer and shielding of the GNRs core when overcoated with either silica or polyelectrolyte layers. The

positively charged CTAB-coated GNRs may have been probably electrostatically interacted with the negatively charged Cl^- ions leading to either crosslinking of GNRs or their complete surface neutralization and hence their subsequent aggregation.

Furthermore, the colloidal stability of GNRs@CTAB as well as the other nanocomposites was evaluated in different biological media such as phosphate-buffered saline (PBS), fetal bovine serum (FBS)-free/supplemented DMEM, and FBS-free/supplemented RPMI cell culture media. The UV-vis spectra of GNRs@SiO₂@GNCs showed almost no obvious optical changes with no evidence of aggregation or hypsochromic or bathochromic shift of the local surface plasmon band (Figure 3) which reflects their excellent colloidal stability in different biological media even after 24 h incubation period. GNRs@GNCs showed also similar colloidal stability during their incubation in different biological media. On the other hand, the UV-vis spectra of the GNRs@LBL@GNCs started to broaden after 6 h of incubation in biological media and the SPR bands become wider after 24 h of incubation. It was very obvious that CTAB-coated GNRs showed very poor colloidal stability in biological media and broadening of the SPR peaks takes place instantly right after incubation in such media. The GNRs@CTAB started to lose their characteristic plasmonic peaks only after 6 h of incubation and could not withstand such conditions. It could be concluded that passivation of the GNRs@CTAB via their surface modification could enhance their colloidal stability making them more robust in relatively harsher conditions.

Taking the TEM and colloidal stability results together, one could infer that overcoating the GNRs@CTAB with silica layer not only allows homogeneous and effective functionalization with the GNCs but also significantly enhances the colloidal stability of the resultant nanocomposites. On top of that it has been shown that coating the NPs with the silica dielectric spacer renders them biocompatible[84-87] and facilitates their functionalization with various silanes.[88]

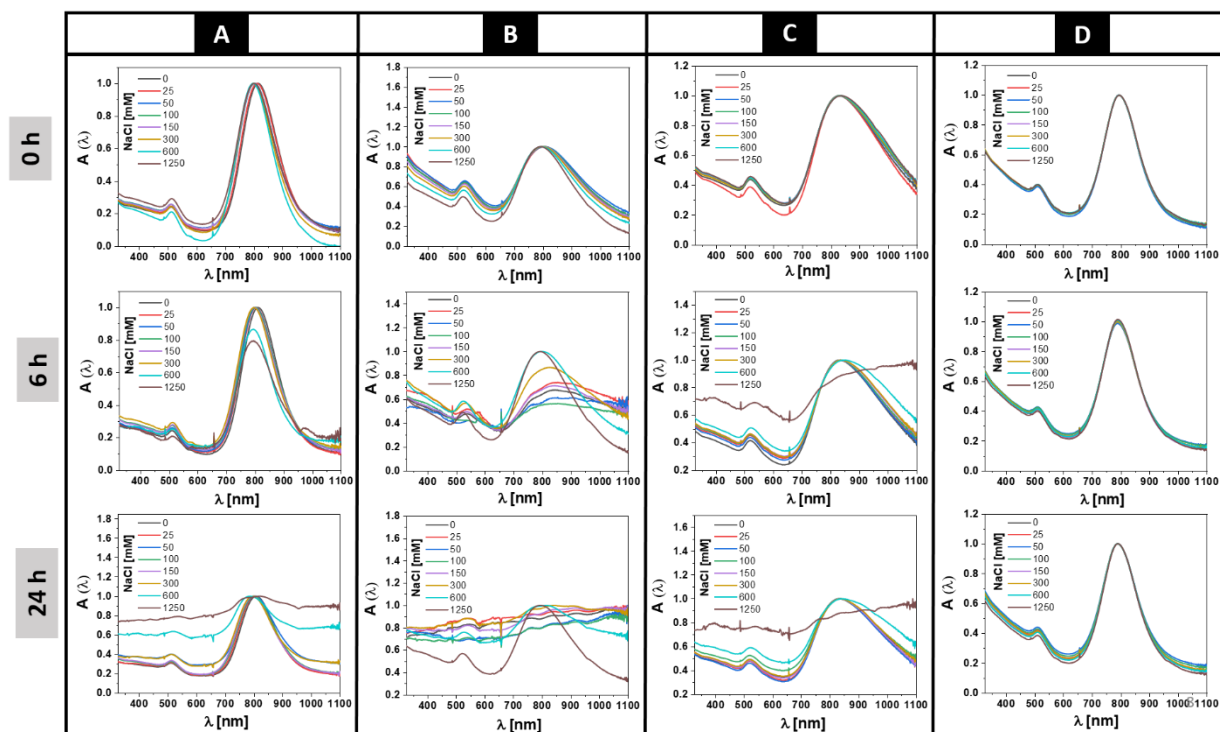


Figure 2. Colloidal stability of GNRs and GNRs nanocomposites in NaCl solution. UV-vis spectra of A) GNRs@CTAB, B) GNRs@GNCs, C) GNRs@LBL@GNCs, and D) GNRs@SiO₂@GNCs after incubation with NaCl solution of different ionic strength at 0h, 6h, and 24h.

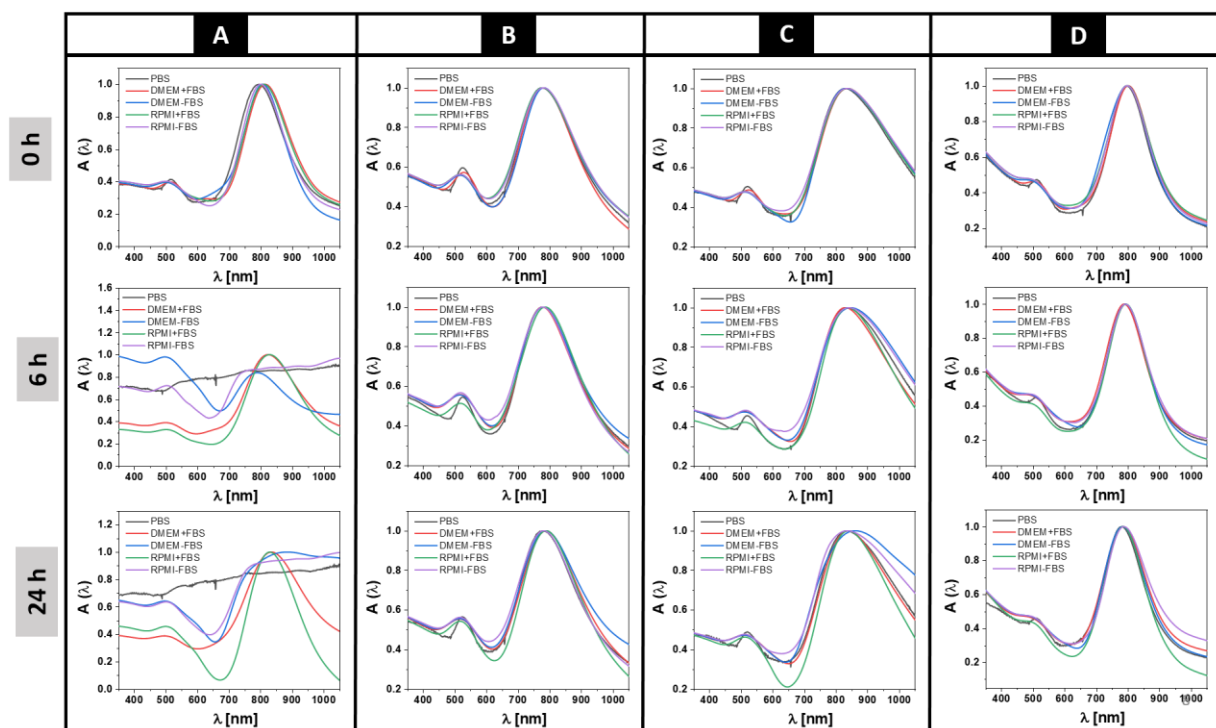


Figure 3. Colloidal stability of GNRs and GNRs nanocomposites in biological media. UV-vis spectra of A) GNRs@CTAB, B) GNRs@GNCs, C) GNRs@LBL@GNCs, and D) GNRs@SiO₂@GNCs after incubation with different biological media at 0h, 6h, and 24h.

1.2.3 Tuning silica shell thickness of GNRs@SiO₂

Based on the great and homogenous covering of silica-coated GNRs with GNCs as well as their enhanced colloidal stability compared to GNRs@CTAB, GNRs@GNCs, and GNRs@LBL@GNCs we decided to investigate the role of tuning the silica shell thickness on different physicochemical properties of GNRs and GNCs in the GNRs@SiO₂@GNCs nanocomposites. Therefore, GNRs with different SiO₂ thicknesses have been synthesized using a modified Stöber process.[89] Tuning the silica thickness was initiated by controlling the CTAB concentration in the as-synthesized GNRs. This was simply done by removing the excess CTAB from the system by centrifugation leaving behind a minimum amount of CTAB that stabilizes the GNRs. The CTAB concentration was then adjusted by the subsequent addition of different amount of CTAB that allowed to equilibrate on the surface of GNRs such as to bring the final CTAB concentration below or well close to the critical micelle concentration of CTAB (0.90–0.98 mM)[90] which is very crucial for coating the GNRs with silica shells of different thickness. [89]

The silica deposition initiated by the base-catalyzed hydrolysis and the subsequent condensation of the silica tetralkylsilicates precursor, tetraethylorthosilicate (TEOS), on the CTAB micelles which serve as the organic template for silica deposition and are mostly surround the GNRs surfaces. The equilibrated CTAB micelles as a function of added CTAB in the previous step controls the silica shell thickness.[88, 89, 91] Using this highly reproducible method, GNRs functionalized with different silica shell thicknesses ranging from approximately 8-30 nm were successfully obtained (Figure 4 C-D and 5). The UV-vis spectra of GNRs functionalized with different silica thickness do not exhibit aggregation or broadening of the LSPR peaks and retain almost the same full width at half maximum (FWHM) values of CTAB-coated GNRs (Figure 4). However, small blue shift is observed after the functionalization with silica shell which is attributed to the changes in refractive index accompanied with CTAB removal after purification of silica-coated GNRs with methanol which diffuses through the mesoporous structure of silica and dissolves the CTAB coating that templates the silica deposition.[92]

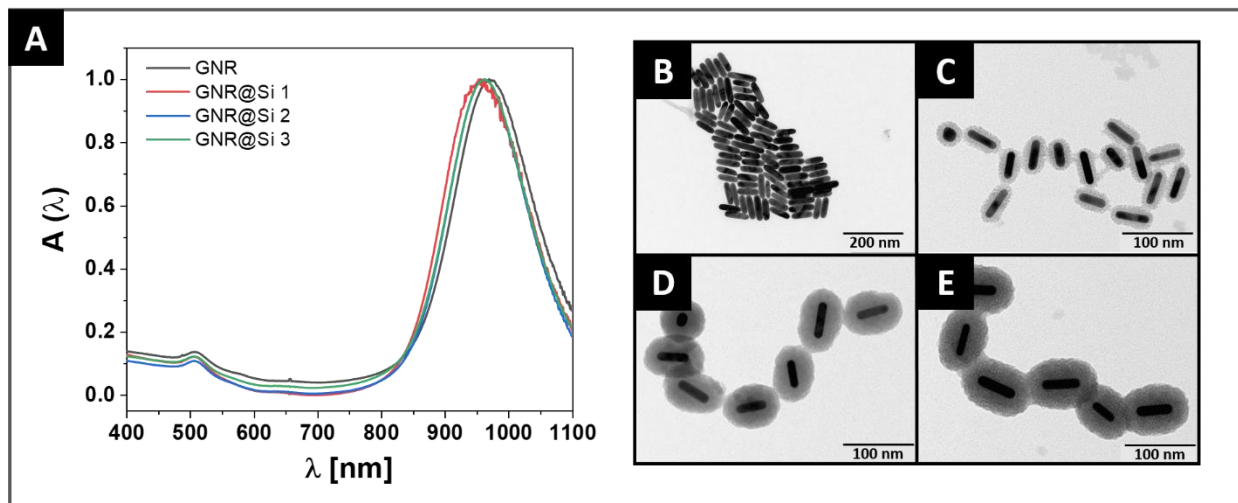


Figure 4. Tuning the thickness of silica shell. A) UV-vis spectra of GNRs@CTAB and GNRs@SiO₂ of different thickness (Si1= 8 nm, Si2= 23 nm, and Si3= 30 nm) and (B-C) their corresponding TEM images.

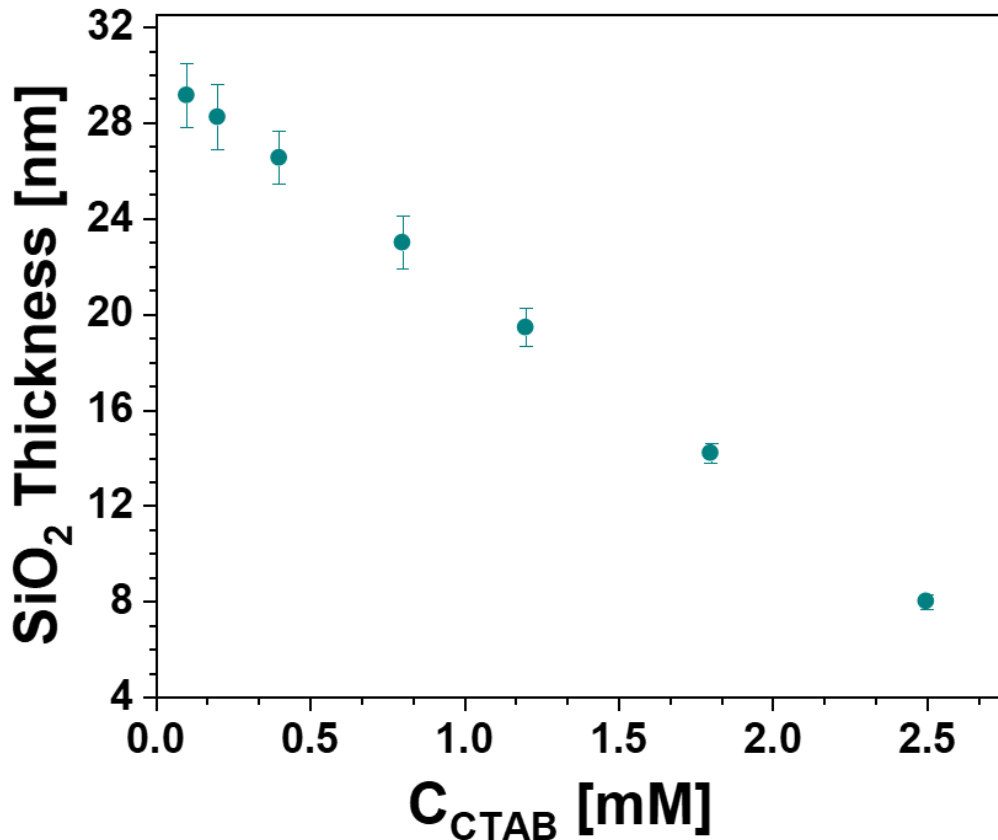


Figure 5. Tuning the thickness of silica shell as a function of final CTAB concentration in GNR solution.

1.2.4 Functionalization of GNRs@SiO₂ with GNCs@GSH

Silica-coated GNRs were then conjugated with GNCs@GSH in order to study the effect of such functionalization on the photophysical properties of both GNRs and GNCs. The conjugation of silica-coated GNRs with GNC@GSH was carried out through two steps (Figure 6 A-E). The SiO₂-coated GNRs was firstly interacted with the 3-aminopropyl triethoxysilane (APTES) to introduce amine groups to the surface of the GNRs. The free carboxylic groups of GSH-capped GNCs were activated through the EDC chemistry and made ready to interact with primary amine groups of the APTES-functionalized silica-coated GNRs. The GNCs@GSH were conjugated to the silica-coated GNRs via amide bond formation through the nucleophilic attack of primary amino groups on the activated carboxyl groups of GSH-capped GNCs with the release of carbodiimide crosslinker as by-product. The successful functionalization with APTES and GNCs could be followed by

observing the changes in zeta potential. The zeta potential of silica-coated GNRs is approximately -10 mV which turns into approximately +9 mV after conjugation with APTES that subsequently changed into -6 mV upon deposition of GNCs (Figure 6E). The UV-vis spectra of GNCs-functionalized GNRs@SiO₂ revealed the retained plasmonic bands of the original GNRs with a small broadening of the LSPR band (Figure 7). Furthermore, The TEM images show the successful conjugation of silica-coated GNRs with GSH-capped GNCs (Figure 8). Our conjugation strategy shows a uniform and homogeneous distribution of the GNCs around the GNRs of different silica thicknesses. The HR-TEM images of GNRs@SiO₂@GNCs show the homogeneous distribution and high loading of the well monodisperse GSH-coated GNCs of 1.8±0.35 nm average core diameter with a measured d-spacing between lattice fringes of 0.235 nm which is in a well agreement with reported values[93], indicating the retained original crystallinity of GSH-coated GNCs (Figure 9). The energy-dispersive X-ray (EDX) mapping of GNRs@SiO₂@GNCs showed the uniform silica deposition around the GNR core and the exclusive and preferential deposition of GSH-coated GNCs at the outer surfaces of the silica shell as could be revealed from the Au elemental distribution in the nanohybrid system (Figure 9).

1.2.5 Electron tomography of GNRs@CTAB, GNRs@SiO₂ and GNRs@SiO₂@GNCs

Due to the limitation of the traditional 2D TEM imaging and thus the difficulty to judge the spatial distribution of GNCs specially that bound to the top and bottom sides of the GNRs in the image plane, STEM tomography reconstruction (3D TEM) was carried out in order to gain more insights into the spatial distribution and assembly of GSH-coated GNCs on the GNRs@SiO₂ surfaces. The 3D imaging was performed through the acquisition of various 2D TEM images at different tilt angles and then the 3D images are reconstructed thereof. The electron tomography images of GNRs@SiO₂@GNCs clearly show the uniform and even distribution of GNCs on the silica coating of the GNRs without preferential deposition onto the sides or the tips of GNRs and not within the porous structure of the mesoporous silica shells (Figure 10). This means that the GNCs are loaded at even and same distance from the surfaces of the plasmonic GNRs. Moreover, 2D and 3D TEM images revealed the monolayer GNCs shell structures of the GNRs@SiO₂@GNCs nanocomposites (Figure 10). As thus, our conjugation strategy could be simply applied to deposit

a monolayer of any carboxyl-group functionalized noble metal nanocluster to silica-coated plasmonic GNRs.

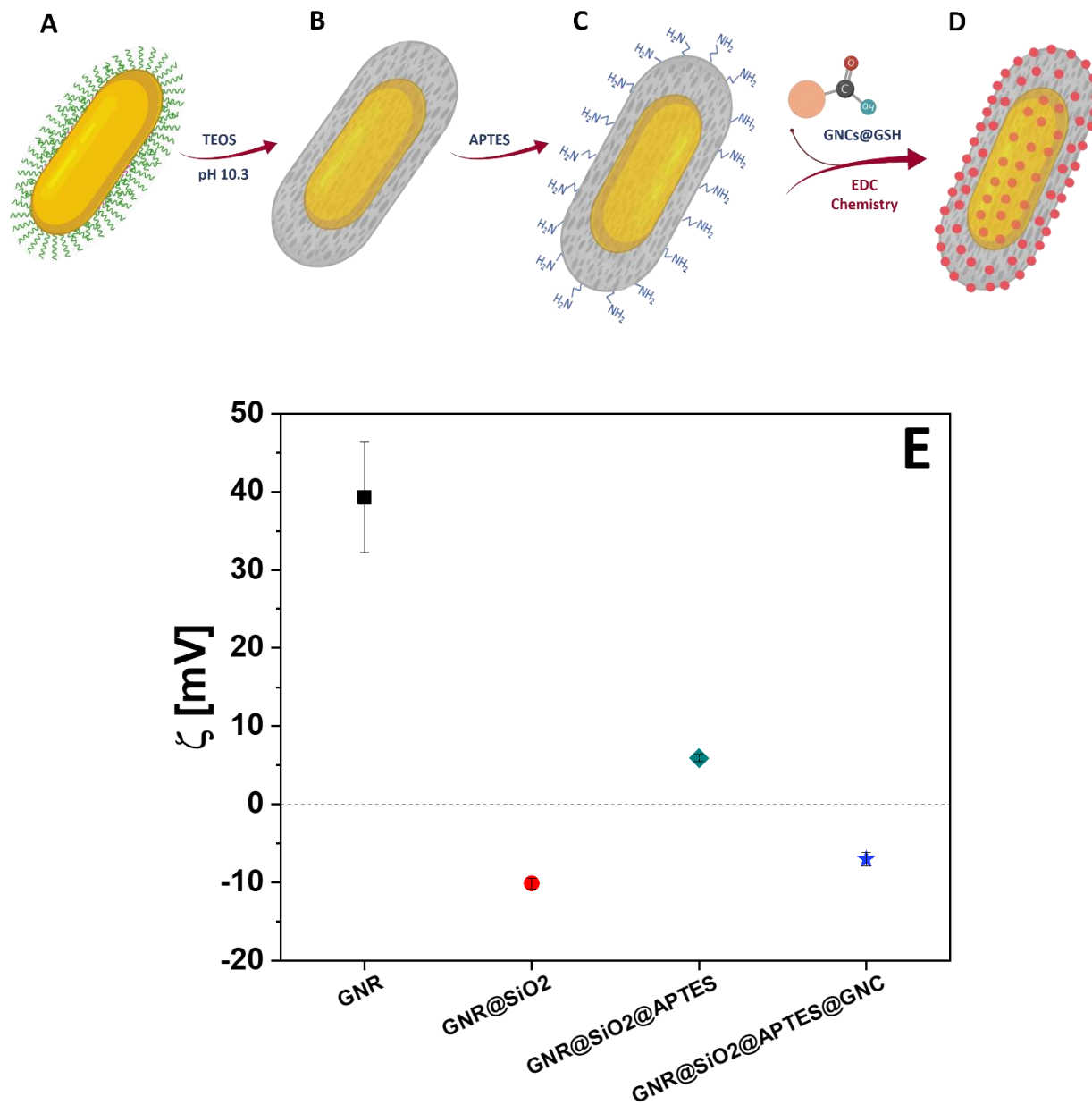


Figure 6. Schematic illustration of the synthetic procedure of GNRs@SiO₂@GNCs. A) GNRs@CTAB, B) GNRs@SiO₂, C) APTES-functionalized GNRs@SiO₂, and D) GNRs@SiO₂@GNCs. E) Development of Zeta potential (ζ) of GNRs during different functionalization steps.

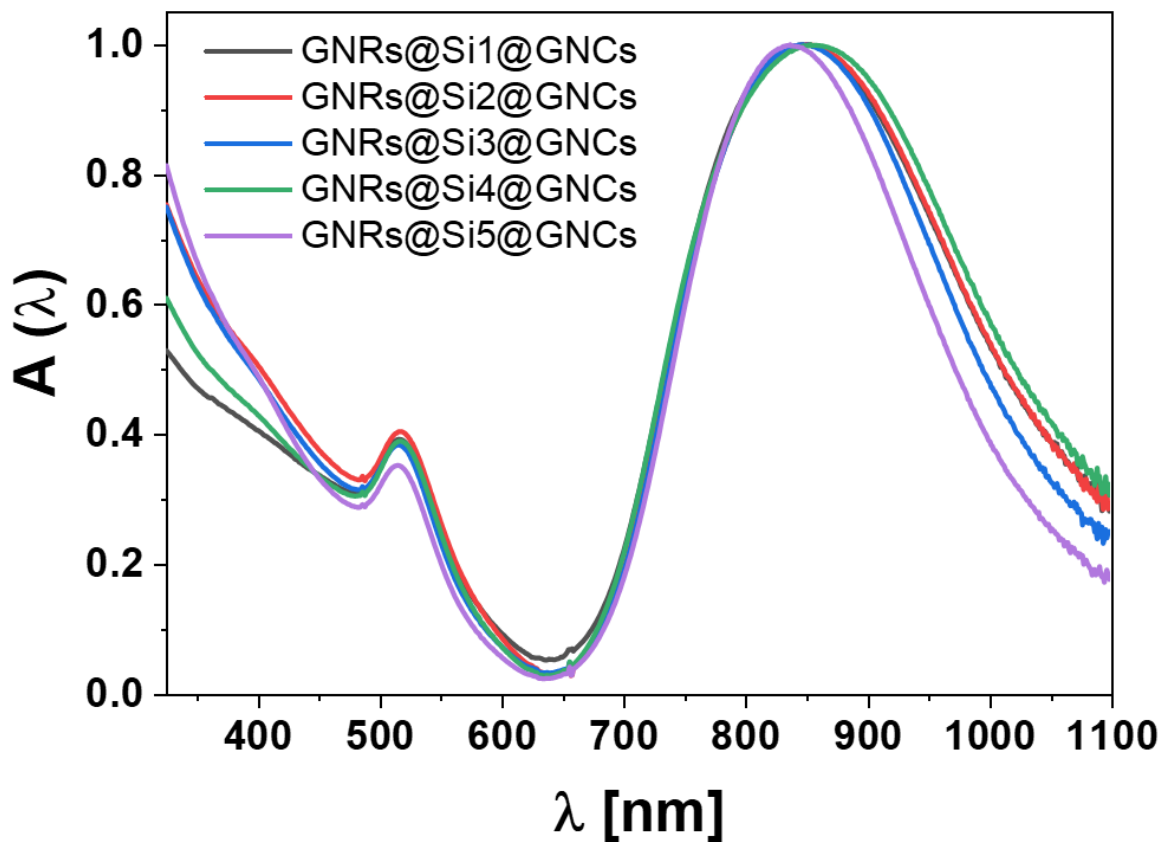


Figure 7. UV-vis spectra of the functionalization of GNRs with GNCs. UV-vis spectra of GNCs-functionalized GNRs@SiO₂ of different silica thickness.

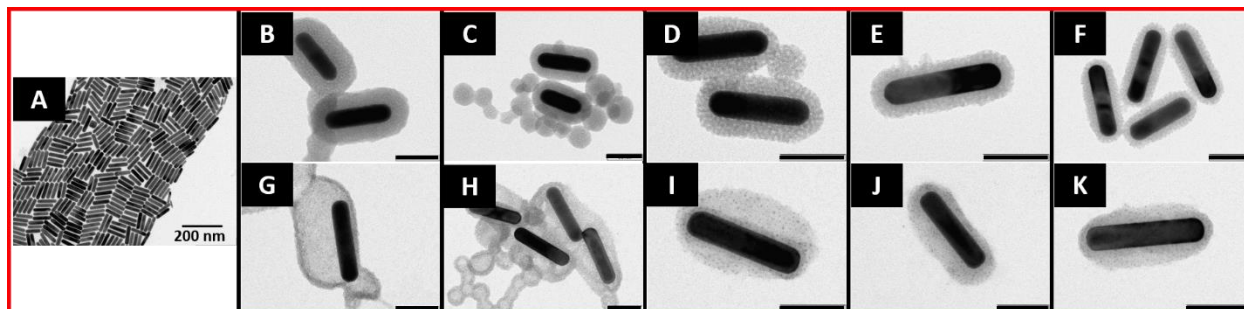


Figure 8. TEM images of the functionalization of GNRs with GNCs. TEM images of A) GNRs@CTAB, B-F) GNRs@SiO₂ of different thickness and their corresponding TEM images after functionalization with GNCs. (Scale bar in B-K= 50 nm).

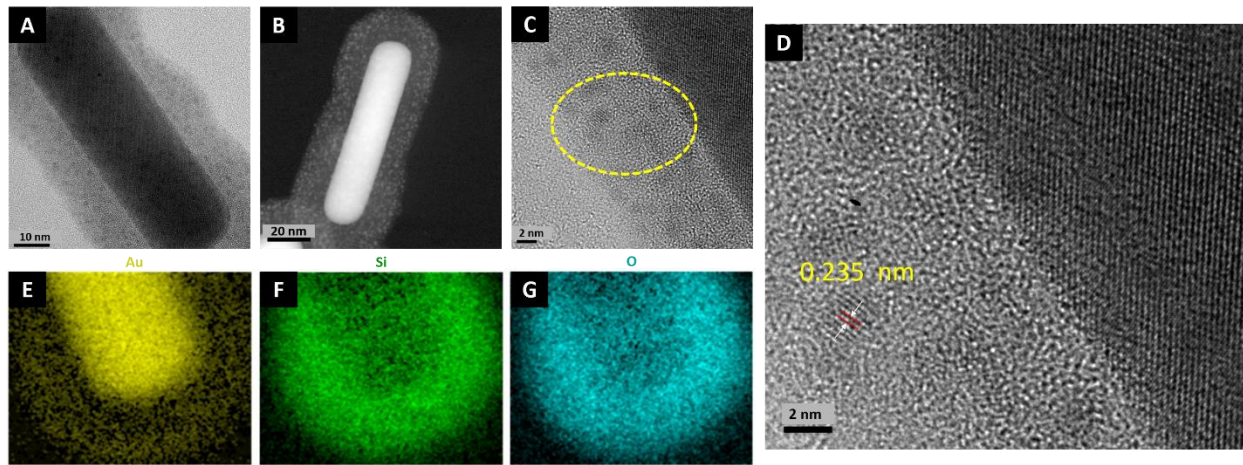


Figure 9. Characterization of GNCs-functionalized GNRs@SiO₂. TEM (A and C) and STEM (B) of GNRs@SiO₂@GNCs. (D) HRTEM of the outlined area in (C) showing the *d*-spacing of Au of the deposited GNCs in GNRs@SiO₂@GNCs. (E-G) EDX elemental mapping of Au, Si, and O in GNRs@SiO₂@GNCs. (Scale bar in E-G= 25 nm).

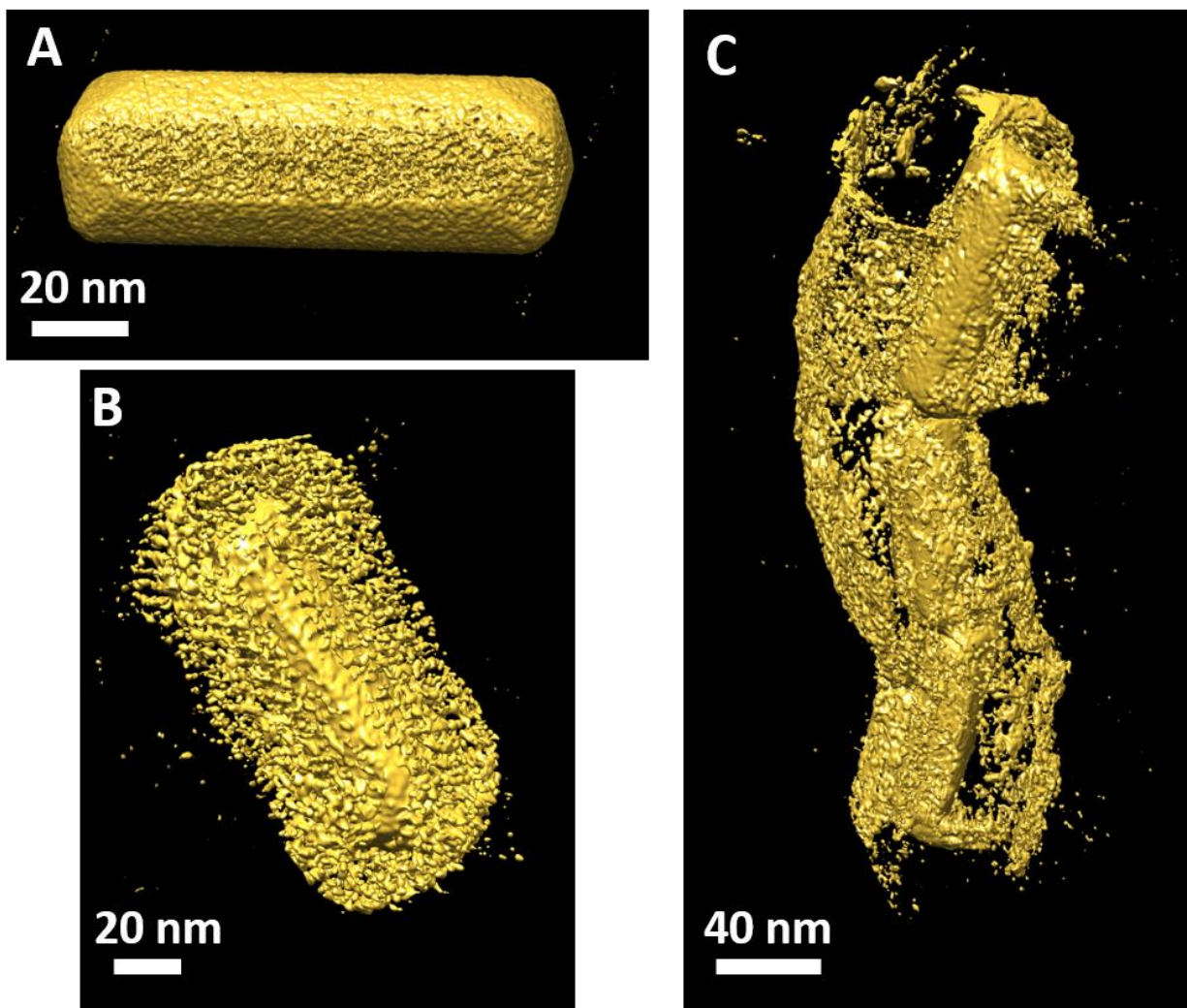


Figure 10. 3D reconstructed TEM images of GNRs. Electron tomography of A) GNRs@CTAB, B) GNRs@SiO₂, and C) GNRs@SiO₂@GNCs.

1.2.6 SiO₂ shell thickness-dependent fluorescence enhancement of GNCs@GSH

It has been reported that the excitation and emission of a fluorophore could be tuned near the surfaces of plasmonic NPs.[94, 95] The plasmon-enhanced fluorescence of a fluorophore could arise either from higher excitation rates of the fluorophore due to the strong local electromagnetic field at the plasmonic surfaces or from the enhanced emission of the fluorophore due to the enhancement of the radiative decay rates of the electromagnetically-coupled fluorophore, or from both processes.[96-98] It has been reported also that the photophysical properties such as optical absorption and scattering of the plasmonic nanostructures could affect the radiative decay rates of the coupled fluorophore and hence their fluorescence properties in a plasmonic nanoparticle-

fluorescent emitter coupled systems.[97] The plasmon-enhanced fluorescence of a fluorophore is a distant-dependent process and the fluorescence enhancement takes place when the fluorophore is at certain distant from the surface of the plasmonic nanostructure where fluorescence resonance energy transfer (FRET) to the plasmon is minimal and the generated electric field at the plasmonic surface still contributes to the excitation ad/or emission enhancement of the fluorophore.[94, 99] When the FRET is much higher than the enhancement of excitation ad/or emission processes then quenching of the fluorophore takes place.[89]

Despite the tremendous efforts that have been devoted to study the plasmon-enhanced fluorescence of organic dyes, inorganic fluorophores such as QDs,[96, 97, 100-114] and fluorescent proteins,[115] there has been no reports, to the best of our knowledge, that discussed the distant-dependent fluorescence behavior of GNCs upon coupling with plasmonic GNRs using the silica shell dielectric spacer.

Therefore, the fluorescence behavior and emission intensity of GSH-capped GNCs were studied as a function of their distance from the surfaces of GNRs. Firstly, GNRs coated with silica shells of different thicknesses (approximately 21-29 nm) were prepared and subsequently functionalized with the GNCs. Then, the distance from plasmonic GNRs-dependent fluorescence enhancement or quenching of GNCs fluorophore was studied using fluorescence spectroscopy. The fluorescence spectroscopy results showed a distant-dependent fluorescence enhancement of GNCs with the GNCs placed at ca. 25.6-26.5 nm exhibiting the maximum fluorescence enhancement (Figure 11). The emission spectra revealed that the fluorescence enhancement of GNCs takes place without any concomitant alteration in the spectral profile of the emission spectra as could be reflected by the fixed emission maxima at approximately 600 nm as well as the unchanged emission color (Figure 11). Such behavior is of important value in bioimaging applications where more than one fluorophore are employed, as a change in the spectral profile of one fluorescence emitter could interfere with the other emitters. Moreover, the distant-dependent fluorescence enhancement follows a nonmonotonic trend where the fluorescence intensity increases to a maximum at a silica spacer thickness of 25.5 nm and then drops back at longer GNCs-GNRs separation distance (Figure 11 B and C). Such nonmonotonic trend is explainable as follows, the GNCs experience on one hand a profound nonradiative quenching at small GNCs-GNRs separation distance[116] and on the other hand the strong electric field near the surfaces of the plasmonic GNRs decays

exponentially as a function of distance from the GNRs hotspots,[89] these are two competing processes and whether enhancement or quenching of the fluorescence is a trade-off between the spontaneous decay rate enhancement due to the plasmon-induced enhanced electric field and the quenching nonradiative decay rates. As such, a maximum plasmon-induced fluorescence enhancement takes place when the spontaneous decay rate increase outweighs the nonradiative quenching. [116] Decreasing the SiO₂ shell thickness and therefore the gap between the GNCs and the plasmonic surfaces leads to a decrease in the emission intensity of the GNCs this could be explained by increased nonradiative decay rates as GNCs get closer to the continuum states of the plasmonic nanostructure.[89] It is worth noting that the silica coating itself does not significantly contribute to enhancement of fluorescence as it is well known that the silica shells largely modulate the electric field up to 10 nm near the plasmonic NPs and this effect is very low past the 10 nm.[117, 118]

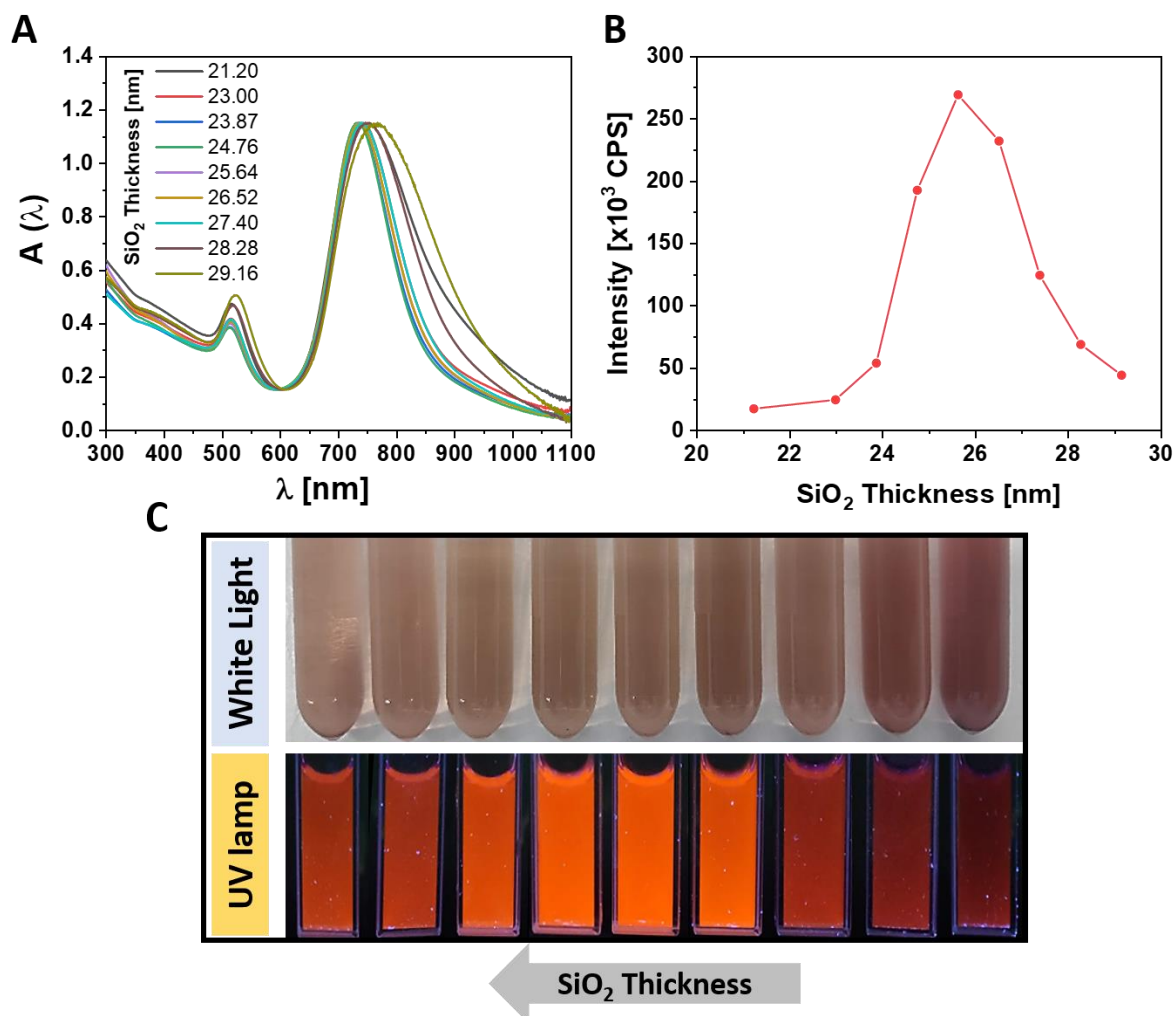


Figure 11. Plasmon-enhanced fluorescence of GNCs. A) UV-vis spectra of GNCs-functionalized GNRs@SiO₂ of different thickness. B) Enhanced fluorescence intensity of GNCs as a function of SiO₂ thickness and distance from plasmonic surface. C) Photographs of GNRs@SiO₂@GNCs of different SiO₂ thickness under white light and UV lamp.

1.2.7 Enhancement of thermal stability of GNRs upon silanization and coating with GNCs

Functionalization of SiO₂-coated GNRs with GNCs not only enhances the photophysical properties of the GNCs as mentioned earlier but also could affect the physical properties of the plasmonic GNRs cores. It has been reported that the thermal heating of GNRs causes abrupt morphological and structural alterations of the GNRs until reaching a nanostructure with more stable crystal facets of low surface energy.[119] Various studies have shown that heating of

anisotropic nanostructures either by using thermal heating or laser irradiation deform such NPs into more rounded nanostructures which in turn limits their intended applications where the morphology and thus the optical properties needed to be preserved.[76, 120, 121] There have been some studies where TEM imaging has been used to analyze the structural and morphological transitions of NPs during the melting process.[122-124] Moreover, the in-situ TEM has been used very often to study the surface melting of metallic NPs.[125, 126]

We performed the in situ TEM heating using a TEM facility equipped with a heating holder to heat the specimens at different temperatures in order to detect the heat-induced morphological and structural changes of GNRs@CTAB, GNRs@SiO₂ and GNRs@SiO₂@GNCs. The in situ heating experiment was performed at different temperature in temperature range of 100-1000° C and the TEM images were taken after approx. 60 min dwell time at a given temperature. The in situ heating experiments of GNRs@CTAB revealed unchanged morphology of the GNRs below 150° C and the GNRs preserved their original AR of approx. 3.5. Once the temperature increases to 150° C, morphological transformations of GNRs start to take place as could be seen from the fusion and coalescence of the GNRs (Figure 12C). As the temperature goes up more structural rearrangements, distortions and crystal annealing of the GNRs take place and more irregular shapes start to appear (Figure 12D). The nearly complete morphological transformation from rod-shaped into spherical-shaped NPs takes place at 250° C, which is hundreds of degrees well below the bulk gold melting temperature (approx. 1064° C). Similar results for in situ thermal-induced transformations have been previously reported.[75] On the other hand, our in situ TEM heating results revealed enhanced thermal stability of GNRs upon coating with mesoporous silica (Figure 13). The TEM images of silica-coated GNRs did not show significant morphological changes and could resist the thermal heating-induced structural rearrangement up to a heating temperature of 850° C. Moreover, functionalization of silica-coated GNRs with GNCs did not change the thermal behavior and thermal stability of the nanocomposite. The TEM images of GNRs@SiO₂@GNCs preserved the intact anisotropic shape of the GNRs up to a temperature as high as 850° C and the morphological changes start to appear as the heating temperature elevated to 900-1000° C (Figure 14), at such high temperature which is close to the bulk gold melting temperature some of the GNRs transformed into prolate spheroid- and Φ -shaped NPs, though a complete transformation of the GNRs still did not take place at such higher temperature. To our surprise, at elevated temperatures (800-1000° C) the deposited GNCs did not exhibit significant structural changes and

showed superb thermal stability, though some coalescence of individual GNCs start to take place at 800° C. It has been shown that the melting temperature of gold nanocrystals decreases as the particles size decreases[127] and some studies determined a melting temperature of as low as 127° C for nanoclusters with diameter of less than 2 nm.[123, 128] As such, the thermal-induced melting of GNRs@CTAB takes place at lower temperatures and well hundreds degrees below the bulk gold melting temperature, this could be attributed to the inability of the organic CTAB layer to prevent the thermal-driven diffusion of the less stable surface atoms from the regions of high curvatures (tips of the GNRs) towards the side faces of the GNRs (shaft of GNRs), such thermally-driven structural rearrangement process will continue until reaching the thermodynamically more stable nanostructures (spherical NPs). Hence, the enhanced thermal stability of GNRs@SiO₂ and GNRs@SiO₂@GNCs over the pristine GNRs could be ascribed to the ability of the inorganic silica coating and GNCs to act as barrier or protecting layers against the thermally-driven reshaping phenomenon. The ability of the protective layers of silica and GNCs to inhibit the thermal diffusion of surface atoms and hence the reshaping of GNRs could be explained by different mechanisms; 1) the insulation/passivation effect of the layers so that less temperatures could reach the GNRs cores, 2) the enhanced thermal conductivity of the silica and GNCs layers compared to CTAB makes them way effective in releasing the heat deposited on the GNRs during the thermal heating process, 3) the thick silica shells could work as highly rigid layers that hinders the surface diffusion of gold atoms and hence the morphological transformations of GNRs and therefore melting the silica-coated GNRs requires higher temperature than that needed to melt micelle-stabilized GNRs.

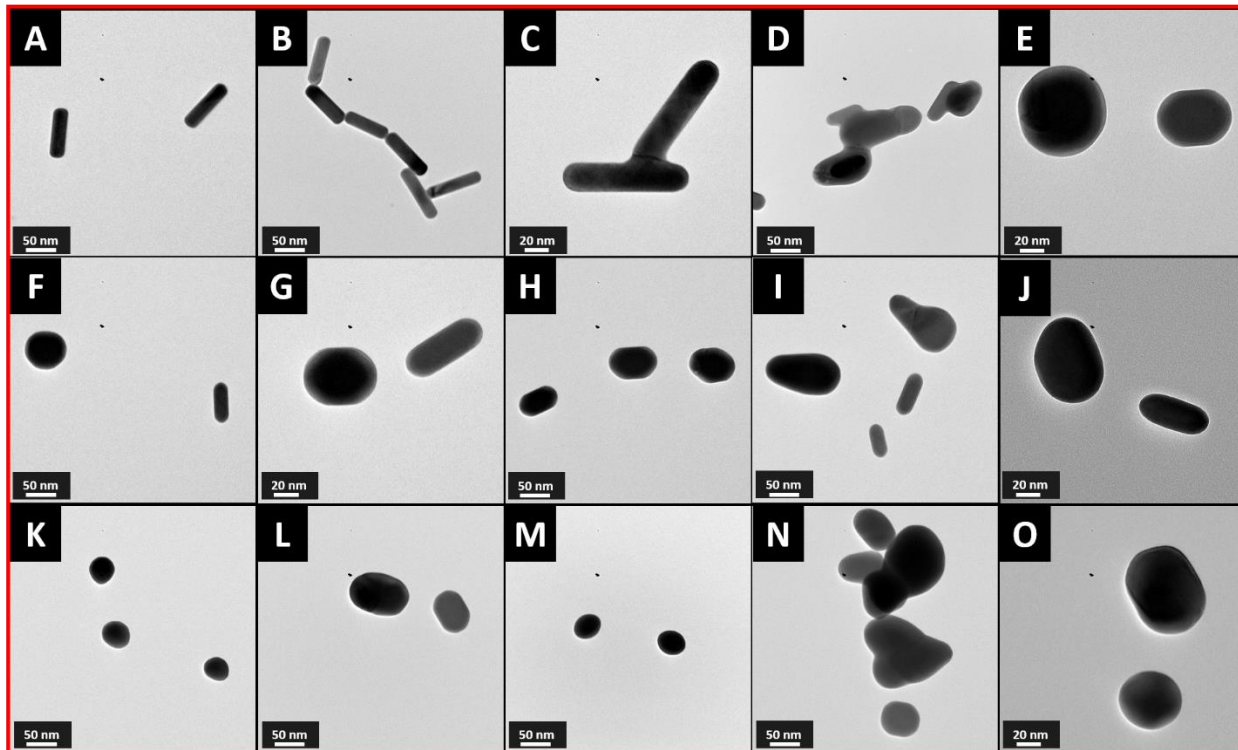


Figure 12. Thermal stability of GNRs@CTAB. (A-O) TEM images of GNRs@CTAB during in situ TEM heating upon annealing at 25, 100, 150, 200, 250, 300, 350, 400, 450, 505, 550, 600, 650, 700 and 750° C, respectively.

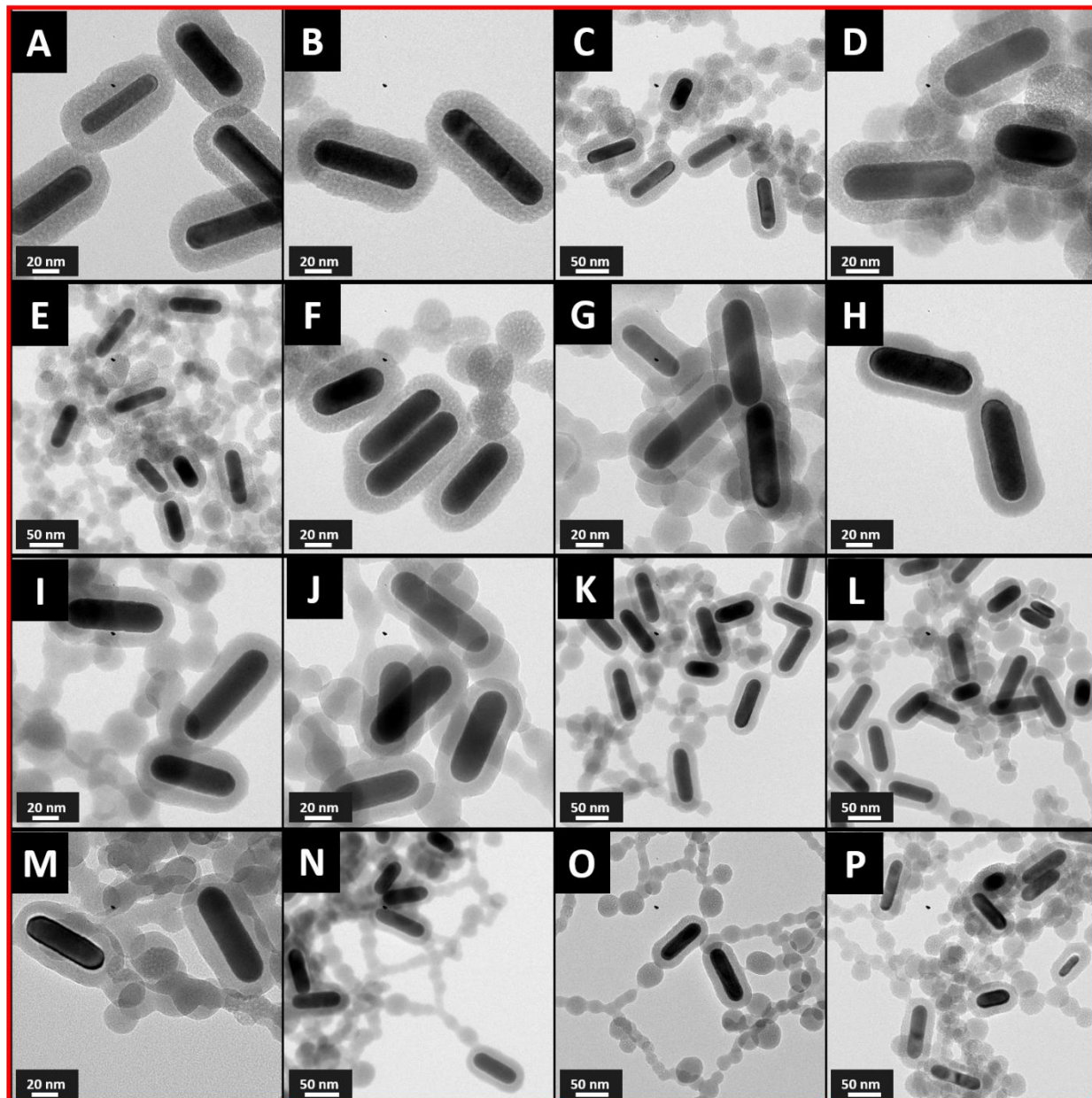


Figure 13. Thermal stability of GNRs@SiO₂. (A-P) TEM images of GNRs@SiO₂ during in situ TEM heating upon annealing at 25, 100, 150, 200, 250, 300, 350, 400, 450, 505, 550, 600, 650, 700, 750 and 850° C, respectively.

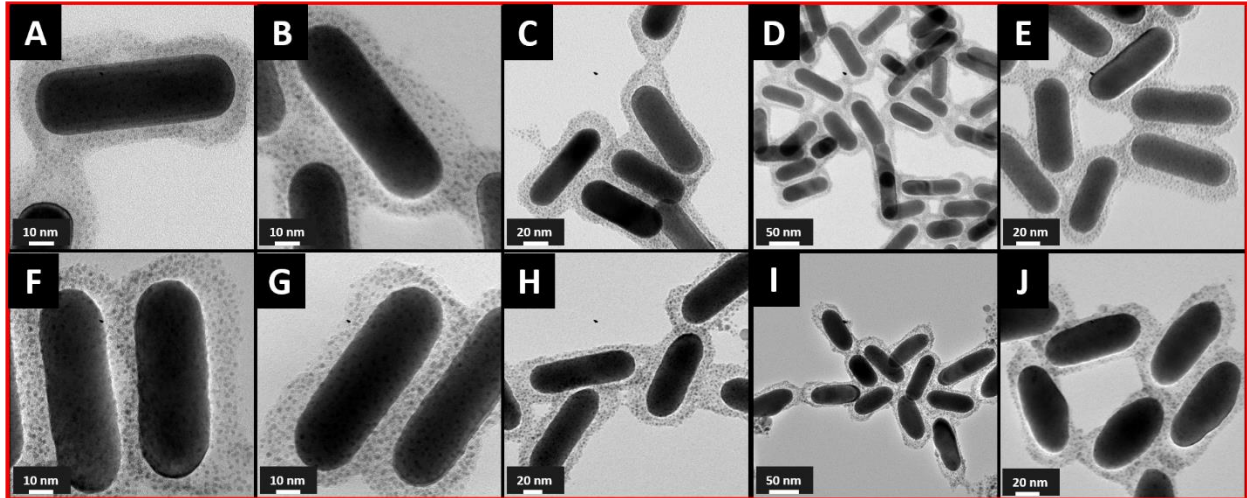


Figure 14. Thermal stability of GNRs@SiO₂@GNCs. (A-J) TEM images of GNRs@SiO₂@GNCs during in situ TEM heating upon annealing at 25, 200, 300, 400, 505, 600, 700, 800, 900, and 1000° C, respectively.

1.2.8 Photothermal behavior of GNRs upon silanization and coating with GNCs

Apart from the in situ and ex situ thermal heating-induced structural and morphological changes of GNRs, photothermal heating-induced fragmentation and melting of GNRs as a result of the interaction of the plasmonic GNRs with laser light can also take place.[121, 129-131] Inspired by such a phenomenon, various work have been done to control the shape and size of already synthesized NPs of wide size and shape distribution using laser pulses-induced shape transformation.[129, 132-135] On the other hand, intensive research have been also carried out to prevent the photothermal heating-induced morphological changes of GNRs in order to preserve their unique optical properties. In order to find out whether functionalizaion of silica-coated GNRs with GNCs could affect the photothermal behavior of GNRs, the ns pulsed laser-induced structural changes of different aspect ratios of GNRs before and after functionalization with silica and GNCs were monitored using UV-vis spectroscopy and TEM. GNRs of AR~3.5 and 5 with LSPR centered at approx. 785 nm and 900 nm, respectively, were irradiated with different number of ns laser pulses (200-9000 pulses) of a 1064 nm laser with a typical fluence of approx. 320 mJ/cm². The UV-vis spectra of irradiated GNRs@CTAB (AR~3.5 and 5) revealed laser beam-induced spectral hole-burning as could be seen from decreased extinction values after ns laser irradiation at the LSPR wavelength while increasing the extinction values at the TSPR wavelength (Figures 16 and

18). It worth noting that the initial increase of the extinction spectra and exceptional reduction of the LSPR bandwidth observed in case of the larger GNRs with AR of 5 after irradiation with 500 and 1000 ns laser pulses could be explained by the ability of laser beams to reduce the polydispersity of the presynthesized GNRs which results in narrowing of the LSPR bandwidth and increased extinction value of the resultant homogeneous GNRs, these observations are in line with a previous work which reported the femtosecond laser reshaping-aided synthesis of GNRs with ultranarrow LSPR bandwidth.[136] The TEM images of irradiated GNRs@CTAB confirmed the spectroscopic results. Irradiation of GNRs@CTAB (AR~3.5 and 5) with 9000 pulses of ns laser results in dramatic morphological changes into the more thermodynamically-stable spherical NPs (Figures 15 A and F & 17 A, F and K). The effect of irradiating the larger GNRs (AR~ 5) with 1000 pulses was also investigated to figure out the intermediate shapes formed during the laser ablation process. The TEM results obtained after irradiating larger GNRs@CTAB with 1000 ns laser pulses of approx. 320 mJ/cm^2 fluence revealed the formation of different shaped NPs (Figure 17F) such as; Φ -shaped NPs, where the GNRs become shorter and thicker from the middle region of the GNR shaft, and other bent or twisted structures such as sickle-shaped nanostructures spanned by a boundary at middle of the NPs, such structures have been reported to be formed after pulsed laser irradiation as a result of planar defect and twins formation in the body of irradiated NPs and had shown to dominates at early stage during melting process and at laser energy below the melting threshold of the GNRs.[121, 137] The TEM images from both smaller and larger GNRs@CTAB revealed that the photothermal reshaping of GNRs with ns laser pulses proceeds with a melting-mediated mechanism and is not fragmentation-based mechanism as could be revealed from the transformation of the majority of GNRs into prolate spheroid, Φ -shaped NPs and finally to spherical NPs of almost the same volume of the initial GNRs. Similar mode of action was reported previously where fragmentation of GNRs takes place upon irradiation with higher fluency of ns pulsed laser whereas melting takes place at low and intermediate laser fluences.[121]

On the other hand, our UV-vis spectroscopic and TEM results revealed the enhanced photothermal stability of GNRs upon coating with different thicknesses of silica shells (15 and 22 nm, hereinafter, referred to as “Si2” and “Si1”, respectively). In case of shorter GNRs, coating the GNRs with either thinner and thicker silica shells make the GNRs more robust during the ns laser irradiation, this could be clearly seen from their nearly unchanged UV-vis spectra which do not exhibit any spectral hole-burning (Figures 16 B and C). It should be pointed out that thicker silica

shells is much effective than thinner shells in enhancing the photothermal stability of GNRs. The UV-vis spectra of GNRs coated with the thinner silica shells (15 nm) started to exhibit a blue-shift of the LSPR position accompanied by a decrease in the extinction value when the GNRs irradiated with 9000 ns laser pulses (Figure 16C). The TEM images of silica-coated GNRs further confirm the data obtained from the spectroscopic studies. Coating GNRs with thicker silica shells (22 nm) prohibits the photothermal reshaping of GNRs even after irradiation with 9000 ns laser pulses of approx. 320 mJ/cm² fluence (Figure 15G). Whereas, coating GNRs with thinner silica shells (15 nm), although appear robust up to 3000 ns laser pulses of approx. 320 mJ/cm² fluence, they could not resist the generated photothermal effect and start to reshape after irradiation with 9000 pulses of the same laser fluence (Figure H). By taking a close look at the TEM of the GNRs coated with thinner silica shell after pulsed laser irradiation, one could realize that the mechanism of photothermal reshaping is different than the mechanism showed for CTAB-coated GNRs. We have shown that the reshaping of GNRs@CTAB at our experimental conditions proceeds via a melting-mediated pathway, whereas, photothermal reshaping of GNRs@SiO₂ most probably follows a fragmentation-based mechanism. This could be seen by two evidences from spectroscopic and TEM studies; 1) the blue-shifting of the LSPR and 2) the shortening of the GNRs and decreased of the AR without significant alteration of the GNRs diameter. Similar results have been previously reported.[77]

The photothermal stability shown by coating GNRs core with different silica thickness could be explained by the significant heat diffusivity of silica shells which competes with photothermal-induced reshaping of GNRs. It has been shown that the accelerated photothermal reshaping of CTAB-coated GNRs results from the densely packed CTAB layers which has a much lower thermal conductivity (K) than water ($K_{\text{Water}} = 0.598 \text{ W/mK}$ and $K_{\text{CTAB}} = 0.140 \text{ W/mK}$)[138] and hence act as heat barrier against heat diffusion which leads to heat accumulation and hence expansion and melting of the GNRs. Whereas, the thermal conductivity of silica was estimated to be approx. twice the that of water ($K_{\text{Silica}} = 1.4 \text{ W/mK}$) which enhances the heat diffusivity to the surroundings and prevents heat build-up by GNRs. This could also explain the better photothermal stability of thicker silica shells which implies better heat distribution over larger surface area and enhanced heat diffusion to the surroundings. Moreover, the rigidity of silica shells hinders the diffusion of surface atoms and hence the GNRs reshaping.

In case of larger GNRs, UV-vis spectra of silica-coated GNR after ns laser irradiation of showed gradual blue-shift of the LSPR as a function of deposited laser pulses (Figure 18 B and C). The different behavior seen at such case than the one showed for shorter GNRs may be due to 1) the higher absorption cross-section and hence more deposited energy of the larger GNRs at the laser wavelength (1064 nm) compared to that of shorter GNRs[76] and 2) the GNRs with shorter AR have been shown to be thermodynamically stable than GNRs with larger AR[76] which in turn means the same number of laser pulses of the same fluence significantly affects larger GNRs than shorter GNRs.

Conjugating silica-coated GNRs with GNCs seemed to alter the mechanism by which GNRs@SiO₂ are deformed upon ns laser irradiation. Irradiating GNRs@SiO₂@GNCs with ns laser pulses (9000 ns laser pulses, 320 mJ/Cm²) results in GNRs reshaping into prolate spheroid and Φ -shaped NPs (Figures 15J & 17 I, N, J and O), whereas, irradiation of GNR@SiO₂ with the same laser pulses did not show such intermediate shapes which are characteristic for the photothermal-induced melting process. It seems that the mechanism of GNRs reshaping in case of GNRs@SiO₂ proceeds mainly through a fragmentation mechanism, this can also be confirmed by the formation of the bullet-shaped nanostructures where the GNRs start to fragment and release the gold through their mesoporous silica (Figures 15H & 17 G, L, H and M). Similar results have been for fs laser ablation of gold NPs below their melting point.[139, 140]

The photothermal-induced reshaping of GNRs upon irradiation with ns laser pulses takes place after the photons get absorbed by GNRs which lead afterwards to the heating of the electrons (electron-electron coupling) that occurs within the femtosecond time domain (500 fs),[137] the energy is then transferred to the lattice (electron-phonon coupling, 1-3 ps),[130] the latter process results in increased kinetic energy of the gold atoms and their surface diffusion to start the reshaping of GNRs. The GNRs continue to absorb more photons during the ns laser irradiation while the lattice is still hot which results in increased lattice energy. On the other hand, the hot lattice dissipates some heat to the surroundings in the phonon-phonon relaxation process (100 ps).[130] The phonon-phonon coupling process is heat loss mechanism and the rate of heat generation in the lattice to the rate of heat loss will determine the shape of irradiation product of GNRs. For instance, higher irradiation time with high energy ns laser pulses will overcompensate the energy loss during phonon-phonon coupling process resulting in fragmentation of the GNRs,

whereas, using higher irradiation time with low energy ns laser pulses in a way that not completely overcompensate the energy loss to the surroundings results in shortening of the GNRs.[130]

As could be seen from the UV-vis spectra, functionalization of GNRs@SiO₂ with GNCs reduces the fragmentation and shortening of GNRs upon laser irradiation (Figures 16E & 18 D and E). To our surprise, functionalization with GNCs switches the photothermal reshaping mechanism of GNRs@SiO₂ back from a fragmentation-based reshaping into melting-based reshaping. Firstly, the TEM images and UV-vis spectra of laser irradiated GNRs@CTAB revealed the gradual melting of GNRs as could be seen from initial formation of Φ -shaped NPs, V-shaped and twisted NPs which finally transformed into spherical NPs of almost the same volume of starting GNRs with UV-vis spectral hole burning characterized by decreased extinction value at LSPR wavelength (Figures 15F and 16A). Whereas, the TEM images and UV-vis spectra of silica-coated GNRs revealed gradual shortening of the GNRs and formation of bullet-shaped NPs with gradual blue-shifting of LSPR band upon increasing number of laser pulses (Figures 15H & 17 G, L, H and M). Such morphological and spectral changes of silica-coated GNRs suggest a switching mechanism of reshaping upon silica coating. On the other hand, conjugating the GNRs@SiO₂ with GNCs switched the reshaping mechanism from fragmentation-based into melting-based, though rates of shape transformation and spectral changes much lower than that observed for GNRs@CTAB (Figures 15J & 17 I, N, J and O).

It worth noting here that the frequent laser irradiation and extended irradiation time did not affect the fluorescence behavior of the GNCs (Figure 19). It seems like the photophysical properties of the GNCs are not affected by the spatial heating generated upon irradiating GNRs with ns laser pulses. These results are consistent with the almost intact structures of GNCs observed during the in situ TEM heating results of GNRs@SiO₂@GNCs. As such, our nanohybrid composite material showed robustness during thermal and photothermal heating.

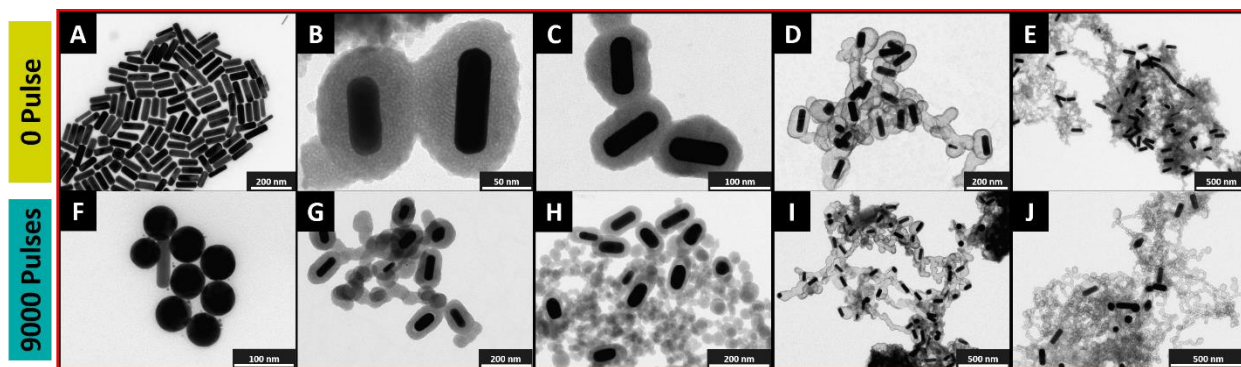


Figure 15. TEM results of the photothermal shape transformation of low AR GNRs and GNRs nanocomposites upon ns laser irradiation. TEM images of GNRs@CTAB (A and F), GNRs@Si1 (B and G), GNRs@Si2 (C and H), GNRs@Si1@GNCs (D and I), and GNRs@Si2@GNCs (E and J), before and after irradiation with 9000 ns laser pulses, respectively.

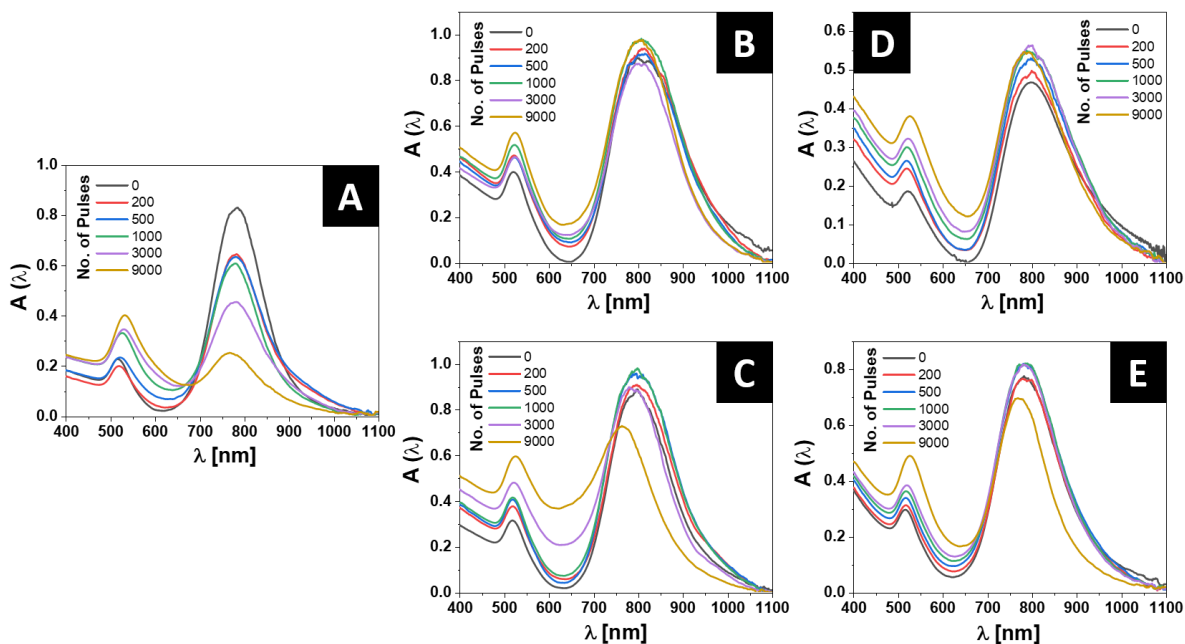


Figure 16. UV-vis spectra of the photothermal shape transformation of low AR GNRs and GNRs nanocomposites upon ns laser irradiation. UV-vis spectra of GNRs (A), GNRs@Si1 (B), GNRs@Si2 (C), GNRs@Si1@GNCs (D), and GNRs@Si2@GNCs (E), before and after irradiation with different number of ns laser pulses.

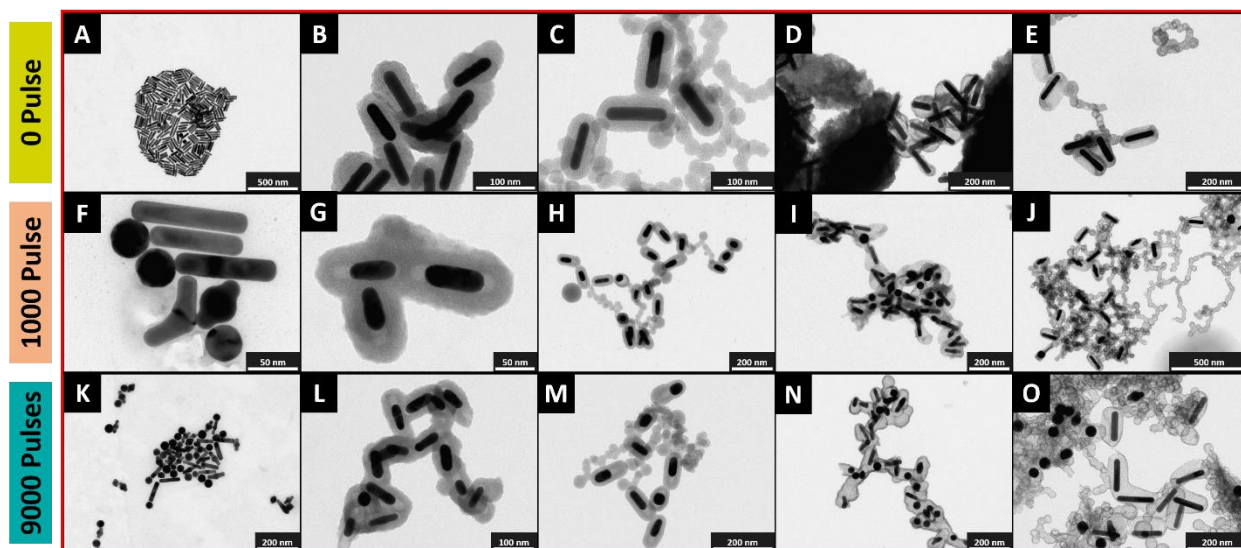


Figure 17. TEM results of the photothermal shape transformation of high AR GNRs and GNRs nanocomposites upon ns laser irradiation. TEM images of GNRs@CTAB (A, F and K), GNRs@Si1 (B, G and L), GNRs@Si2 (C, H and M), GNRs@Si1@GNCs (D, I and N), and GNRs@Si2@GNCs (E, J and O), before and after irradiation with 1000 and 9000 ns laser pulses, respectively.

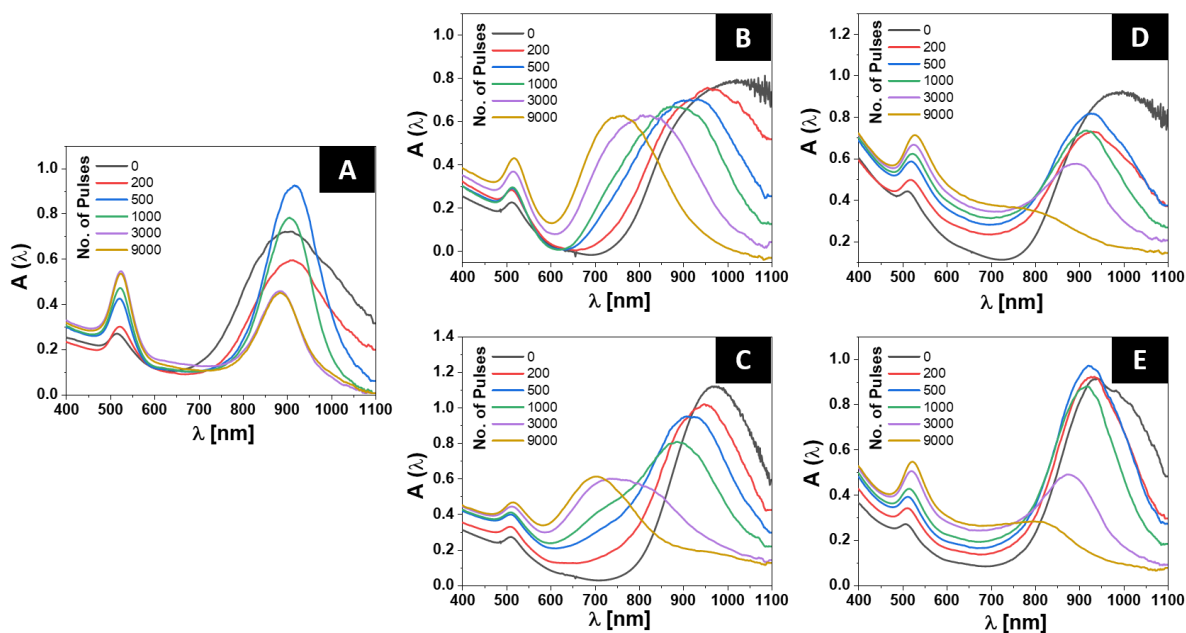


Figure 18. UV-vis spectra of the photothermal shape transformation of high AR GNRs and GNRs nanocomposites upon ns laser irradiation. UV-vis spectra of GNRs (A), GNRs@Si1 (B), GNRs@Si2 (C), GNRs@Si1@GNCs (D), and GNRs@Si2@GNCs (E), before and after irradiation with different number of ns laser pulses.

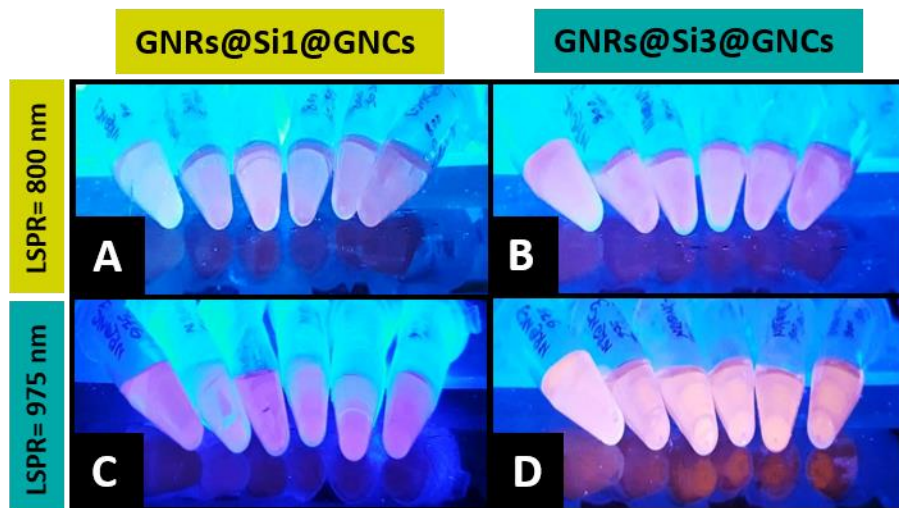


Figure 19. Retained Fluorescence properties of GNCs after irradiation of $\text{GNRs@SiO}_2\text{@GNCs}$ with 9000 ns laser pulses.

Chapter 2: BSA-directed synthesis of colloiddally stable and biocompatible Au nanopopcorn¹

2.1 Introduction and aim of the work

Gold-based nanostructures have drawn great attention due to their unique properties and their potential uses in different fields of nanoscience-based applications.[141-143] Their physicochemical properties could easily be adjusted by tuning their size, morphology, and surface chemistry.[142, 144]

In the last few decades, different isotropic and anisotropic shapes of GNPs have been developed.[144] In particular, anisotropic GNPs have drawn much attention as they have more interesting physicochemical properties that are most often surpassing those of their isotropic counterparts, i.e., the 0D spherical GNPs.[145] In contrast to spherical (nonhollow) Au NPs, most anisotropic and hollow Au NPs apparently exhibit a plasmon peak in the NIR region (therapeutic window), where the attenuation by biological tissues is very minimal.[145] Therefore, such anisotropic NPs can be utilized in various biomedical applications including diagnosis as well as therapy (i.e., “theranostics”).[146] Anisotropic NPs with their sharp edges and tips could also offer a great platform for the enhancement of the SERS activity.[147] Nevertheless, cytotoxicity of the anisotropic GNPs is a major issue when it comes to biomedical applications.[148, 149] The toxicity exhibited by most anisotropic GNPs is mainly arising from their capping agents or surface ligands. For instance, it has been shown that CTAB, which is a cationic surfactant frequently used for the synthesis of different anisotropic GNPs such as GNRs, GNPCs, gold nanoprisms (GNPRs), is cytotoxic to many cell lines.[149] There have been different routes to passivate the CTAB effect either by surface overcoating or ligand exchange of CTAB in postsynthesis procedures.[150] for instance, polymer coating is commonly used to modify the surface chemistry by wrapping the undesired capping agents such as CTAB, making them more biocompatible by reducing the exposure of biological compartments to the cytotoxic capping agents.[149, 151] Ligand exchange is another alternative way to exchange the bound capping agents with more benign ligands.[152-155] However, 100% wrapping or removal of surface ligands by overcoating or ligand exchange, respectively, is not possible and the leftover ligands can yet exhibit some sort of toxicity.[149, 154] In order to overcome the drawbacks usually associated with those classical approaches, a sustainable route for the synthesis of biocompatible anisotropic GNPs would be ideal. There have

¹ The data of this work has been published in [166].

been various green routes for the synthesis of anisotropic GNPs using a number of biomolecules, however, not only the precise control over the nanoparticle size but also their colloidal stability and large-scale preparation are still major challenges.[67, 156-158]

It has been shown that the surface chemistry of NPs is influenced to a great extent by the protein corona formation in different biological media.[159] Moreover, the protein corona can lead to various alterations in the physicochemical properties of NPs, for instance formation of protein corona increases their hydrodynamic diameters and could result in aggregation of NPs with compromised colloidal stability.[160, 161] On the other hand, protein corona has been shown to reduce toxicity of nanoparticles.[162] Nevertheless, there have been a debate regarding the effect of protein corona on NPs in various drug delivery-based applications.[163]

Given the fact that they can be used as reducing, shape-directing agents and are considered as naturally preformed protein corona, proteins could offer a powerful alternative to the classical toxic ligands for the synthesis of biocompatible and colloidally stable anisotropic NPs.[65, 66]

In this work we report an efficient and sustainable synthesis method of anisotropic gold nanopopcorn (GNPCs). In this work, the effect of using different proteins on dictating the shape of NPs was evaluated. Among different proteins, BSA has shown superiority over other protein in synthesizing monodisperse GNPCs of narrow size distribution. The synthetic route is scalable and liters of GNPCs ($C_{Au} = 5.6 \times 10^{-4}$ M) could be synthesized in one single batch. The tunability, colloidal stability, as well as the cytotoxicity of BSA-capped GNPCs have been also evaluated.

2.2 Results and discussion

2.2.1 Characterization of NPs

In this study, BSA was selected as a shape-directing agent because of its biocompatible nature as well as its potential shape-dictating capability. [65, 66] This sustainable synthetic route is straightforward and could be used for the large-scale preparation of high quality GNPCs (scheme of the synthesis is shown in Figure 20A). The UV–vis absorption spectra of GNPCs exhibit an absorption peak centered at 588 nm (Figure 20B), which matches well with the reported branched GNPs.[164] The broadening in the absorption peak (fwhm= 100 ± 10 nm) results from different arm length of individual GNPCs. The TEM images show uniform and branched popcorn-shaped GNPs, similar to the NPs previously reported by Lu et al.[36] where the CTAB was used as a

surface capping agent. The GNPCs@BSA have an average core diameter (d_c) and arm's length of 70 ± 5 nm and 12 ± 5 nm, respectively, and is in a good agreement with the results from dynamic light scattering (DLS) measurements which revealed a hydrodynamic diameter (d_h) of ca. 80 ± 8 nm (Figure 20C). High-resolution transmission electron microscopy (HRTEM) images and Fourier transformation (FFT) pattern indicate the crystalline nature of GNPCs (Figure 20 D–I). FFT patterns of GNPCs exhibited the characteristic (111) and (200) planes of the face-centered cubic (fcc) structure of gold, similar to those showed by previously reported branched GNPs (Figure 20 G and I).[157, 165]

It should also be noted that using the same synthesis route, other proteins can successfully produce GNPCs (Figure 21), however, the obtained NPs exhibited significant polydispersity than that showed by the GNPCs@BSA. To further confirm the substantial role of BSA in dictating the shape of GNPCs, a control experiment was done during which no BSA was added. The purple-colored NPs formed during the control experiment exhibited a narrow absorption peak centered at 535 nm, suggesting the formation of spherical NPs with a shoulder at 750 nm, suggesting an aggregation of the NPs (Figure 22). In another control experiments, different capping agents instead of BSA were used such as citrate, polyvinylpyrrolidone (PVP) and CTAB. The NPs formed using citrate and PVP exhibited a plasmonic peak centered at ~ 530 nm (Figure 23), again suggesting the formation of isotropic spherical NPs.[150] Whereas, CTAB produced sponge-like nanostructures (Figure 24) with a plasmonic peak at ~ 590 nm.

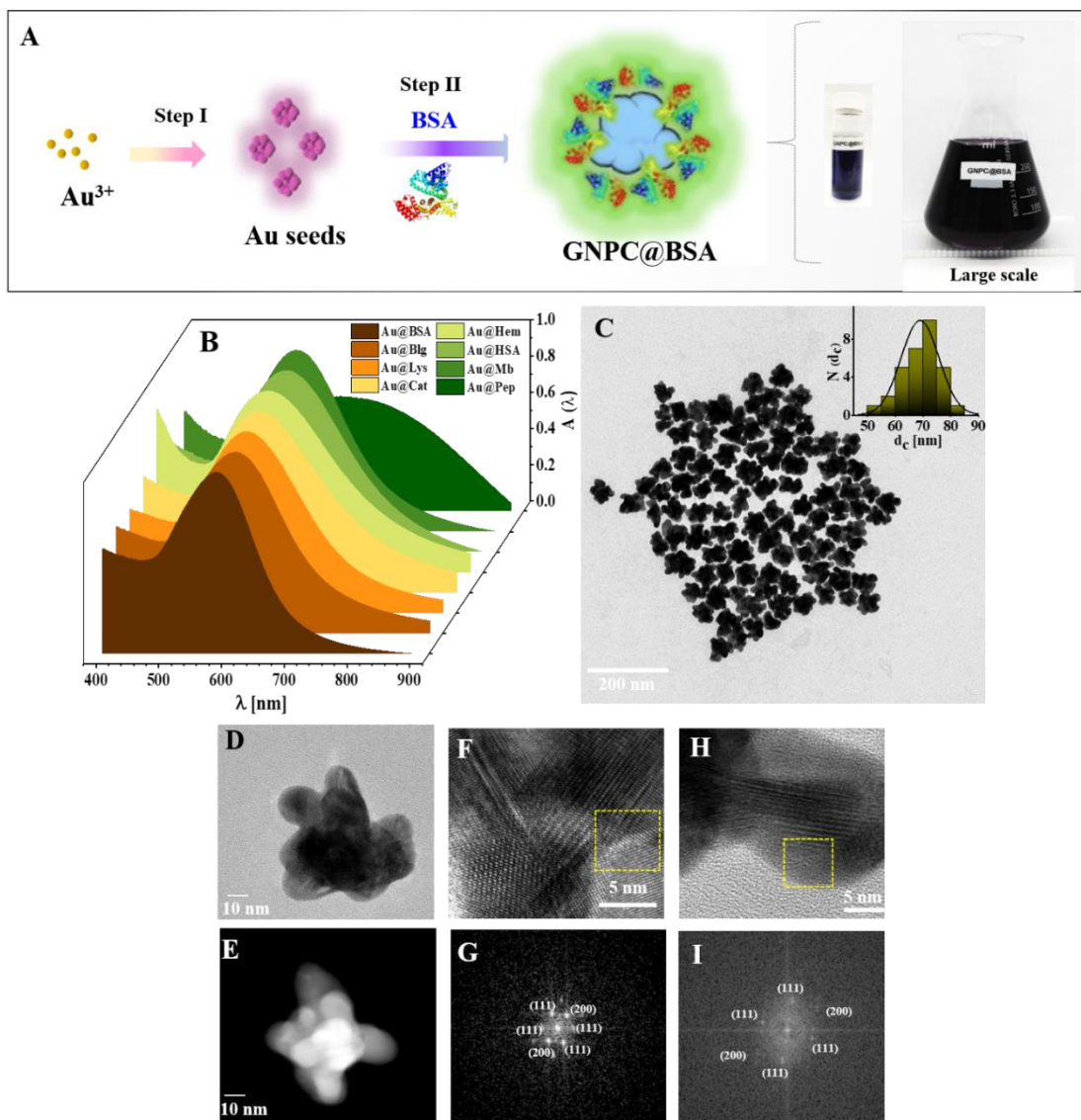


Figure 20. Synthesis and characterization of GNPC@BSA. (A) Scheme of GNPCs@BSA synthesis with photographs of the corresponding GNPC@BSA in small scale (left) and large scale (right). (B) UV-vis absorption spectra of GNPC@BSA and other GNPs synthesized using different ligands other than BSA. (C) TEM images of GNPC@BSA. The inset shows the d_c values (length from tip to tip) distribution histogram of GNPC@BSA. (D and E) TEM and STEM images of a single GNPC@BSA, respectively. (F, H and G, I) HRTEM and corresponding FFT pattern of selected regions, respectively. Prepublished in [166].

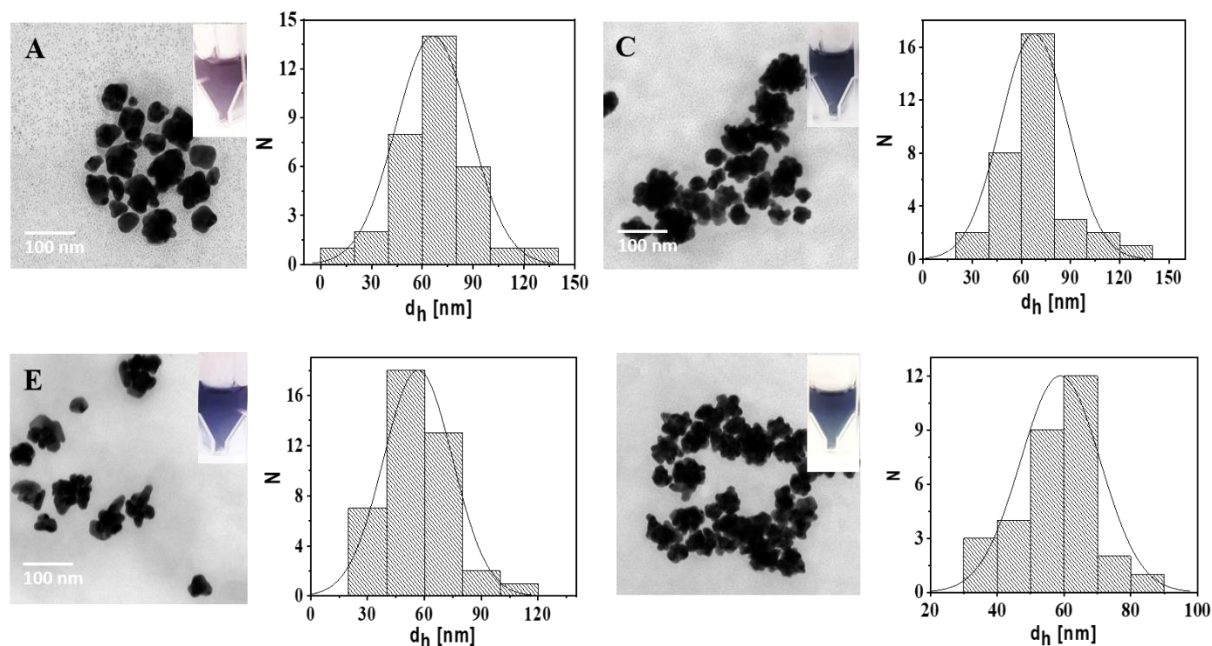


Figure 21. Characterization of GNPs synthesized by different proteins other than BSA. TEM images and corresponding size distribution of the dc values of (A-B) Au@Blg NPs, (C-D) Au@Cat NPs, (E-F) Au@Lyz NPs, and (G-H) Au@Hem NPs. Insets are photographs of the corresponding GNPs, Prepublished in [166].

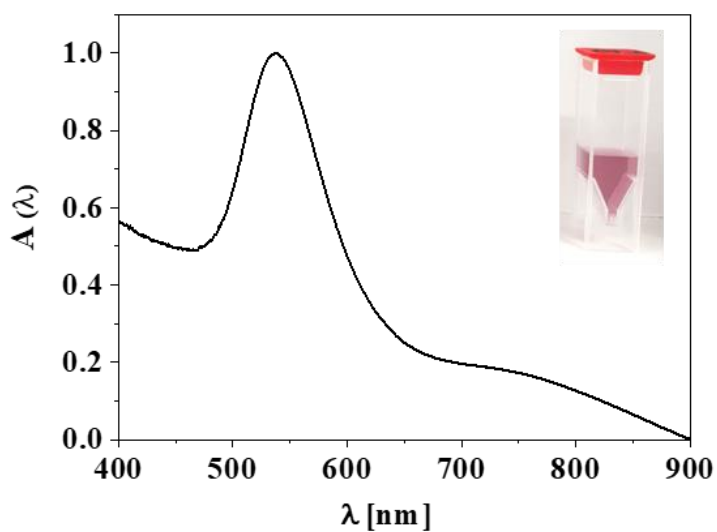


Figure 22. Absorption spectrum of spherical GNPs synthesized without the use of BSA. Prepublished in [166].

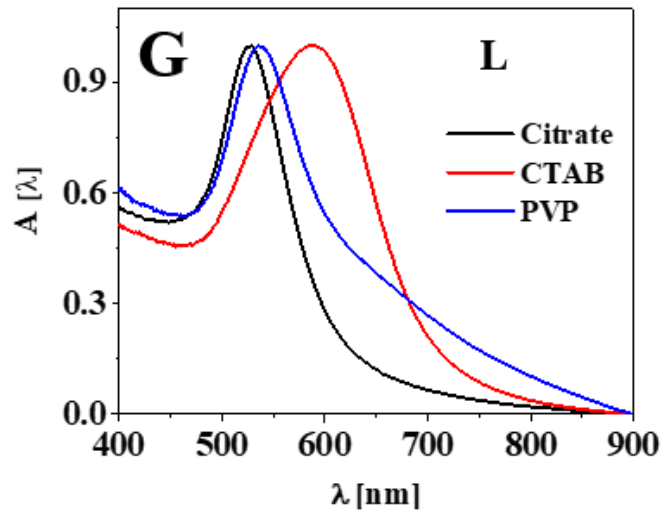


Figure 23. UV-vis absorption spectra of GNPs formed by using different ligands other than BSA. Prepublished in [166].

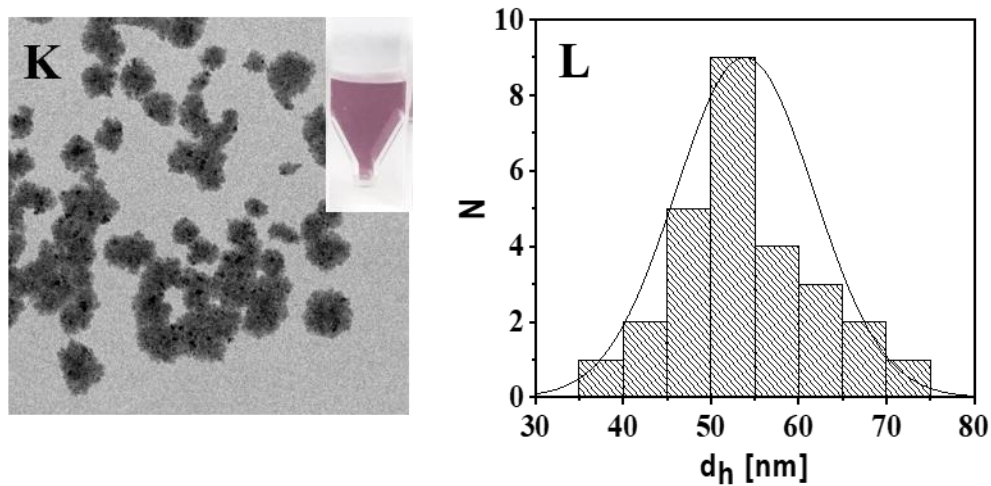


Figure 24. TEM and size distribution of sponge-like NPs formed using CTAB instead of BSA. Prepublished in [166].

The plasmonic peak of GNPs could be tuned by adjusting the reaction parameter such as volume of seed solution (V_s), concentration of Au precursor in seed solution ($C_{Au(s)}$), volume of Au precursor added in the growth step ($V_{Au(g)}$), concentration of Ag precursor (C_{Ag}), reaction pH and

temperature (Figure 25). The results showed that a tuning of the absorption peak of GNPCs@BSA to the NIR region is possible.

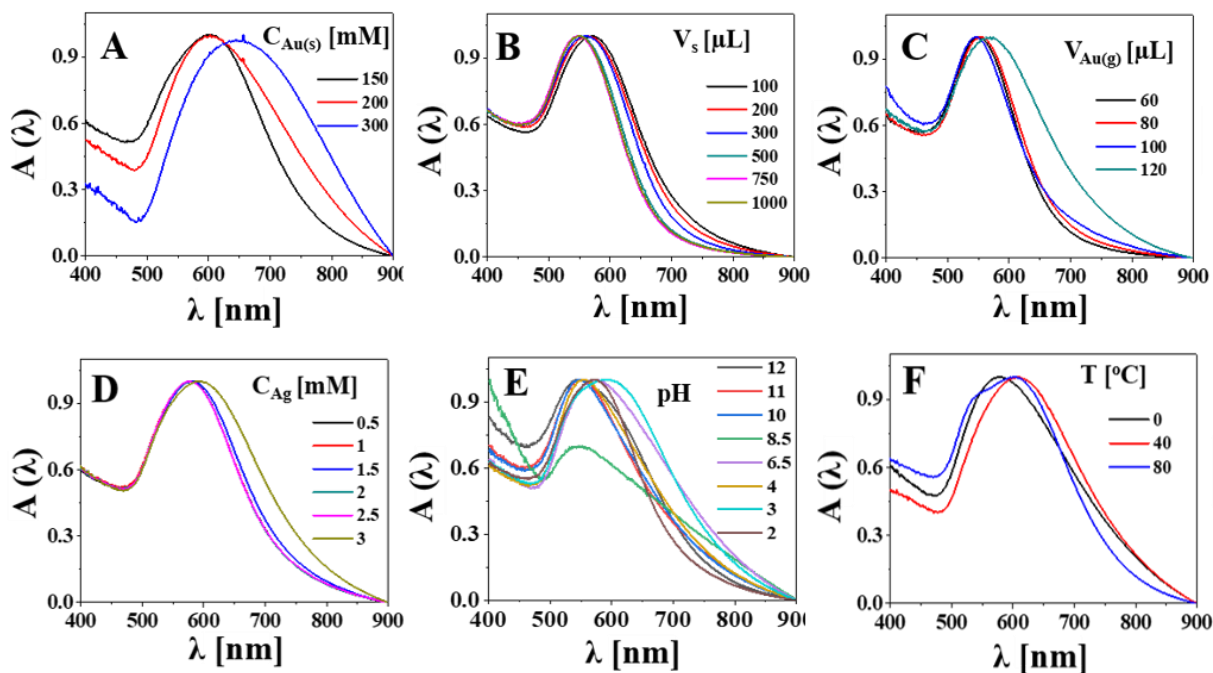


Figure 25. UV-vis absorption spectra of GNPs formed by tuning different synthetic parameters; A) $C_{Au(s)}$, B) V_s , C) $V_{Au(g)}$, D) C_{Ag} , E) pH of the reaction, and F) reaction temperature (T). *Prepublished in [166].*

As an essential step to understand the role of protein structure in dictating the anisotropic shape of GNPCs, structural changes of BSA during the course of GNPCs formation were investigated using circular dichroism (CD) spectroscopy (Figure 26A).[167] The CD spectra of GNPCs@BSA were compared with those of native BSA solution (pH 6.5) and acidified BSA solution (pH 3.1, corresponding to the pH value during the course of GNPCs@BSA formation).

BSA at almost neutral pH shows one spectroscopic band at 190 nm in the positive absorption side and two other bands at ca. 209 and 222 nm in the negative absorption side. The later peaks are characteristic for the α -helix structure of BSA (Figure 26A).[168]

Deconvolution of the CD spectra[169] suggests that the native BSA (pH 6.5) consists of about 51% α -helix, 3% strand, 14% turn, and 32% irregular structures (Figure 26A and Figure 27). Whereas, GNPCs@BSA consists of only 10% α -helix, 27% strand, 15 % turn, and 48% irregular structures (Figure 26A), suggesting a nearly complete loss of the proteins' secondary structure. To understand at which stage in the growth step are the structural changes of BSA initiated, a set of control experiments were carried out during which the CD spectra of BSA are recorded. The control experiments revealed that the CD spectral behavior of BSA did not significantly change until only the addition of Au precursor to the reaction medium, after which the CD bands of native BSA are almost disappeared, which suggests a unique and strong interaction between BSA and Au salt, resulting in the loss of the α -helix conformation of BSA, and the subsequent unfolding of BSA.[170]

To gain more insights on the structural transformation of BSA, fluorescence spectra were recorded. The intrinsic fluorescence of BSA arises mainly from two tryptophan (Trp) residues located in different domains of BSA, namely, (Trp-134) in domain I and (Trp-213) in domain II.[168] Structural transformations of BSA could be examined by measuring the emission intensity and emission maxima after selectively exciting the tryptophan at 280 nm, as any alteration in the local environment of tryptophan could affect the fluorescence behavior of BSA. A drastic drop in the fluorescence intensity as well as significant increase in the emission maxima of GNPCs compared to native BSA have been observed (Figure 26B and Figure 28). These results are consistent with the changes observed in the CD behavior and further confirm the BSA unfolding during the formation of GNPCs.

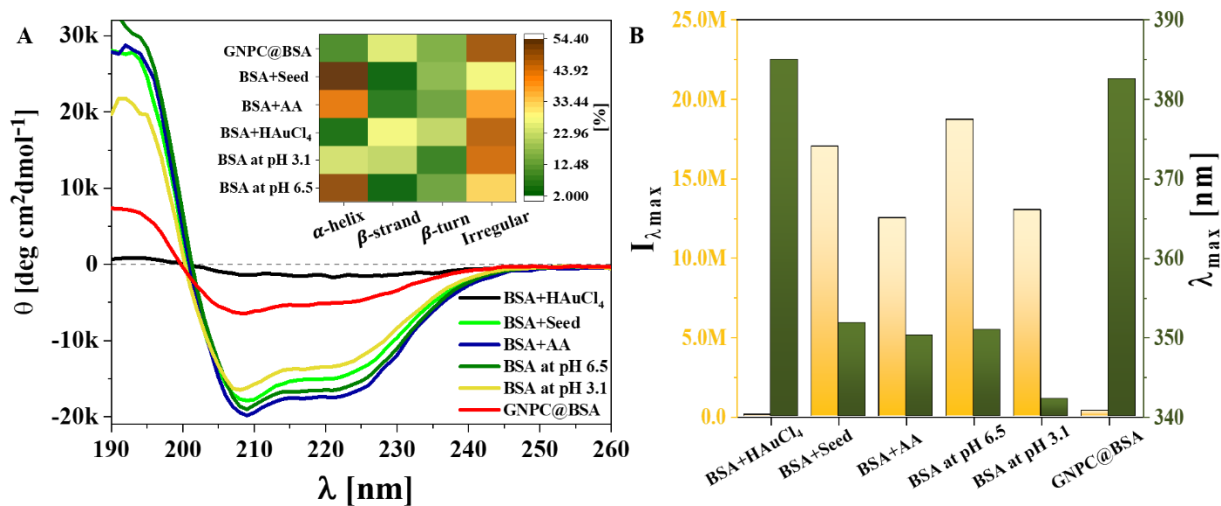


Figure 26. Understanding the structural changes of BSA during GNPCs synthesis. A) CD spectra of GNPCs@BSA and different control samples. To avoid the noise at lower wavelength (190–200 nm), all spectra were smoothed using OriginPro 2018 (5 points, Savitzky–Golay). The inset shows a heat map specifying the contents of different secondary structure elements of BSA. (B) Fluorescence intensity (yellow bars) and maximum emission wavelength (λ_{max}) (green bars) of different samples. Prepublished in [166].

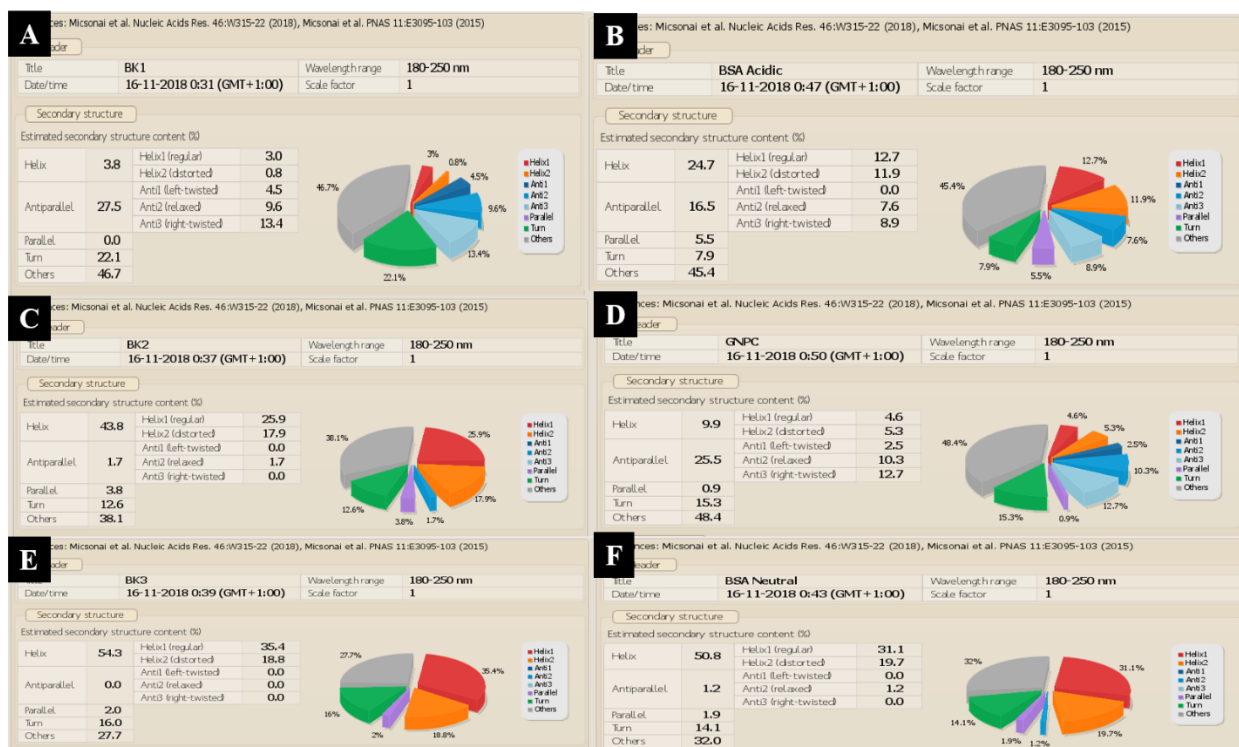


Figure 27. Table representing the deconvoluted protein structures from the corresponding CD spectra (presented in Figure 26). A) BSA+HAuCl₄, B) BSA at pH 3.1, C) BSA+ascorbic acid (AA), D) GNPC@BSA, E) BSA+seed GNPs, and F) BSA at pH 6.5. Prepublished in [166].

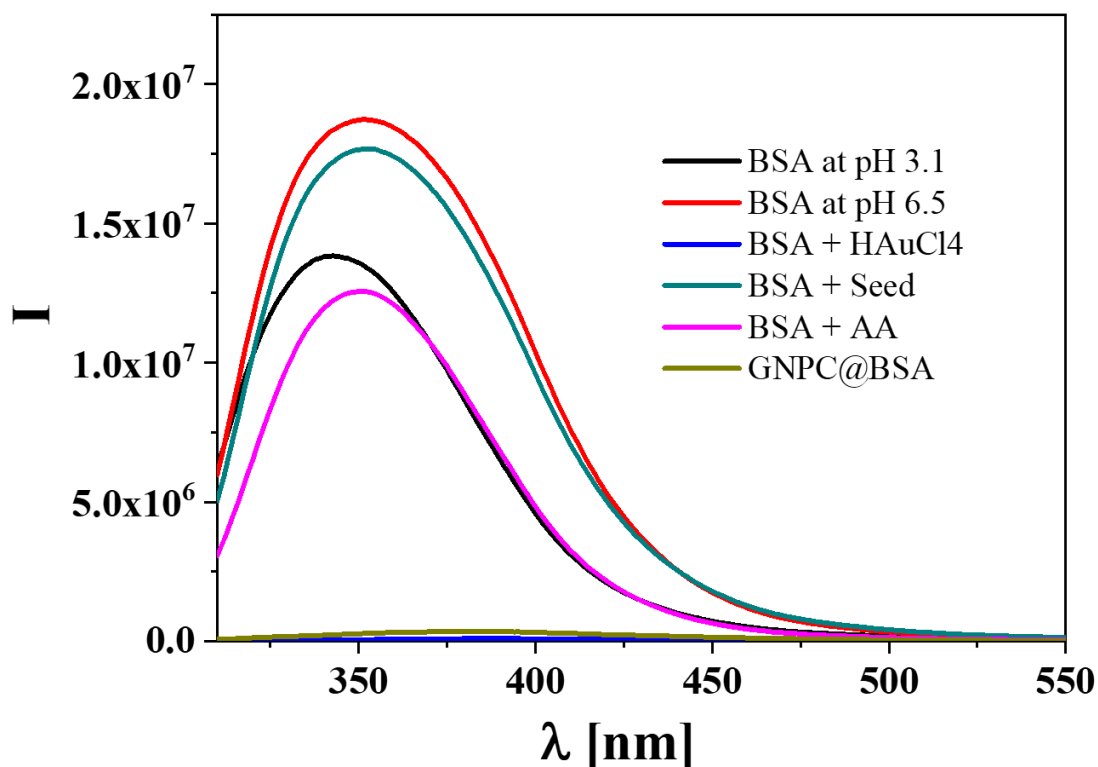


Figure 28. Fluorescence emission spectra of GNPCs@BSA and native BSA under different synthetic conditions. Prepublished in [166].

Summing up the previous results, one could conclude that the addition of Au precursor drops the pH of the reaction medium and induces the formation of Au^{3+} -protein complexes, both events facilitate protein unfolding and loss of protein's secondary structure. Unfolding of BSA as well as spatial nucleation of Au along the (111) and (200) facets may offer an appropriate biotemplate for the anisotropic growth of GNPCs.

2.2.2 Colloidal stability of NPs

It has been reported that colloiddally stable NPs in biological media is very crucial criterion in many biomedical applications and a compromised colloidal stability as well as protein corona formation affect the physicochemical properties of NPs.[150, 152] Since surface capping agents determine the major properties of NPs, such as their net charge, surface behavior, colloidal stability in different media, as well as their cytotoxicity,[171] studying how far could the surface chemistry affect the properties of GNPCs@BSA compared to almost similar sized NPs synthesized using

different surface ligands (citrate-capped Au NPs (GNP@Citrate), surfactant-free star-shaped AuNPs (GNS), and CTAB-capped popcorn-shape GNPs (GNPC@CTAB) (Figure 29A).

The colloidal stability of NPs in Milli-Q water, PBS and FBS-free/supplemented DMEM was investigated by monitoring their hydrodynamic diameters (d_h) for up to 36 h (Figure 29B, C and Figure 30). All NPs were stable in MQ water except for GNS, whereas, different trend of colloidal stability has been observed in FBS-supplemented DMEM as follows: GNPC@BSA > GNP@Citrate > GNS > GNPC@CTAB (ordered according to their colloidal stability as monitored by their d_h values at 36 h) (Figure 29B). The high colloidal stability of GNPC@BSA as well as the only slight increase in the hydrodynamic diameter of GNP@citrate is probably due to their net negative surface charge which means less adsorption of protein and slight increase in their d_h values.

On the other hand, the significant increase in the d_h values of GNPC@CTAB and GNS in FBS-supplemented DMEM suggests a strong protein corona formation and the subsequent aggregation of the GNPs (Figure 29 C and D). The high positive charge of CTAB-coated GNPCs as well as the easily accessible surfaces of GNS facilitates their interaction with proteins and in turn increases the protein adsorption and their aggregation which explains their increased d_h values while incubated in FBS-supplemented DMEM medium (Figure 31).

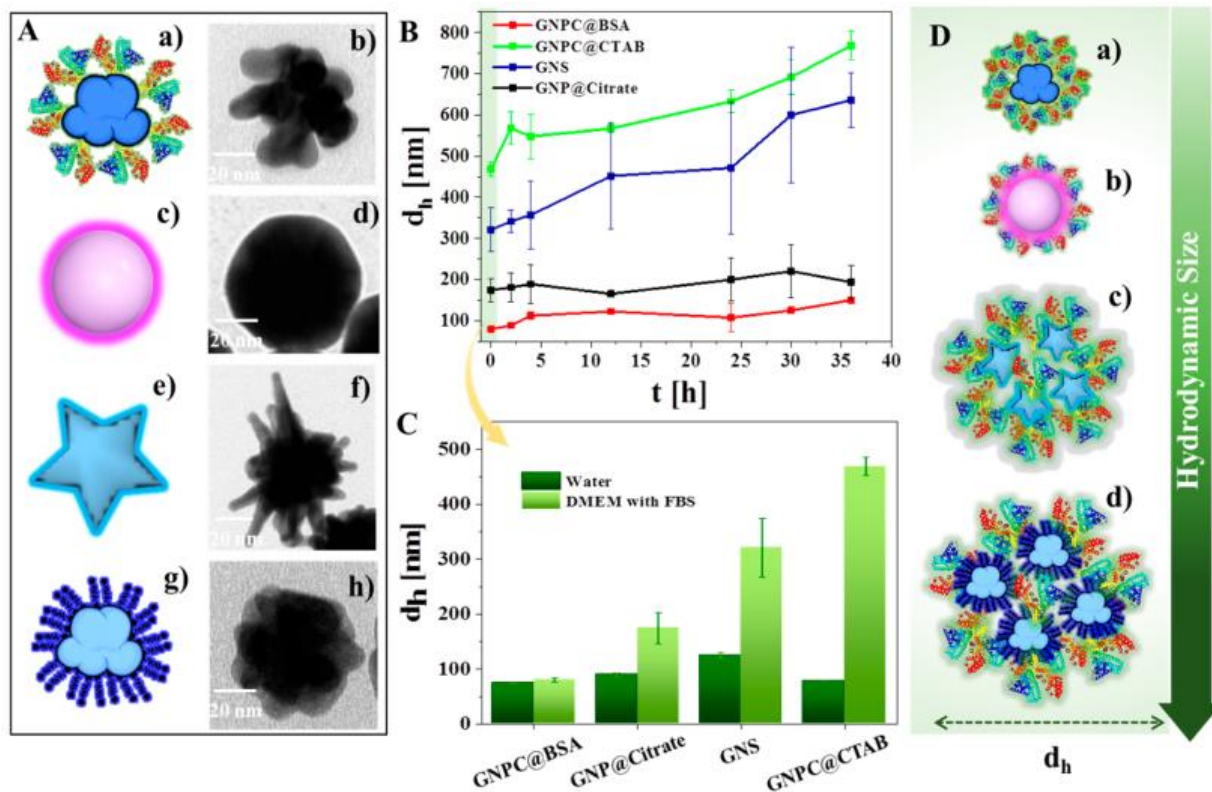


Figure 29. Effects of surface ligands on the colloidal stability of different GNPs in biological media. A) Comparative cartoon structures and TEM images of (a, b) GNP@BSA, (c, d) GNP@Citrate, (e, f) GNS, and (g, h) GNP@CTAB, respectively. B) Colloidal stability monitored as a change in d_h of GNPs over time in FBS-supplemented DMEM. C) d_h of different GNPs in water and FBS-supplemented DMEM (measured directly after addition, at $t = 0$ h, collected from the marked region of Figure 29B). D) Proposed schematics of the corona formation for the different GNPs. Prepublished in [166].

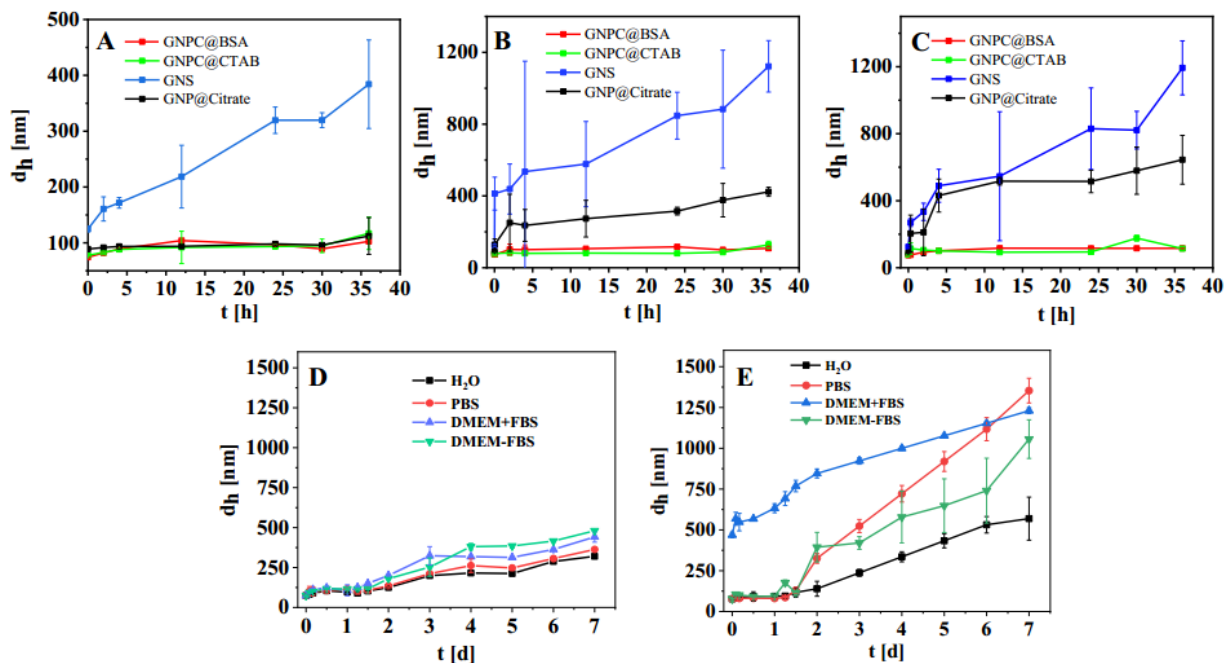


Figure 30. Hydrodynamic diameter (d_h) of GNPC@BSA, GNPC@CTAB, GNS, and GNP@citrate. d_h values of the different GNPs in A) water, B) PBS, and C) FBS-free DMEM. D) d_h of GNPC@BSA and E) GNPC@CTAB in different media over a period of 7 days. Prepublished in [166].

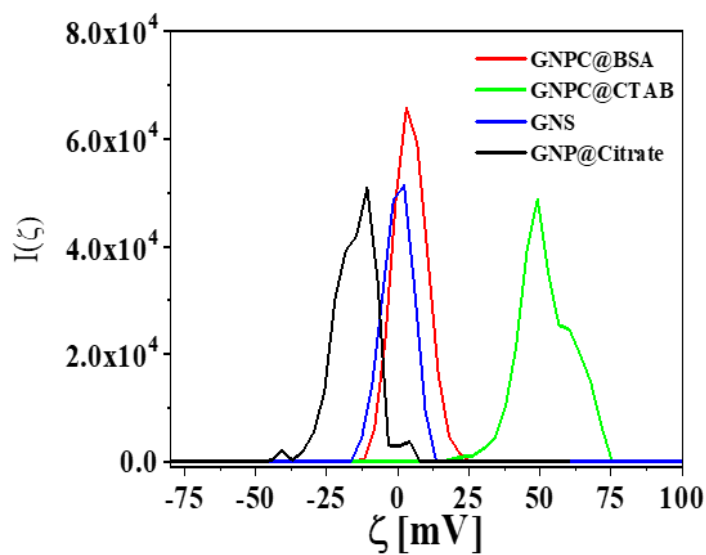


Figure 31. Zeta potential of GNPCs@BSA, GNPCs@CTAB, GNS, and GNP@citrate. Prepublished in [166].

2.2.3 Biocompatibility studies of NPs

The biocompatibility of GNPC@BSA has been evaluated by assessing their cytotoxicity on the cancerous Henrietta Lacks (HeLa) and the normal Medical Research Council cell strain 5 (MRC-5) cell lines using the resazurin assay and compared to that of the other GNPs prepared using different surface coating. The results revealed the higher cytotoxic effects of GNPC@CTAB (at concentrations $C_{Au} = 3.1\text{--}100 \mu\text{g/mL}$, as measured by inductively coupled plasma mass spectrometry (ICP-MS)) on both the cell lines. Our results are consistent with previous work reporting the toxic nature of CTAB for cellular applications.[65, 149] Whereas, GNPC@BSA as well as GNP@Citrate and GNS did not compromise the viability of HeLa as well as MRC-5 cells and exert no cytotoxic effect on both cell lines (up to the maximum C_{Au} employed in the study) (Figure 32 B and E). Further assessment of cytotoxicity was carried out using the lactate dehydrogenase (LDH) assay. The LDH assay evaluates the cell membrane integrity via measuring the amount of LDH, which normally located in the cytosolic compartment, released into the cell culture media when the cellular membranes got damaged and hence can be used to assess the cellular toxicity upon exposure to GNPs of different surface chemistry (Figure 32 C and F). Incubation of HeLa and MRC-5 cells with CTAB-capped GNPCs ($C_{Au} = 3.1\text{--}100 \mu\text{g/mL}$) up to 24 h resulted in a significant increase in %LDH release relative to the control cells compared to the %LDH released in the culture medium upon incubation with the same concentrations of BSA-coated GNPCs, citrate-capped GNPs, and GNS (Figure 32). These findings show that exposure to certain concentrations of CTAB-coated GNPCs damages the cell membranes of HeLa and MRC-5 cells with subsequent leakage of the intracellular LDH into the cell culture medium. The LDH assay results are consistent with the results of the resazurin assay and confirm the cytotoxic effects of GNPC@CTAB on both cell lines when used at concentrations above $C_{Au} = 3.1 \mu\text{g/mL}$. Despite the shown biocompatibility of both citrate-capped GNPs and GNS, their compromised and limited colloidal stability in PBS and DMEM media (cf. Figure 30) might make them less attractive for biomedical applications.

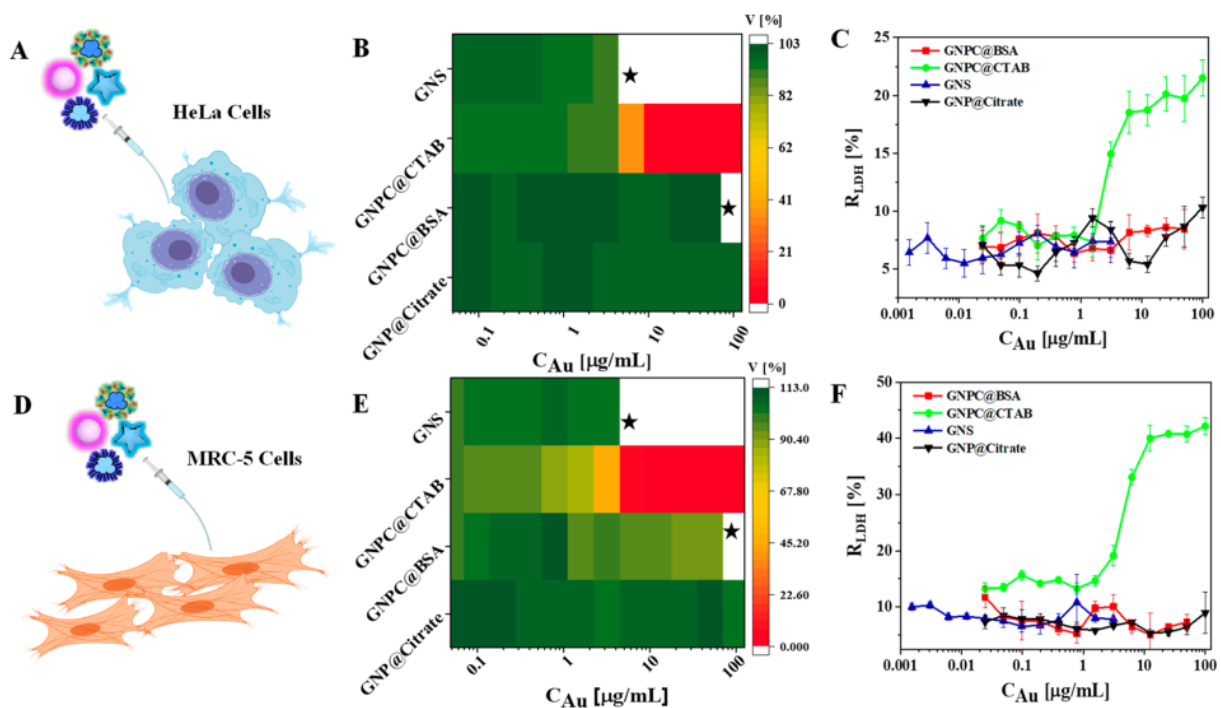


Figure 32. Effects of surface ligands on the biocompatibility of GNPs. (A, D) Cartoon illustration of HeLa cells and MRC-5 cells, respectively. (B, E) Heat maps representing the dose-dependent reduction in cell viability V after 24 h exposure of HeLa and MRC-5 cells, respectively, to different GNPs using the Resazurin assay from three independent experiments. Due to colloidal instability, GNS and GNPC@BSA cannot be concentrated more beyond the star marks labeled in the plot and their cytotoxicity beyond this concentration was not carried out. Effect of 24 h exposure of C) HeLa cells and F) MRC-5 cells to different GNPs on LDH release as depicted by the dose–response curves. Prepublished in [166].

Chapter 3: BSA-directed synthesis of porous bimetallic AgPt NPs with pH-switchable nanozyme activity and cargo loading capability¹

3.1 Introduction and aim of the work

Due to their distinct catalytic efficiency,[172, 173] electronic,[174] magnetic,[175] and optical[176] properties compared to their corresponding monometallic equivalents,[143] substantial attention has been devoted to bimetallic and multimetallic NPs over the past few decades. For example, previous studies have shown superior SERS and enhanced catalytic activity of the bimetallic AgAu, AgPd and AgPt NPs in comparison with the monometallic Ag NPs.[177-181] Bimetallic NPs are mostly synthesized through either of two pathways: 1) through the galvanic exchange (GE) between one metal of a desired sacrificial template morphology and another metal of relatively higher reduction potential, the difference in reduction potential will facilitate the other metal deposition on the sacrificial template,[182-184]or 2) through the co-reduction pathway, which simultaneously reduces the metal precursors using strong reducing agents.[185-187]Such strategies usually employ, however, the use of dangerous and noxious chemicals, such as surfactants. Non-biocompatible surfactants and hazardous chemicals must therefore be removed prior to the use of such NPs in many bio-applications, this is usually done using cumbersome post-synthesis purification methods, whereby a complete removal / exchange of surface ligands and noxious chemicals is often not possible.[188, 189]Green synthesis strategies that avoid using toxic surface coating would be therefore of great interest. Using of proteins as surface coatings, shape-directing and stabilizing agents could be a reasonable choice for the synthesis of biocompatible anisotropic NPs.[67]

Implementing nanostructures to imitate the nature's design is a compelling research topic. Nanozymes, which is a group of nanomaterials that possess an intrinsic natural enzyme-mimicking activity, have been recently reported.[190-196]These group of artificial enzymes can overcome many drawbacks of the natural enzymes and offer many advantages such as low-cost, large scale synthesis, time-effective processing and purification and their high stability under stringent conditions. Remarkable advancement in the field of nanozymes have been done since the introduction of iron oxide NPs as artificial peroxidases and cerium oxide (nanoceria) as catalase

¹ The data of this work has been published in [207].

mimics.[195, 197, 198]This inspired some attempts to assess the enzyme-mimicking activity of bimetallic and multimetallic NPs. For instance, various bimetallic and multimetallic NPs have shown artificial peroxidase,[185] oxidase-like[199, 200] and catalase-like activity, such as AgM NPs (M= Au, Pd and Pt),[185] FePt NPs,[199] and Au@ PdPt NPs,[200] among others, and their catalytic activity could be simply tuned by adjusting their elemental composition.

The nanoparticles-based artificial enzymes hold a great potential for sensing applications, as well as other biological applications.[201-205] Despite their unique properties, colloidal/chemical stability, substrate selectivity and biocompatibility of many recent nanozymes are still remaining great challenges. And as such, green synthesis of nanozymes using innocuous chemicals and their coating with intrinsically non-toxic surface capping agents would be of utmost value.

In this work, BSA protein was used for the facile synthesis of biocompatible porous AgPt bimetallic NPs. The biocompatible BSA was employed as a biotemplate, shape-directing and stabilizing agent. The obtained porous AgPt NPs exhibited pH-switchable peroxidase-/catalase-mimetic activity. In addition, the porous structure of the AgPt NPs allows them to be effective cargo carriers, and their pH-dependent peroxidase-like activity facilitates the triggered release of the cargo.

3.2 Results and discussion

3.2.1 Characterization of NPs

The AgPt bimetallic NPs were synthesized through a three-step process (Figure 33a). Firstly, the yellow-colored Ag seeds were synthesized, followed by the synthesis of the purple-colored BSA-coated Ag nanoprisms. Then, AgPt bimetallic NPs were synthesized via the galvanic exchange reaction in the 3rd step. The preformed Ag nanoprism used as a sacrificial template for the controlled deposition of Pt, resulting in the formation of the navy-blue-colored AgPt NPs. The role of BSA in directing the anisotropic growth of the NPs have been evaluated through a set of control experiments (Figures 36-39). The TEM images of AgPt NPs reveal the porous nature of the prism-shaped NPs (Figure 33) with an average edge length (LE) of 44 nm (Figure 34). The HR-TEM images of the AgPt NPs show different lattice orientations of the nanocrystals with d-spacing values between fringes of 0.242 nm and 0.222 nm, similar d-spacing values are assigned to the interplanar spacing of the (111) planes of Ag and Pt (JCPDS No. 04-0783 and 04-0802),

respectively (Figures 35a and 35b). The electron diffraction (ED) pattern of the AgPt NPs shows a diffused ring pattern, which reveals their polycrystalline nature (Figure 35c). The formation of AgPt NPs involves two simultaneous reduction reactions of the Pt precursor via GE reaction with the sacrificial Ag nanoprism, which contributes most, and through the remaining ascorbic acid (AA) in the growth solution, followed by Pt deposition into the preformed Ag nanoprism template and the oxidative dissolution of Ag⁰ to Ag⁺ ions. The reduction rate of Ag⁺ by AA is much lower than the oxidative dissolution rate of the preformed Ag nanoprism by the Pt precursor. This mechanism accounts for the porous nature of the resulting AgPt NPs.

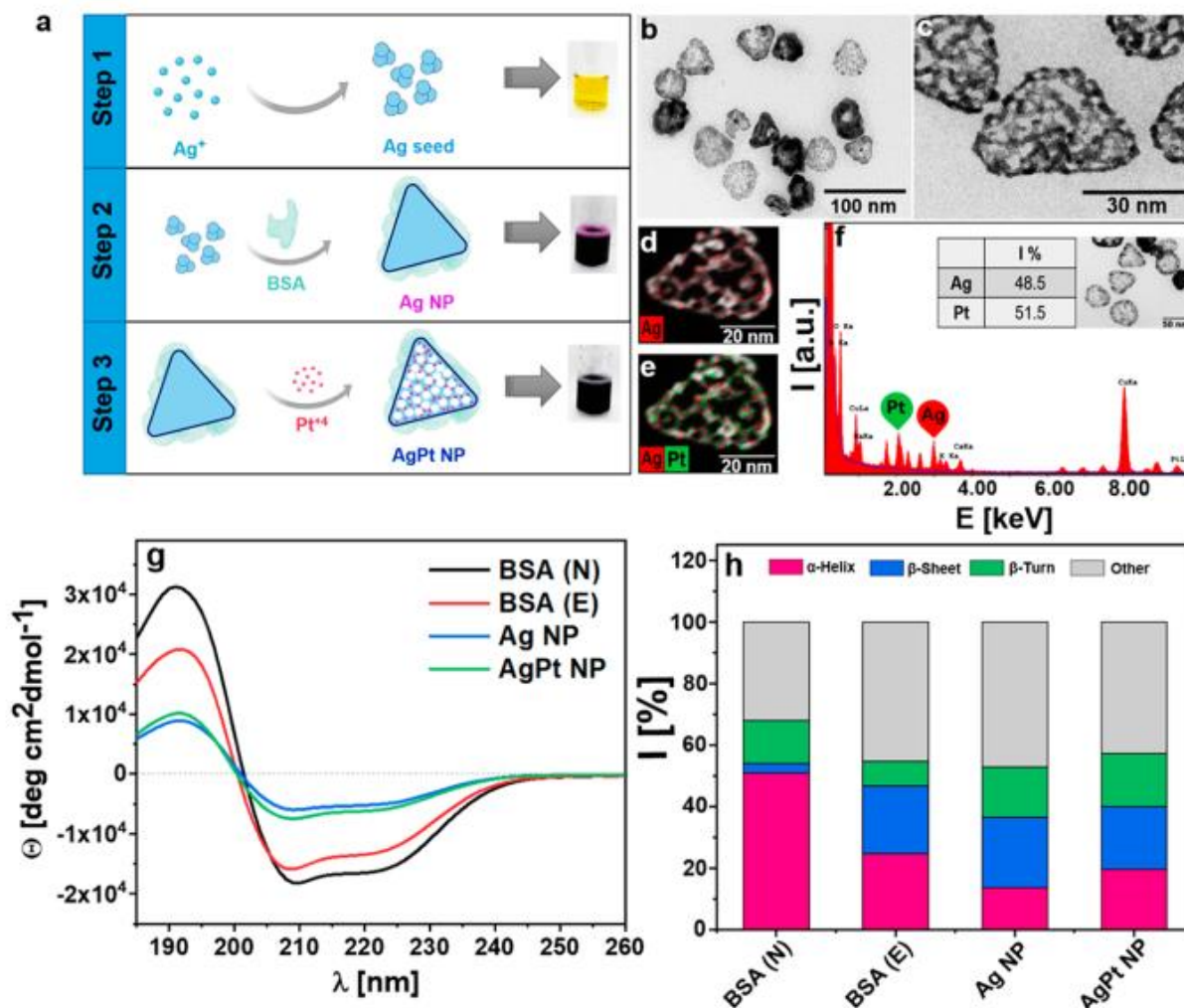


Figure 33. Synthetic route and characterization of AgPt NPs. a) schematic illustration of the synthetic route of AgPt NPs. (b, c) TEM images of the porous AgPt NPs at different magnification. (d, e) EDS elemental mapping of Ag and combination of Ag and Pt in AgPt NPs, respectively. f) EDS analysis of AgPt NP (corresponding to one of the NPs shown in the inset) showing the atomic percentage (I %) of Ag and Pt (table inset). g) CD spectra of Ag NPs, AgPt NPs and BSA solutions (N- and E-forms) and h) their corresponding secondary structure elements distribution (I %). Prepublished in [206].

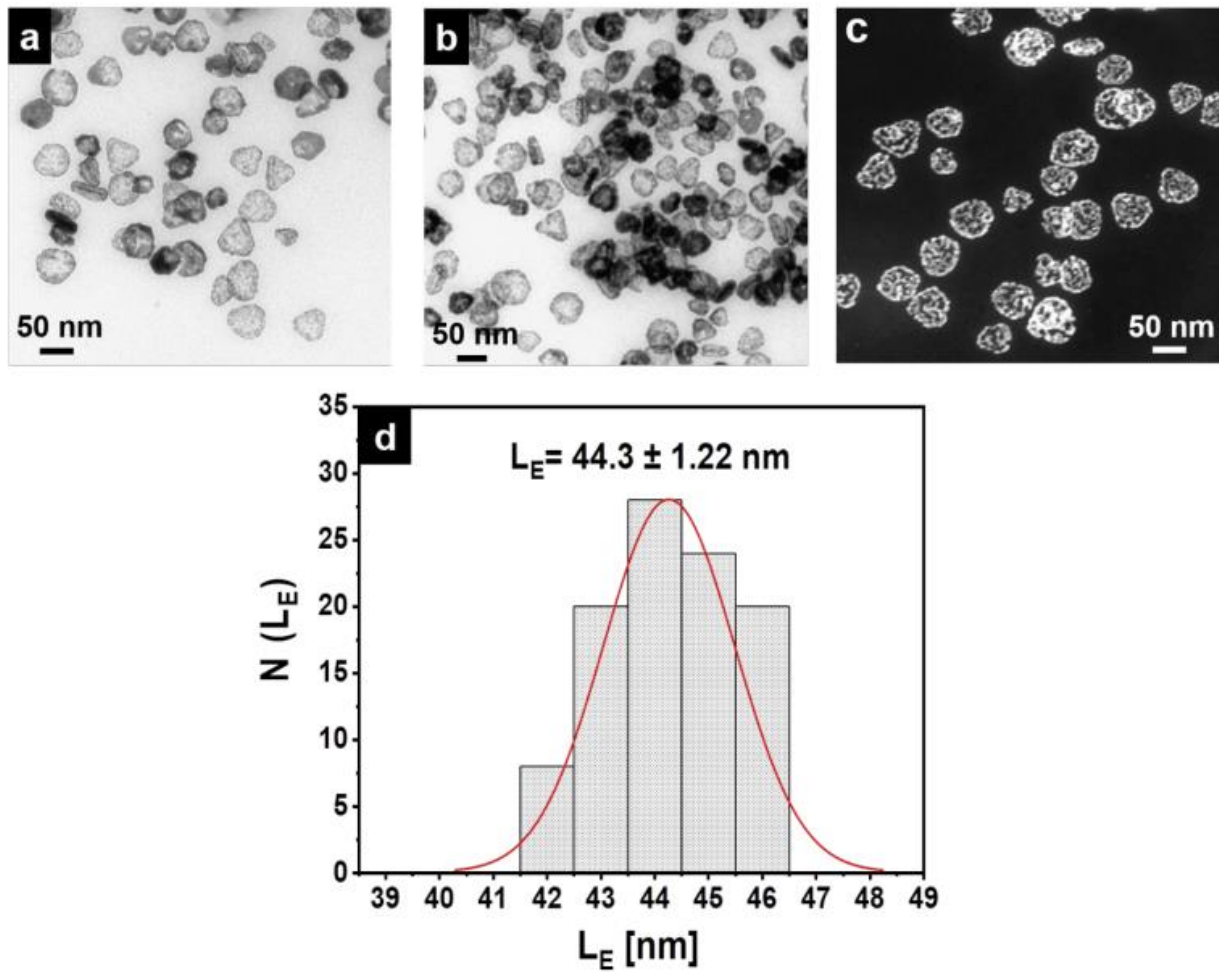


Figure 34. Characterization of the porous AgPt NPs. (a and b) TEM and (c) STEM images of AgPt NPs. d) Size distribution histogram and size distribution Gaussian fitting of the edge length (LE) of AgPt NPs (mean $LE = 44.3 \pm 1.22$ nm, averaged from 100 NPs). Prepublished in [206].

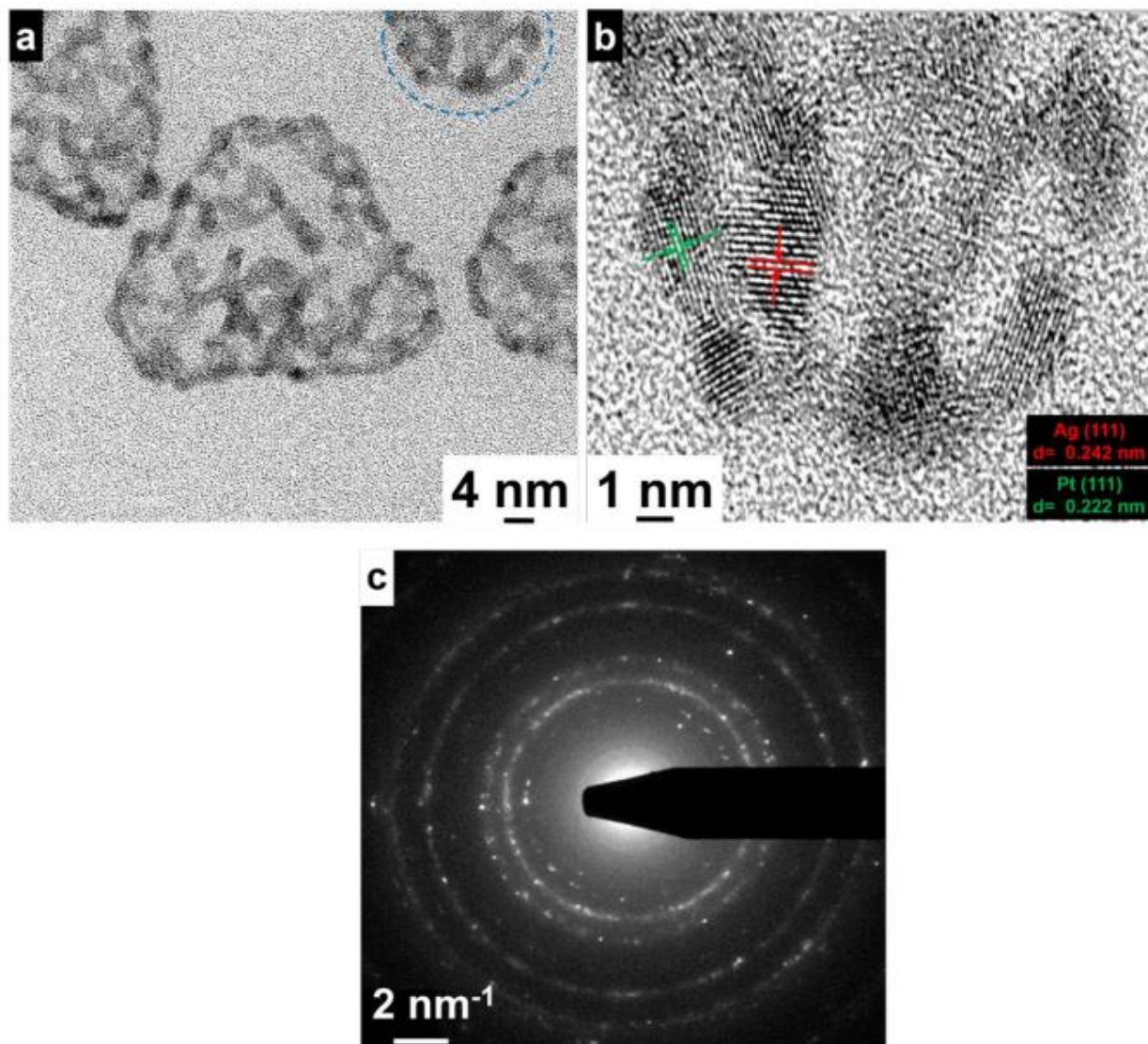


Figure 35. HRTEM and SAED pattern of AgPt NPs. a) HRTEM of AgPt NPs and (b) HRTEM image of the outlined area in (a) showing the d-spacing of Ag and Pt in AgPt NPs. c) SAED pattern of AgPt NPs. Prepublished in [206].

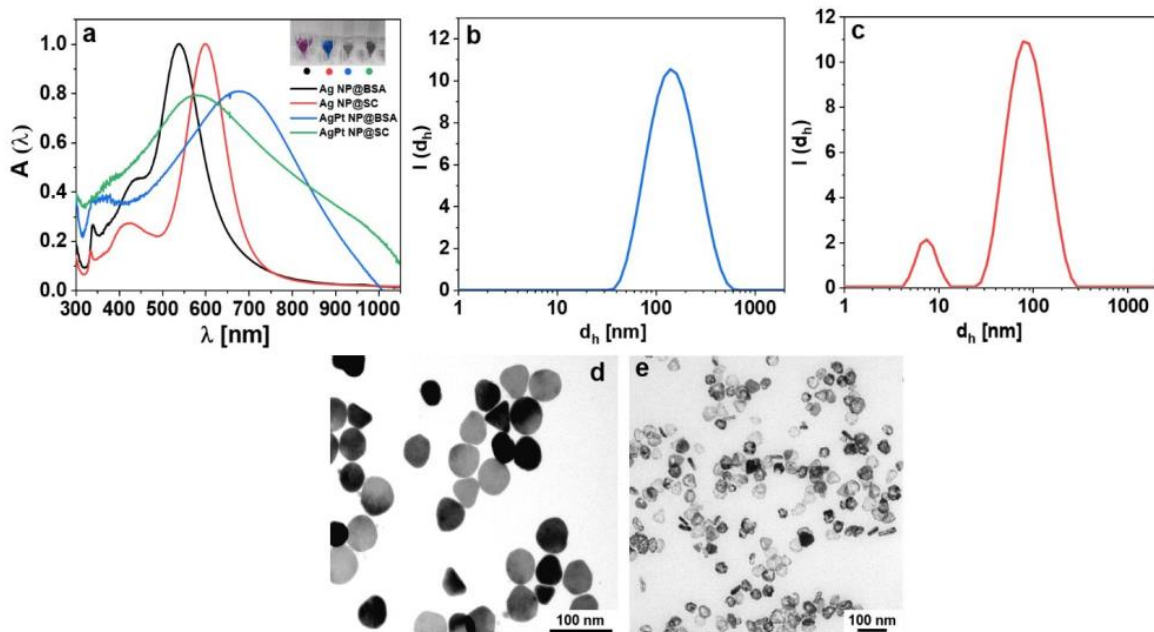


Figure 36. Role of BSA in directing the shape towards porous prism-shaped AgPt NPs. a) UV-vis spectra of Ag NPs@BSA, Ag NPs@SC, AgPt NPs@BSA, and AgPt NPs@SC and their corresponding photographs in the inset. (b and c) d_h of AgPt NPs@SC and AgPt NPs@BSA as recorded in the form of the intensity distribution $I(d_h)$, respectively. (d and e) TEM images of AgPt NPs@SC and AgPt NPs@BSA, respectively. Prepublished in [206].

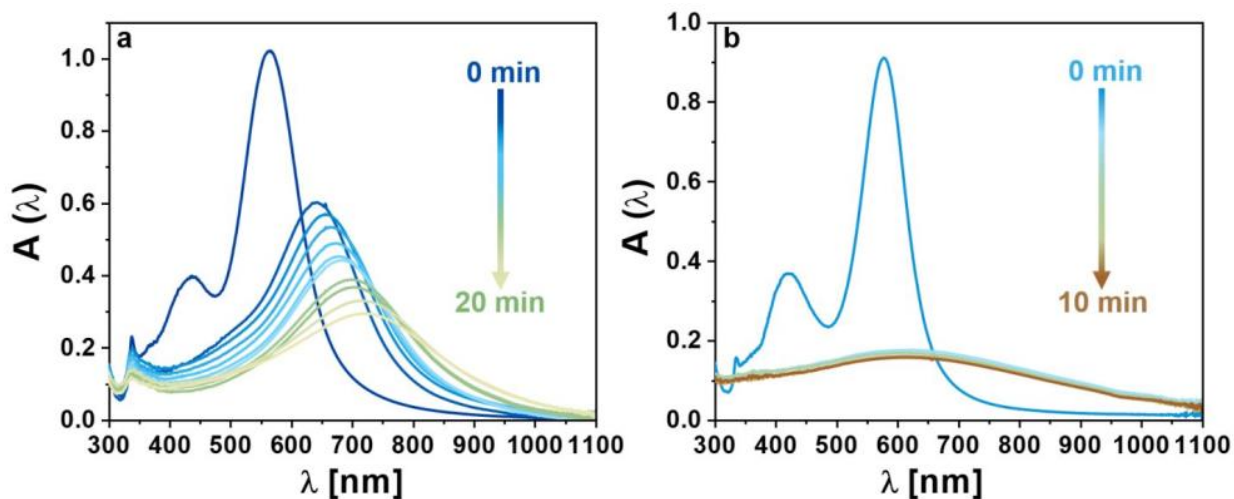


Figure 37. Kinetics of AgPt NPs formation using different surface ligands. (a and b) UV-vis spectra recorded at different time points during the synthesis of AgPt NPs@BSA and AgPt NPs@SC, respectively. Prepublished in [206].

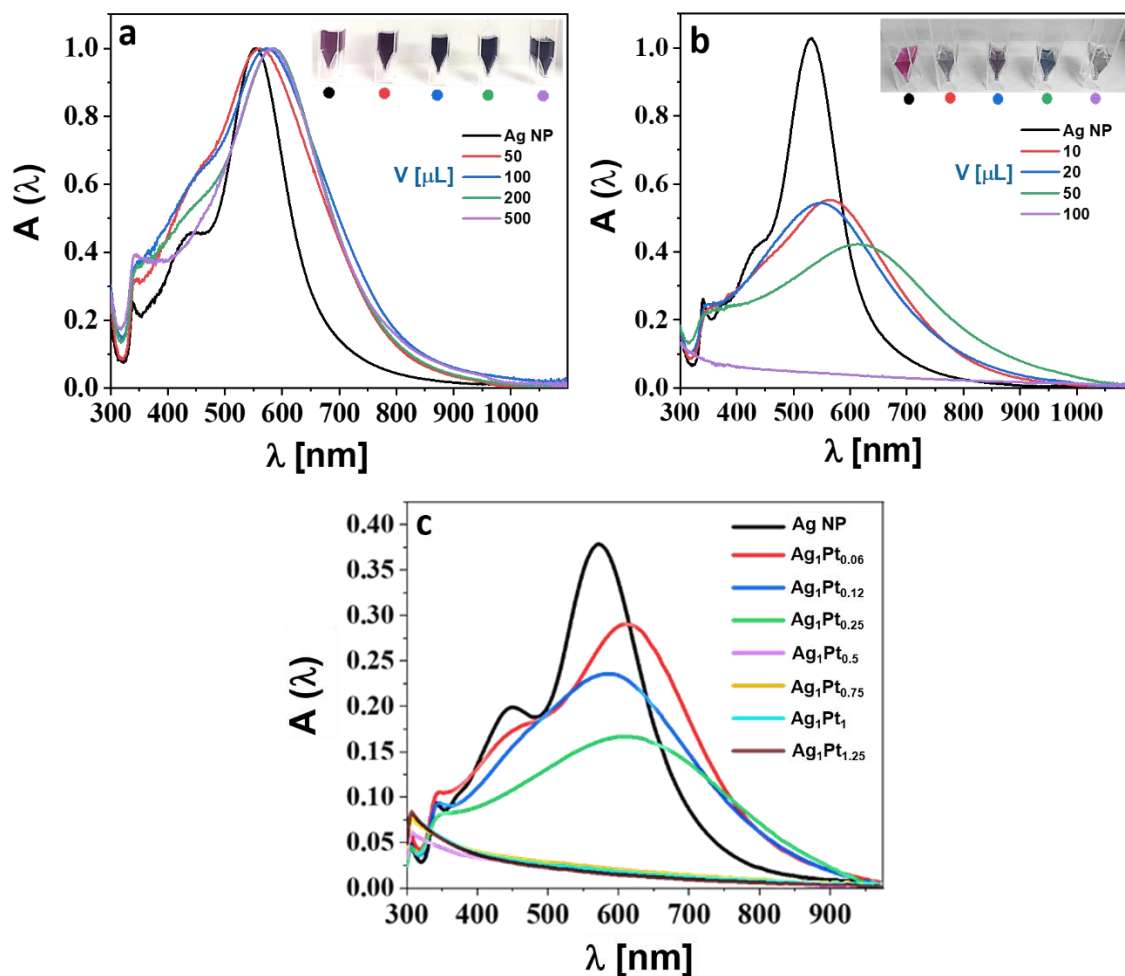


Figure 38. Effect of using different concentrations of Pt precursor (H_2PtCl_6) on the synthesis product. UV-vis spectra of the NPs prepared using different amounts (V) of (a) 2 mM and (b) 25 mM Pt precursor (Insets are the photographs of the obtained). c) UV-vis spectra of AgPt NPs prepared using different molar ratios of Ag and Pt precursors. Prepublished in [206].

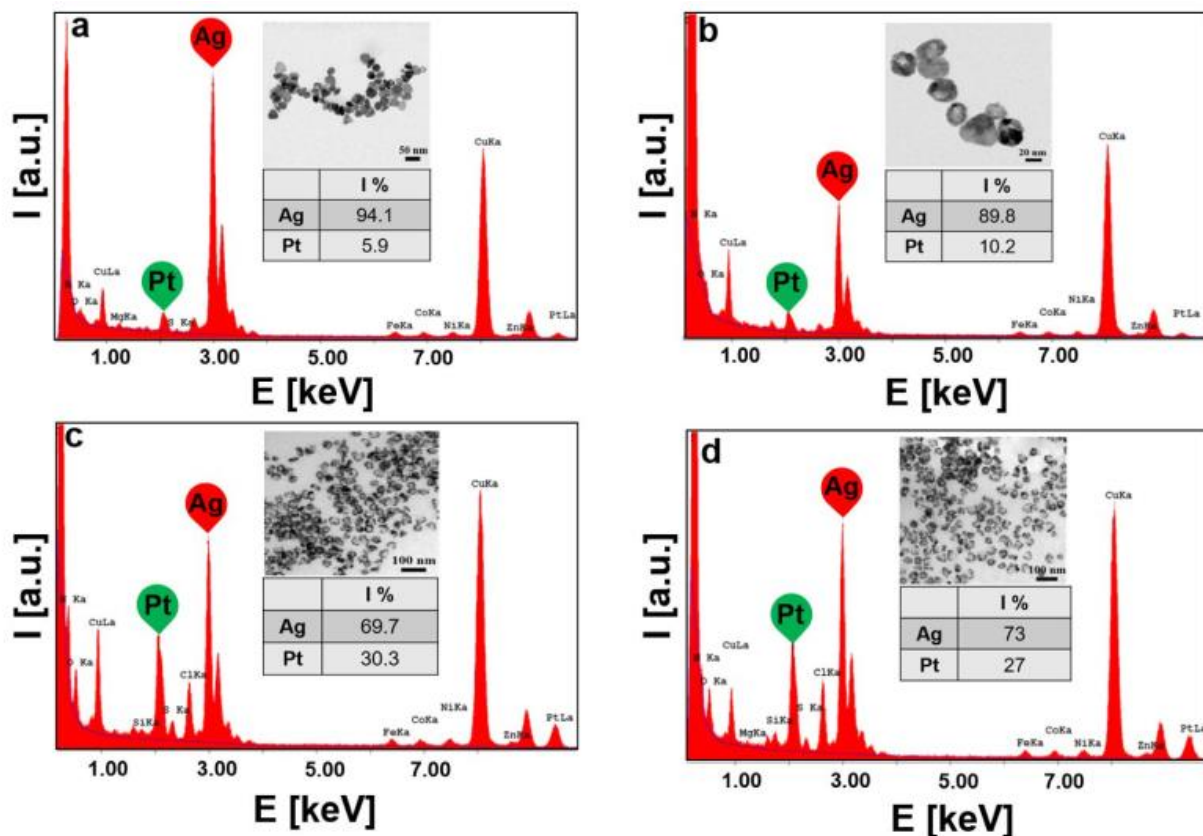


Figure 39. Effect of changing the Ag:Pt molar ratio on the NP shape and composition. (a-d) EDS spectra of AgPt NPs prepared using 5, 10, 50 and 100 mM Pt precursor, respectively. Insets are the corresponding TEM images and tables summarizing the atomic % of Ag and Pt obtained from the EDS spectra. Prepublished in [206].

The deconvoluted X-ray photoelectron spectroscopy (XPS) spectra of AgPt NPs show a broader Ag 3d peak than exhibited by the monometallic Ag nanoprism (Figure 40). The Ag 3d peak in both AgPt and Ag NPs is centered around 368 eV, which corresponds to a state closer to Ag(0) (Figure 41a). In addition, a small peak at 367 eV appeared in the XPS spectra of AgPt which confirms the presence of Ag(I). This was further confirmed by the small peak at ~200 eV in the survey spectra of AgPt NPs (Figure 40). The XPS Pt 4f spectra of AgPt NPs show a peak at 71 eV which indicate the presence of Pt in the Pt(0) oxidation state (Figure 41b).

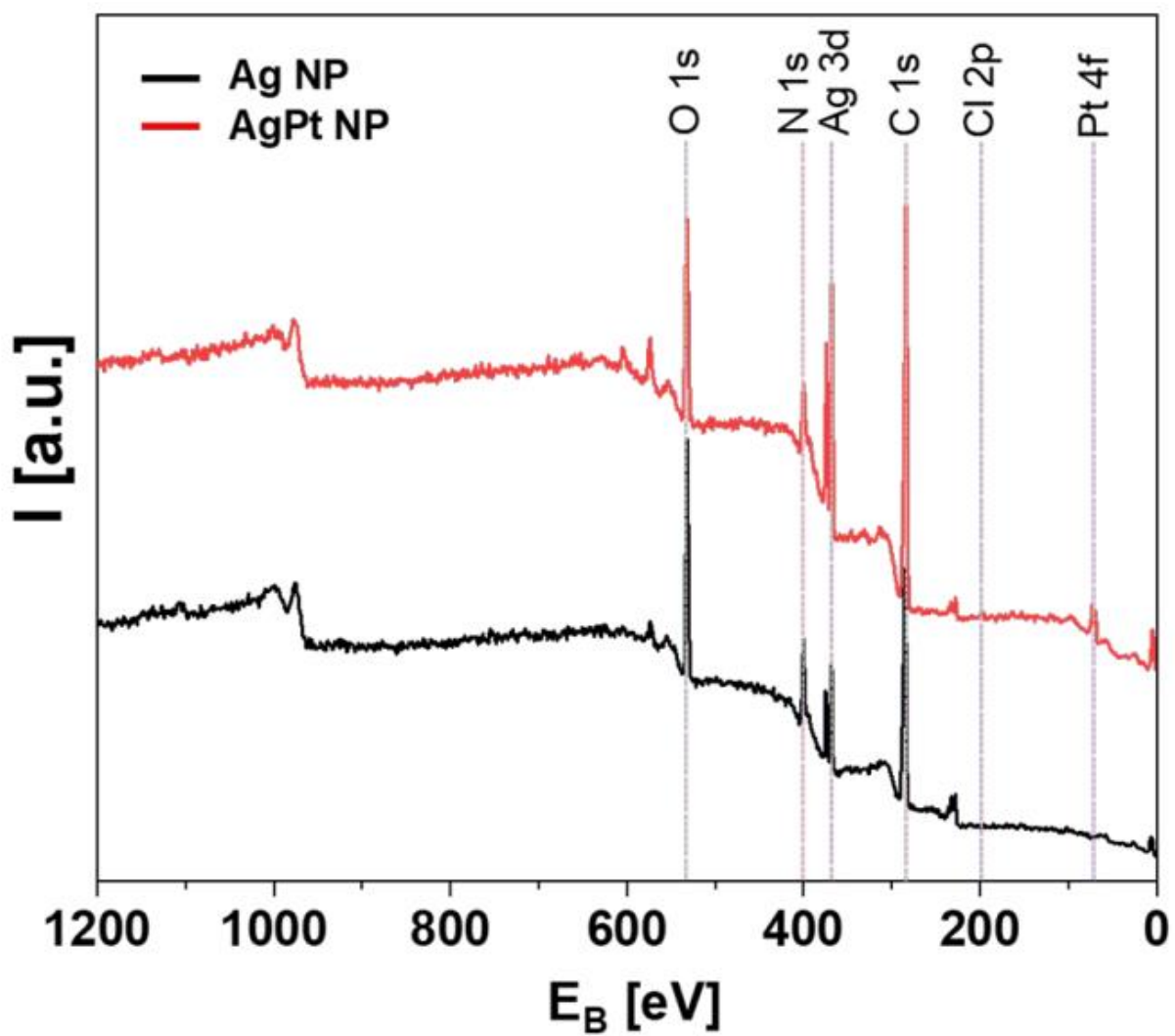


Figure 40. XPS survey spectra of Ag NPs and AgPt NPs. Individual elements are assigned in the spectra. Prepublished in [206].

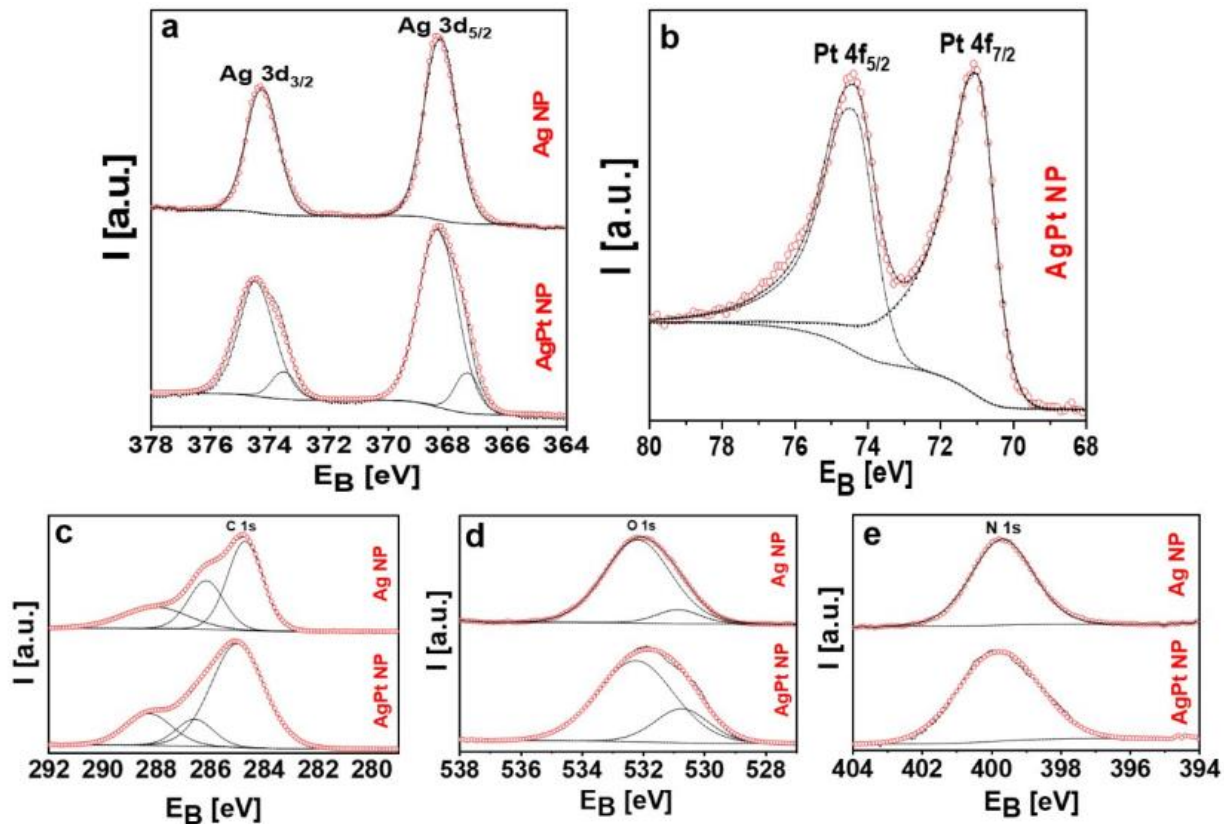


Figure 41. Deconvolution of XPS spectra of Ag NPs@BSA and AgPt NPs@BSA. Deconvoluted XPS spectra of Ag3d (a), Pt4f (b), C1s (c), O1s (d) and N1s (e) respectively. All the spectral features were fitted into the different chemical species expected. Prepublished in [206].

Elemental mapping of AgPt NPs using STEM with dual EDS revealed the coexistence of Ag (48.5%) and Pt (51.5%) and their homogeneous distribution in the bimetallic NPs (Figure 33 d–f).

The morphology as well as the elemental distribution of AgPt NPs can be easily tuned by adjusting the Ag:Pt molar ratio used during the synthesis (Figure 39). A perfectly prism-shaped AgPt NPs with controlled porosity could be obtained using Ag:Pt molar ratio of 1:0.25, and was chosen therefore for further investigations.

The formation kinetics of AgPt NPs as studied by the UV-vis spectra revealed the apparent changes in the UV-vis spectra of Ag NPs after the GE reaction with Pt (Figure 37a). Once the Pt precursor introduced to the Ag NPs, a gradual red-shift, broadening as well as decrease in the plasmonic peak corresponding to the in-plane dipole resonance of Ag NPs takes place with complete loss of the in-plane quadrupole plasmon resonance. Thus, the ability to tune the plasmonic peaks of Ag

NPs to NIR region could be done simply by introducing a second noble metal such as Pt, this plasmonic peak of AgPt NPs could be further tuned to span broad range of the NIR region by adjusting the synthesis parameters, this could be of utmost importance for various biomedical applications. The bathochromic shift observed in AgPt NPs is mainly due to changes in the refractive index of the resulting porous nanostructure, similar trend have been previously reported.[207]

The synthesis pathway of AgPt NPs could be extended to synthesize other AgM bimetallic NPs such as AgAu and AgPd NPs (Figures 42 - 44).

The effect of pH on the reaction product was studied and the results clearly reveal that the GE reaction is pH-dependent and the galvanic exchange between the Pt and the preformed Ag nanoprism scaffold takes place mainly at acidic pH (pH ~4) leaving behind a porous AgPt nanostructure with its characteristic plasmonic bands as could be confirmed by the UV-vis absorption spectra (Figure 45). Similar observations were obtained for other bimetallic and multimetallic NPs.[208, 209]

The CD as well as the fluorescence spectra of BSA were recorded in order to trace the conformational changes of the surface capping agent during the synthesis of Ag and AgPt NPs.

The native BSA (N-form, pH 6.5) exhibits single CD spectroscopic band at 190 nm in the positive absorption side and two other CD bands at approximately 210 and 225 nm in the negative absorption side, which are attributed to the helical structure of BSA[168] (Figure 33g).

Deconvolution of the CD spectra shows that the nearly neutral BSA solution is made up of 51% α -helix, 3% β -sheet, 14% turns, and 32% irregular structures (Figure 33h and Figure 46a), which is in agreement with the reported values.[166, 210]

Deconvolution of the CD spectra of acidified BSA solution, which mimic the reaction conditions, revealed that the configuration of BSA contains ca. 25% α -helix, 22% β -sheet, 8% β -turn, and 45% other structures (Figure 33h and Figure 46b), which means that BSA unfolds at such pH and adopts an extended configuration (E-form).[211, 212]

Compared to the N-configuration, a significant decrease in the α -helical configuration of the BSA was observed in BSA-capped Ag and AgPt NPs (Figure 33h, Figure 46c and 46d). Furthermore,

an additional decrease in the α -helix structural conformation of Ag and AgPt NPs (14% and 20%, respectively) was observed, compared to the E-form of BSA (25%). These results reflect a strong interaction between BSA and the metal ions/atoms takes place,[167] which gives rise to an extra unfolding of the E-configuration of the BSA, which employs more reduction in the α -helical conformation.

The findings from the fluorescence spectra matched well with the results gained from deconvolution of the CD spectra. A drastic drop in the fluorescence intensity of Ag NPs and AgPt NPs compared to N- and E-forms of BSA was observed (Figure 47). These results further confirm the BSA unfolding during the formation of Ag NPRs and AgPt NPs.

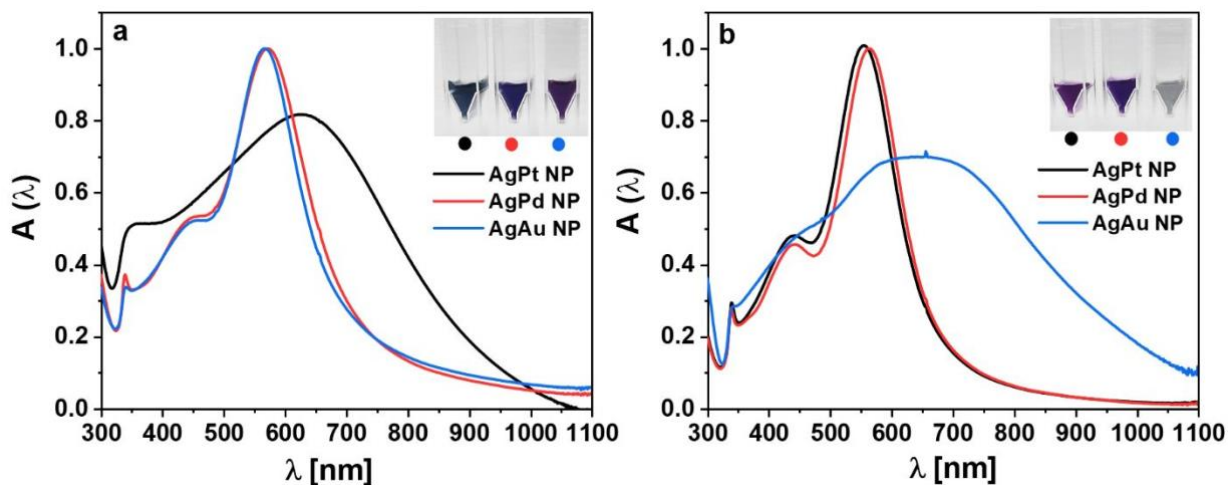


Figure 42. Characterization of AgM@BSA NPs. UV-vis spectra of bimetallic AgM NPs synthesized at (a) pH 4 and (b) pH 11, respectively (Insets are the photographs of the corresponding AgM NPs). Prepublished in [206].

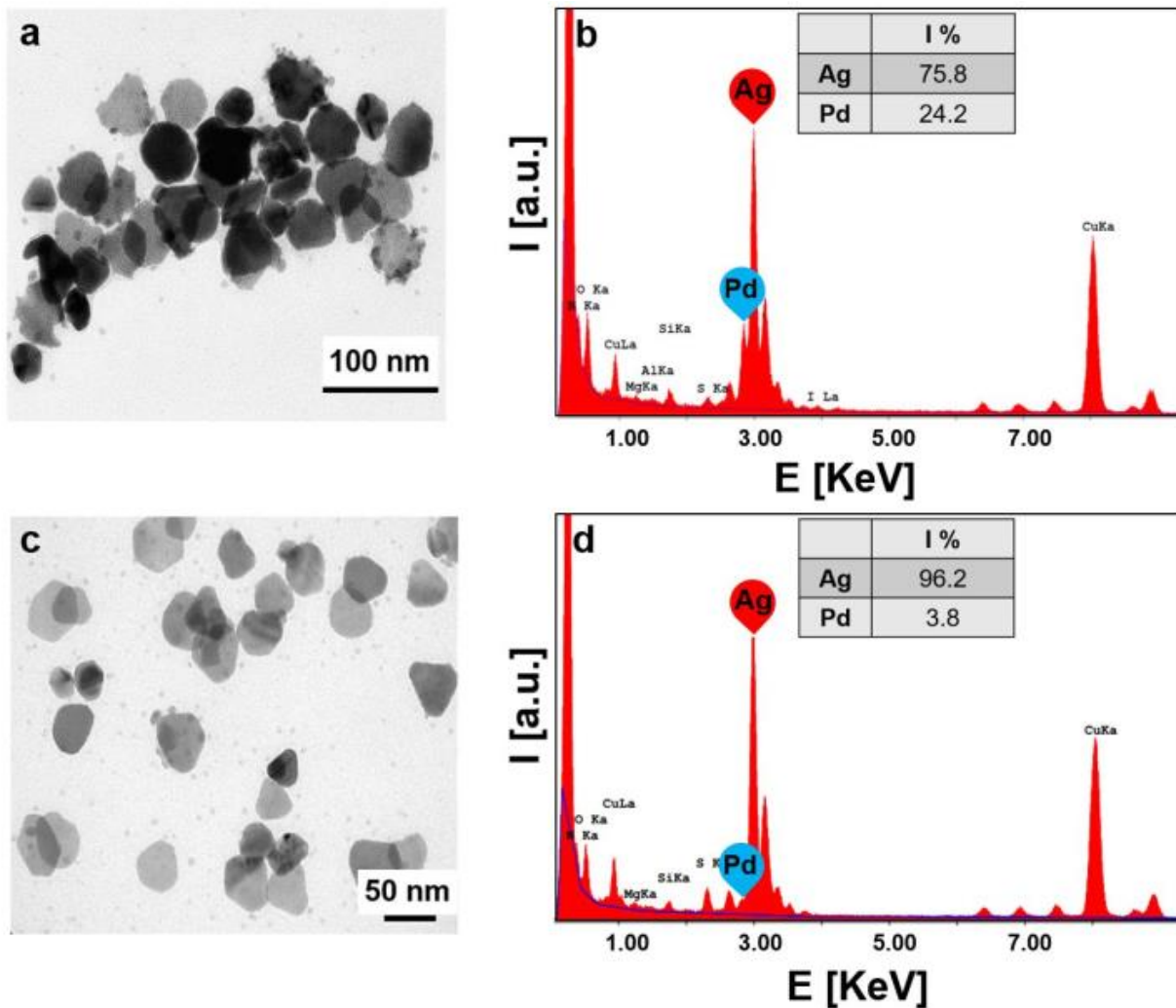


Figure 43. Characterization of AgPd@BSA NPs. TEM images and EDS spectra of AgPd NPs prepared at (a-b) pH 4 and (c-d) pH 11, respectively. Insets in (b) and (d) are the corresponding atomic % of Ag and Pd in the obtained NPs. Prepublished in [206].

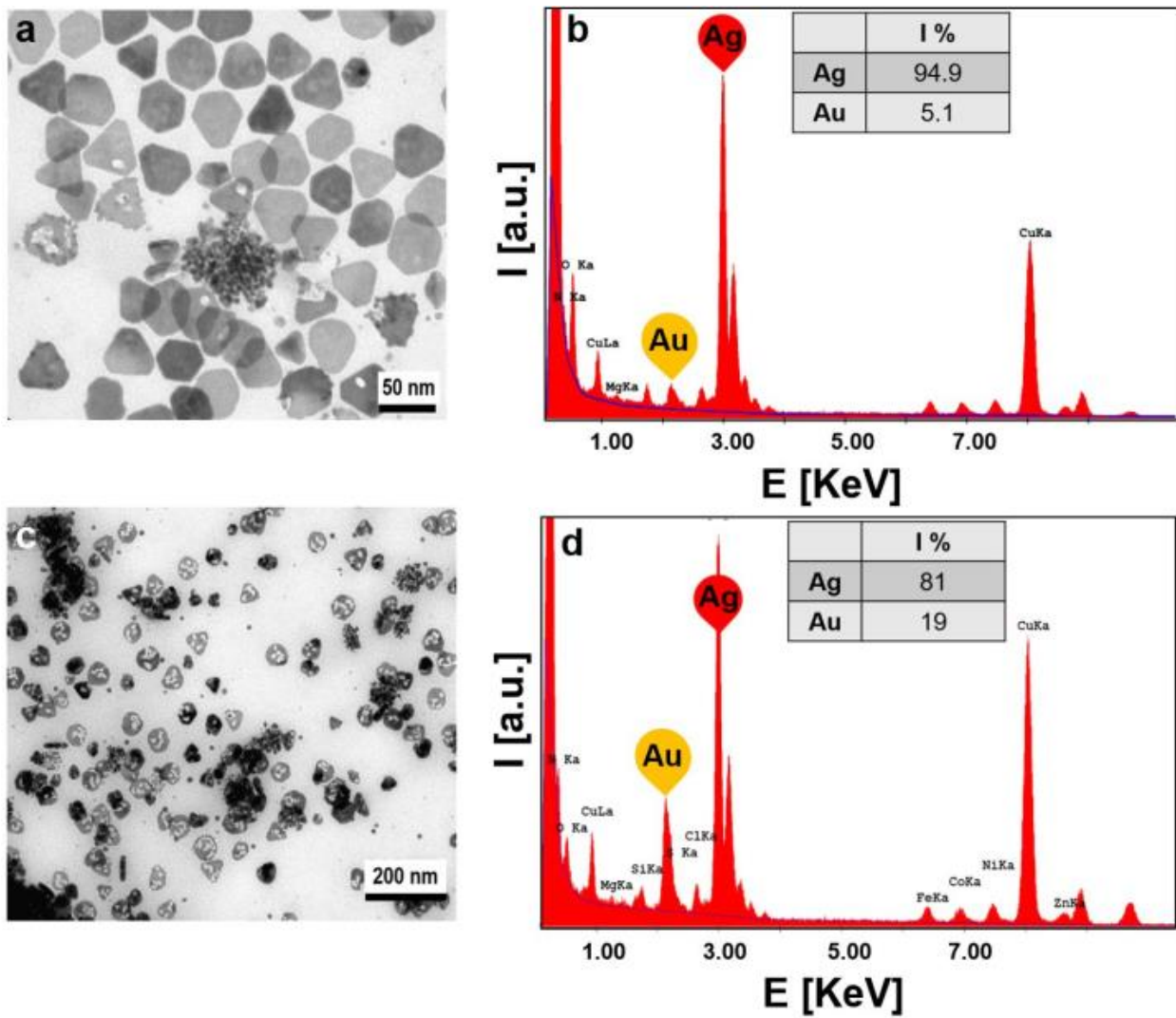


Figure 44. Characterization of AgAu@BSA NPs. TEM images and EDS spectra of AgAu NPs prepared at (a-b) pH 4 and (c-d) pH 11, respectively. Insets in (b) and (d) are the corresponding atomic % of Ag and Au in the obtained NPs. Prepublished in [206].

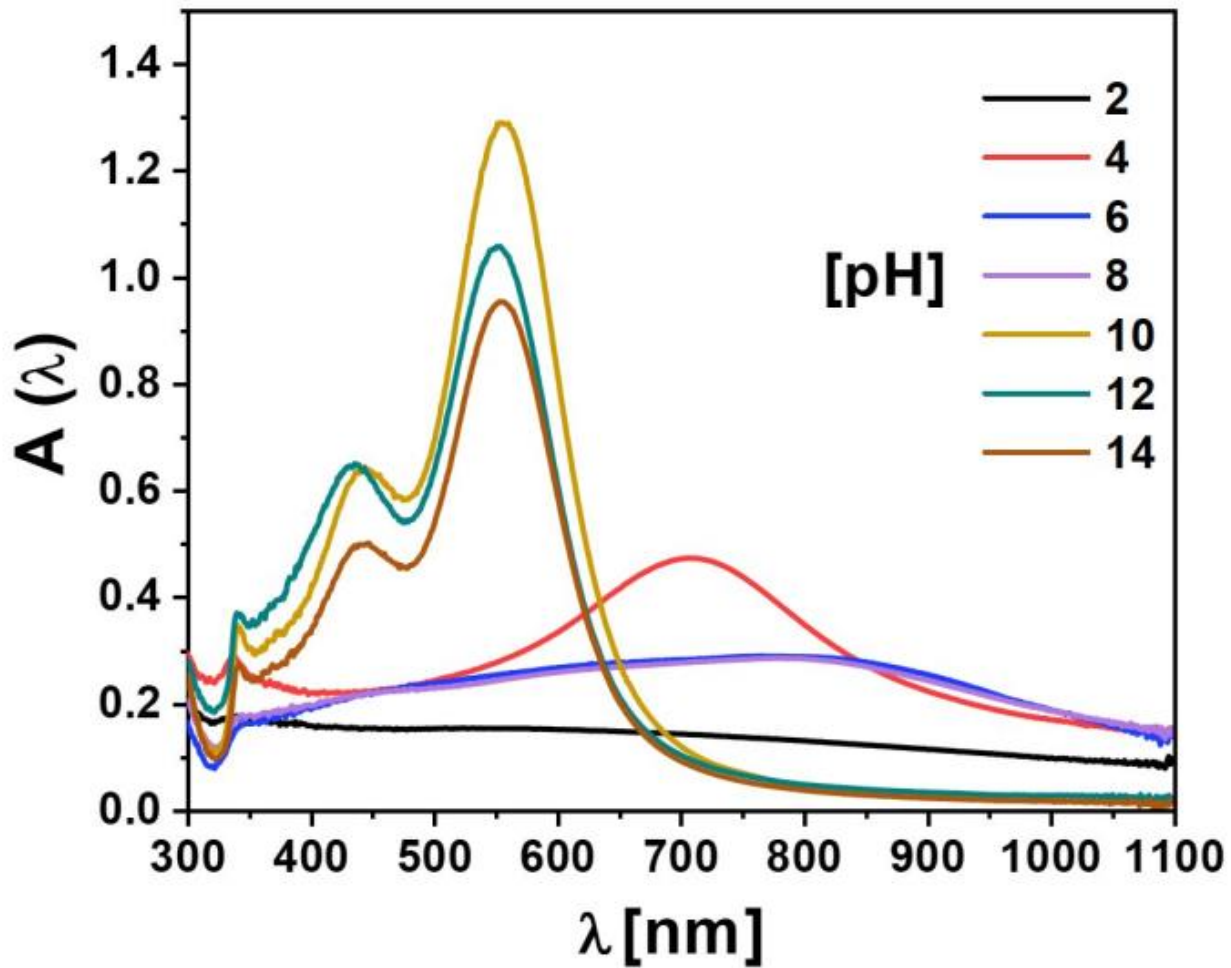


Figure 45. Effect of pH on the synthesis of AgPt NPs. UV-vis spectra of different reaction products synthesized at wide range of pH (2-14). Prepublished in [206].

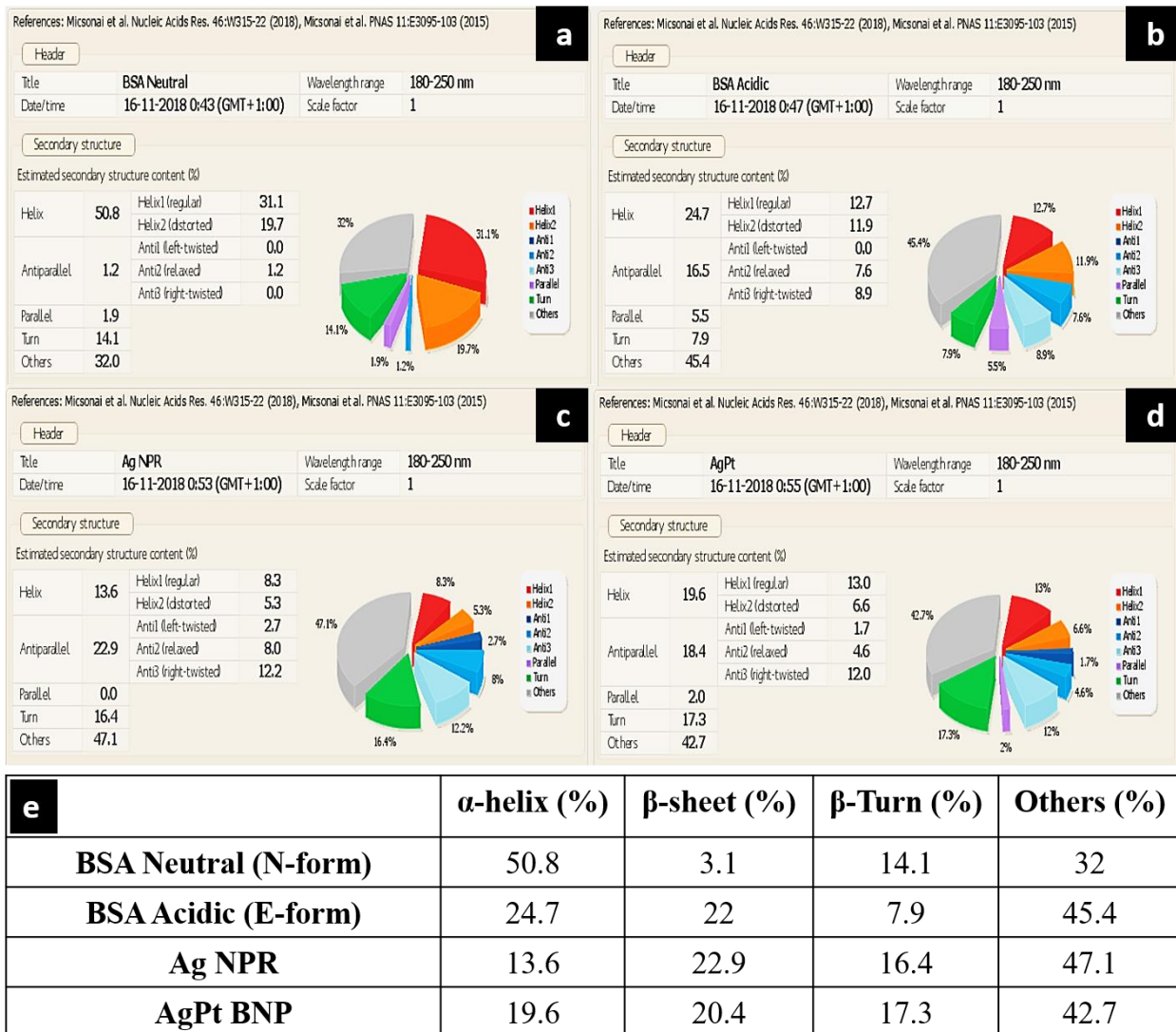


Figure 46. Deconvolution of CD results. Distribution of secondary structure elements of BSA within the a) N- and b) E-forms of BSA, c) Ag NPs and (d) AgPt NPs as estimated from the CD spectra using CD spectra deconvolution online tool <http://bestsel.elte.hu> and e) their corresponding relative content (%) of secondary structure elements. Prepublished in [206].

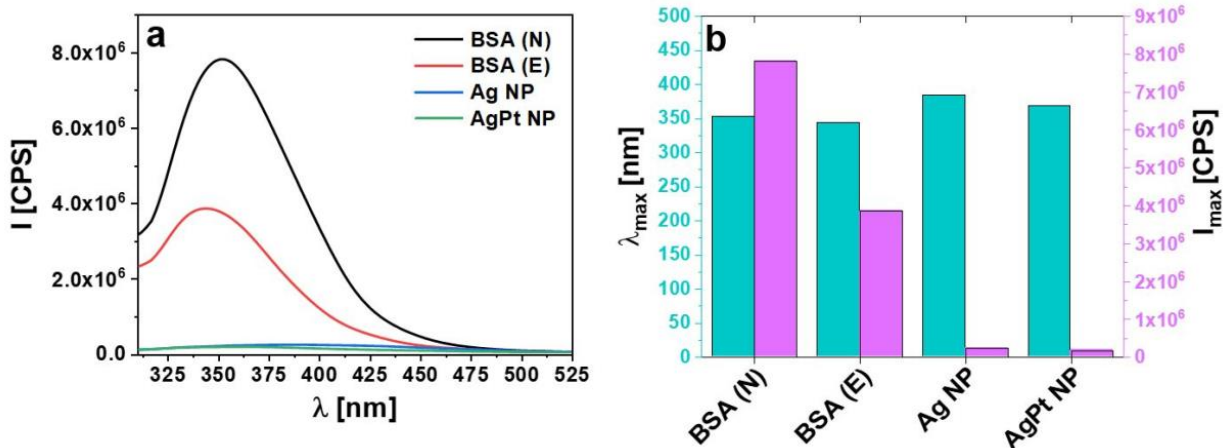


Figure 47. The structural changes of BSA during the synthesis of Ag NPs and AgPt NPs. a) fluorescence spectra of the N- and E-forms of BSA, Ag NPs, and AgPt NPs and b) their peak emission intensity (I_{max}) and peak emission wavelength (λ_{max}). Prepublished in [206].

3.2.2 Colloidal stability of AgPt NPs

As it is important for a nanozyme to be colloidal stable in different media, the colloidal stability of AgPt NPs in high ionic strength medium as well as other biological media was studied.

The AgPt NPs exhibited superior colloidal stability in NaCl solutions of different ionic strengths, as well as in PBS, FBS-free/-supplemented DMEM and RPMI media compared to the monometallic Ag NPs (Figure 48). The relatively superior colloidal stability of the bimetallic AgPt NPs over Ag NPs results from their porous structure. The porous structure of AgPt NPs increases their surface area which implies increased surface coverage with BSA in comparison to the solid structure of Ag NPs. The intrinsic amphiphilic properties of BSA[213] endow the AgPt NPs more colloidal stable, this is most probably due to the increased interfacial energy upon increasing coating with BSA, which forms a mechanical barrier against aggregations. [214]

On the other hand, incorporation of Pt in the AgPt NPs significantly enhances their electrochemical behavior compared with the monometallic Ag NPs. For instance, the internal electron traps formed within the bimetallic AgPt NPs may prevent the oxidative dissolution and etching of Ag scaffold which takes place easily in case of the monometallic Ag NPs, hence, doping the nanostructure with Pt confers them more chemically stable. Similar findings showing the increased chemical stability of bimetallic nanostructures upon alloying Ag NPs with Pt have been reported.[182]

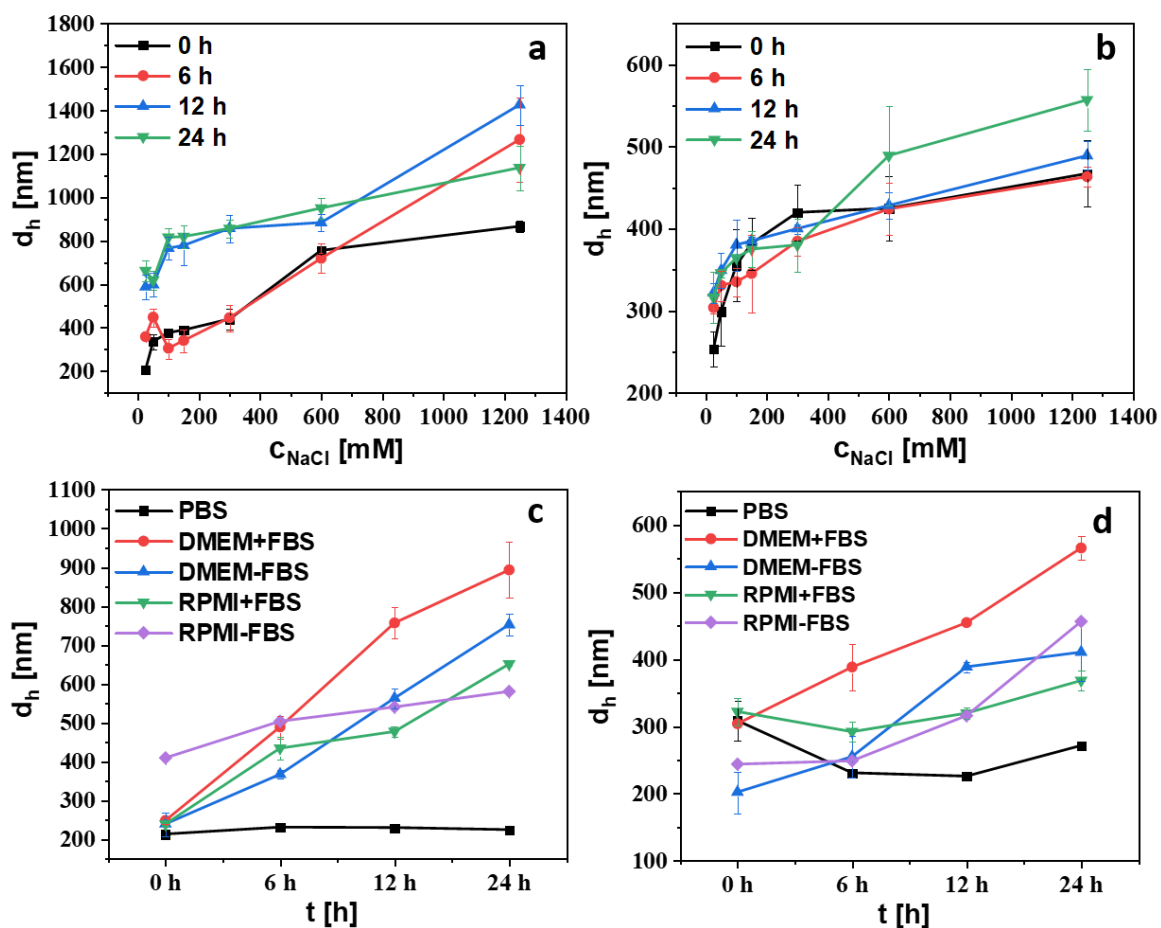
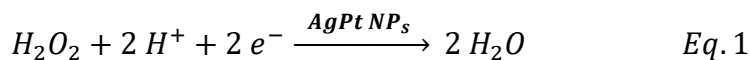


Figure 48. Colloidal stability of Ag NPs and AgPt NPs. Hydrodynamic diameters of (a and c) Ag NPs and (b and d) AgPt NPs in NaCl solutions and in different biological media, respectively. Prepublished in [206].

3.2.3 Enzyme-mimic activity of AgPt NPs

The pH-dependent nanzoyme activity of AgPt NPs was studied by assessing their peroxidase and catalase mimic catalytic activity. The artificial peroxidase activity of AgPt NPs, on one hand, was evaluated by checking their ability to catalyze the oxidation of ortho-phenylenediamine (OPD), a common peroxidase enzyme substrate, in the presence of hydrogen peroxide (H_2O_2). The evolution of the yellow-colored oxidation product of OPD is the 2,3- diaminophenazine (DAP) could be traced using the UV-vis spectrophotometer. On the other hand, the catalase-like activity of AgPt NPs could be evaluated by measuring the dissolved oxygen level resulted from the catalytic decomposition of H_2O_2 .

The AgPt NPs exhibited a conspicuous peroxidase-mimicking activity at acidic pH (pH ~4), this activity could be seen by the relatively faster buildup of the yellow-colored DAP as well as the progressive evolution of the characteristic DAP absorption band ($\lambda = 425$ nm), compared to control, the standard horseradish peroxidase enzyme and the monometallic Ag NPs (Figures 50 and 51). Furthermore, the experiments not only show a pH-dependency (Figure 50) but also changing the elemental composition of the bimetallic NPs and doping with certain amounts of Pt enhances their peroxidase-like activity with AgPt NPs prepared using Ag:Pt molar ratio of 1:0.5 exhibited the highest catalytic activity (Figure 49f, Figure 52). It worth mentioning here that a nanoparticle entirely made of Ag, i.e. the Ag NPs template, show very little to negligible peroxidase-mimicking activity and doping with Pt is necessary to exhibit such catalytic activity (Figures 49c, 49e, 50 and 51c). These results clearly suggest that the peroxidase-mimicking activity AgPt NPs stemming mainly from the Pt metal content of the bimetallic NPs, such catalytic activity may be related to the electron-transfer capability of Pt as previously reported in many electron-transfer reactions (Eq. 1), as such the captured electron could be transferred to the H_2O_2 adsorbed on the surfaces of the AgPt NPs which leads subsequently to the decomposition of H_2O_2 . [215, 216]



To assess whether coating of AgPt NPs with relatively larger surface ligand, such as BSA, passivate their surfaces to a degree that reduces the accessibility of active sites of AgPt NPs and hence their peroxidase-mimic activity, a control experiment to evaluate the peroxidase-like activity of citrate-capped AgPt NPs (AgPt@SC) was carried out. The obtained results reveals almost similar catalytic activity with no evidence of surface passivation by the BSA (Figures 53 and 54).

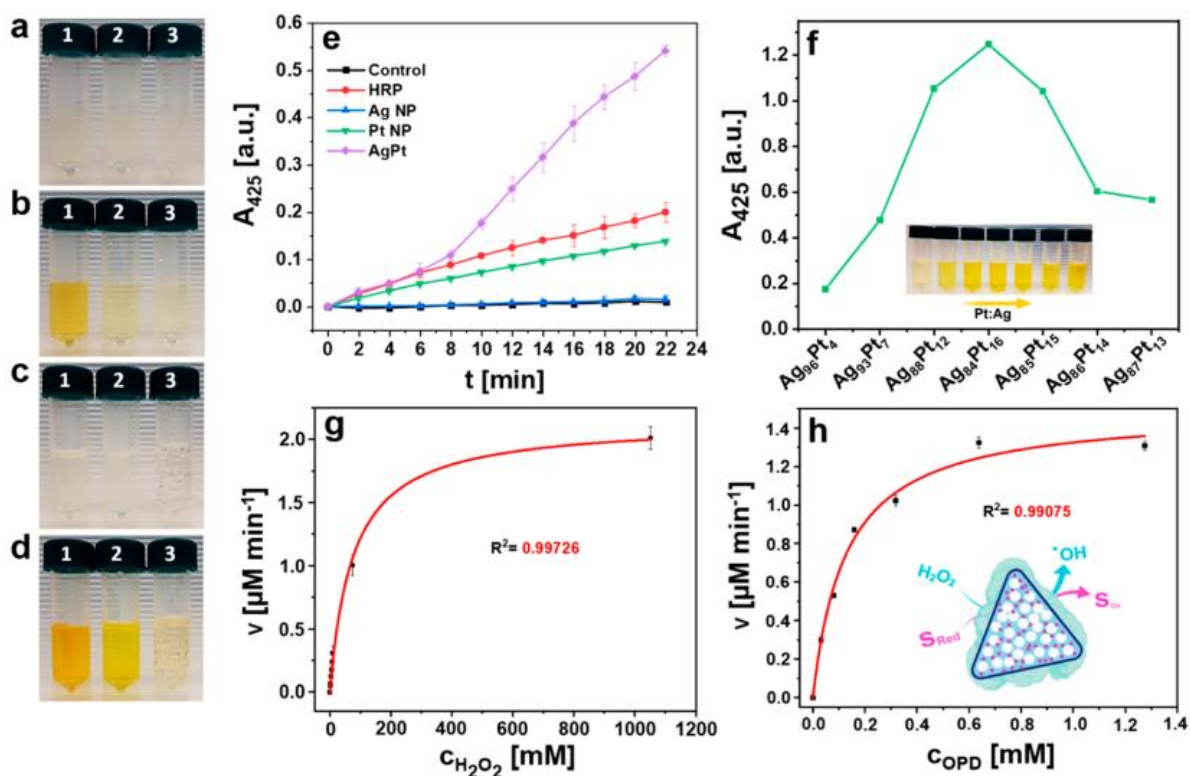


Figure 49. Peroxidase-like activity of AgPt NPs and steady-state kinetics of the catalytic reaction. Photographs of the peroxidase-like activity of a) control, b) horseradish peroxidase (HRP), c) Ag NPs, and d) AgPt NPs at different pH (“1”, “2”, and “3” represents pH 4, pH 7, and pH 11, respectively). e) Time-dependent absorbance changes at $\lambda = 425$ nm upon oxidation of OPD to DAP. f) Elemental composition-dependent peroxidase-like activity of AgPt NPs. The inset shows the corresponding photographs. (g and h) Steady-state kinetics of the catalytic reaction where the rate of reaction (v) was plotted versus different concentrations of H_2O_2 ($C_{H_2O_2}$) while keeping the OPD concentration fixed and while keeping H_2O_2 concentration fixed, respectively. The inset in (h) shows the schematic illustration of the peroxidase-like activity of AgPt NPs. The error bars represent the standard deviation of three measurements. The (R^2) value represents the correlation coefficient. Prepublished in [206].

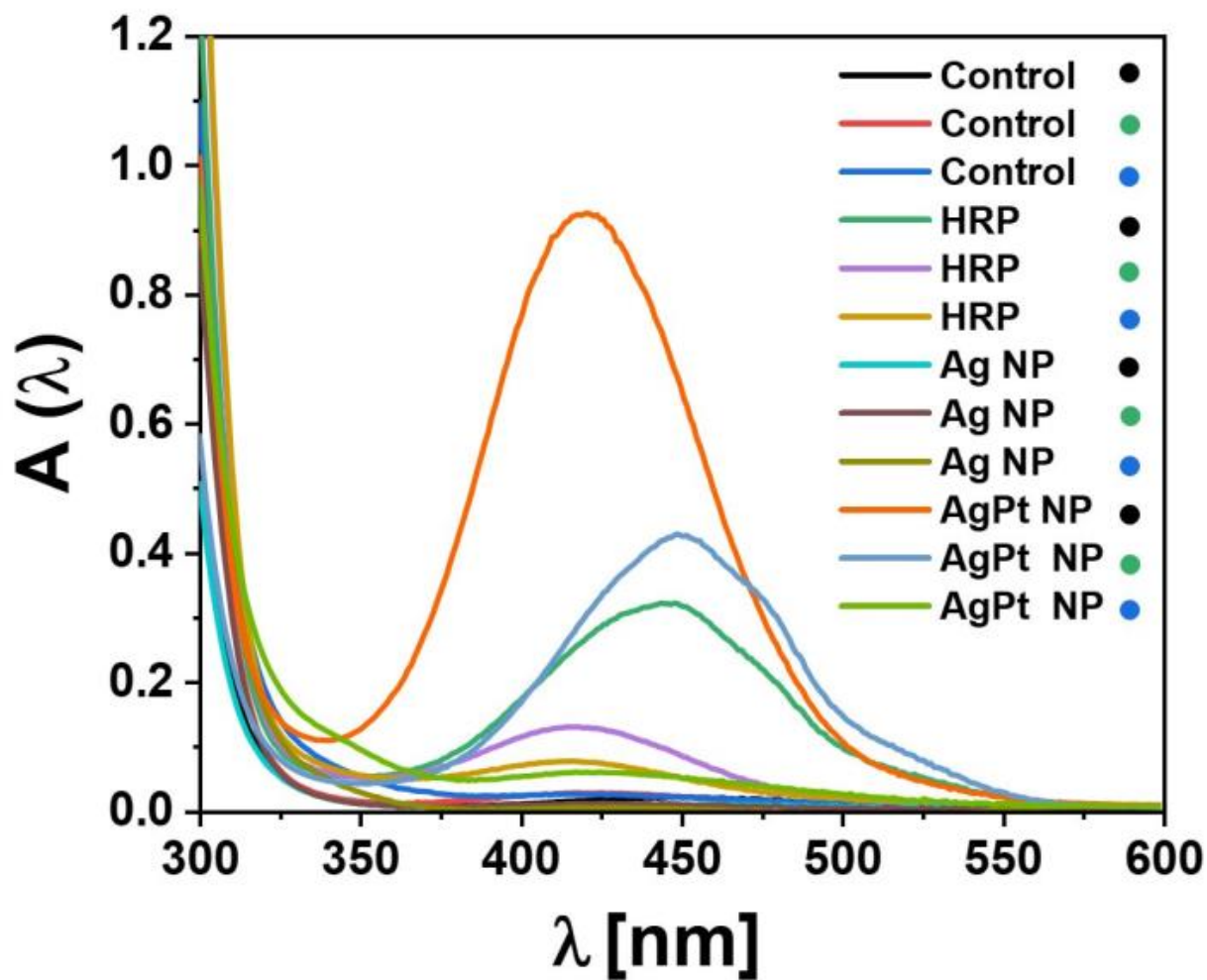


Figure 50. Peroxidase-like activity of AgPt NPs at different pH. UV-vis absorption spectra of the oxidation product of OPD by control, HRP, Ag NPs, and AgPt NPs at different pH (pH 4: black circle, pH 7: green circle and pH 11: blue circle). Prepublished in [206].

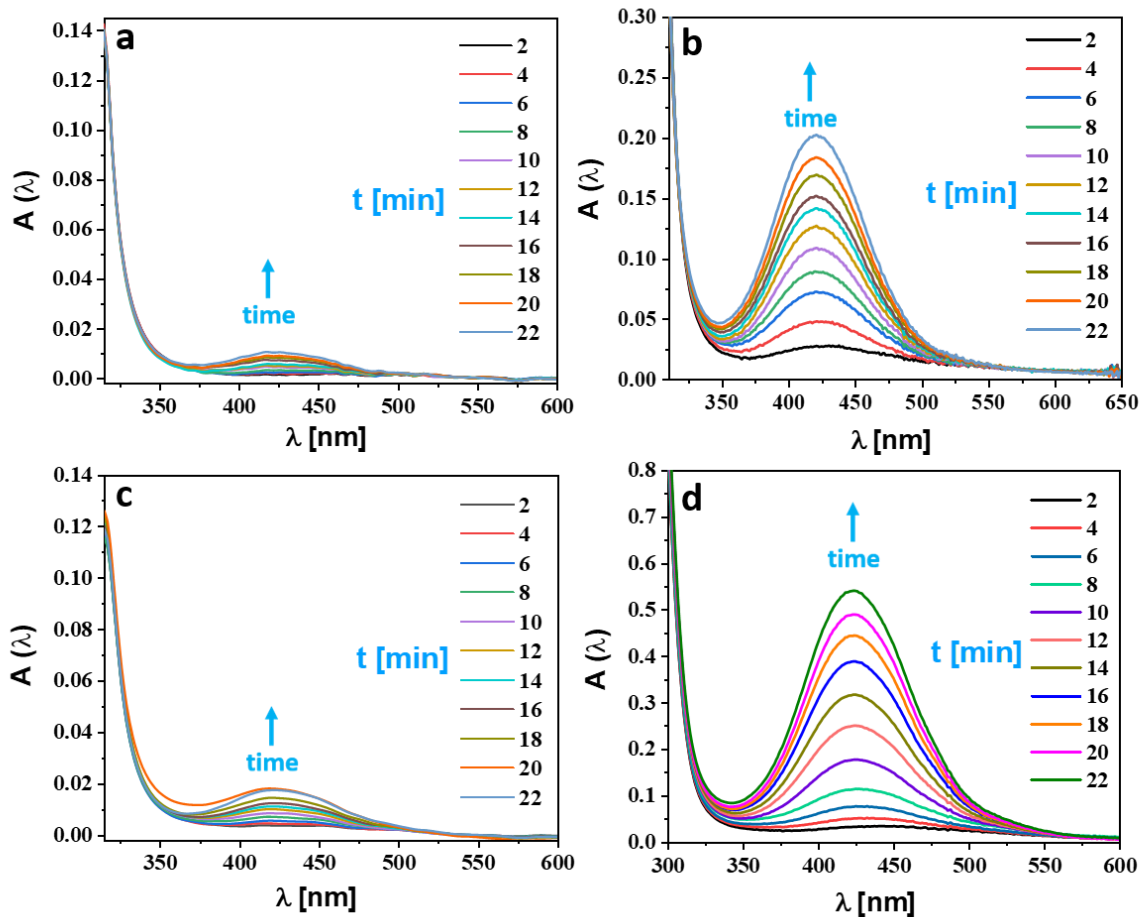


Figure 51. Kinetics of OPD oxidation using AgPt@BSA NPs. Time-dependent absorbance spectra of the DAP generated upon oxidation of OPD a) in absence of catalyst and in presence of b) HRP, c) Ag NPs, or d) AgPt NPs at pH 4. Prepublished in [206].

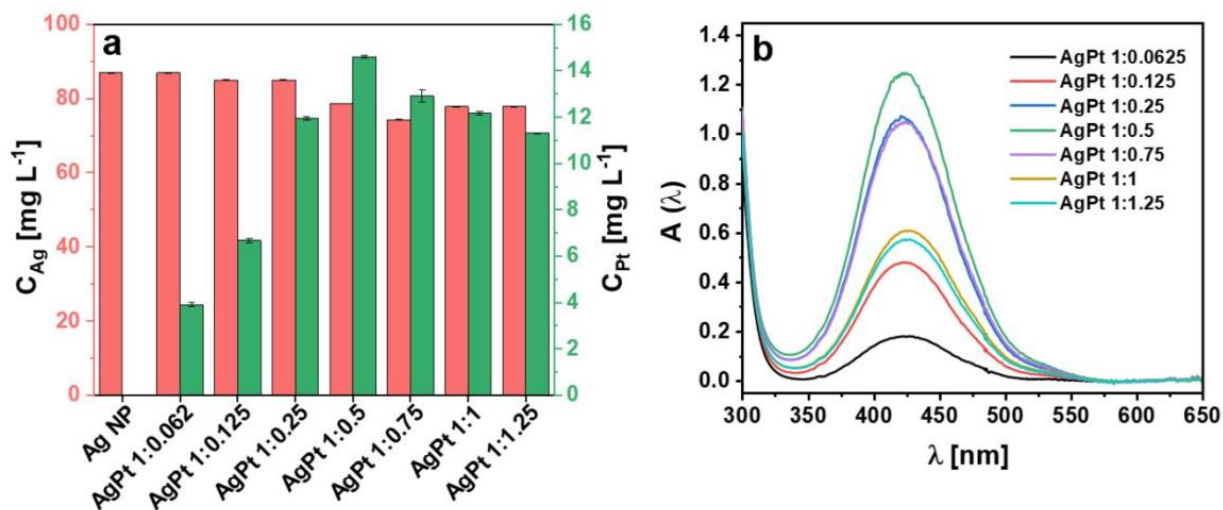


Figure 52. Intrinsic peroxidase-like activity of AgPt NPs as a function of their elemental composition. a) ICP-MS analysis of AgPt NPs obtained using different Ag:Pt molar ratios (C_{Ag} and C_{Pt} refer to the mass concentrations) and b) their corresponding peroxidase-like activity as shown from the UV-vis absorption spectra of the OPD oxidation product at pH 4. Prepublished in [206].

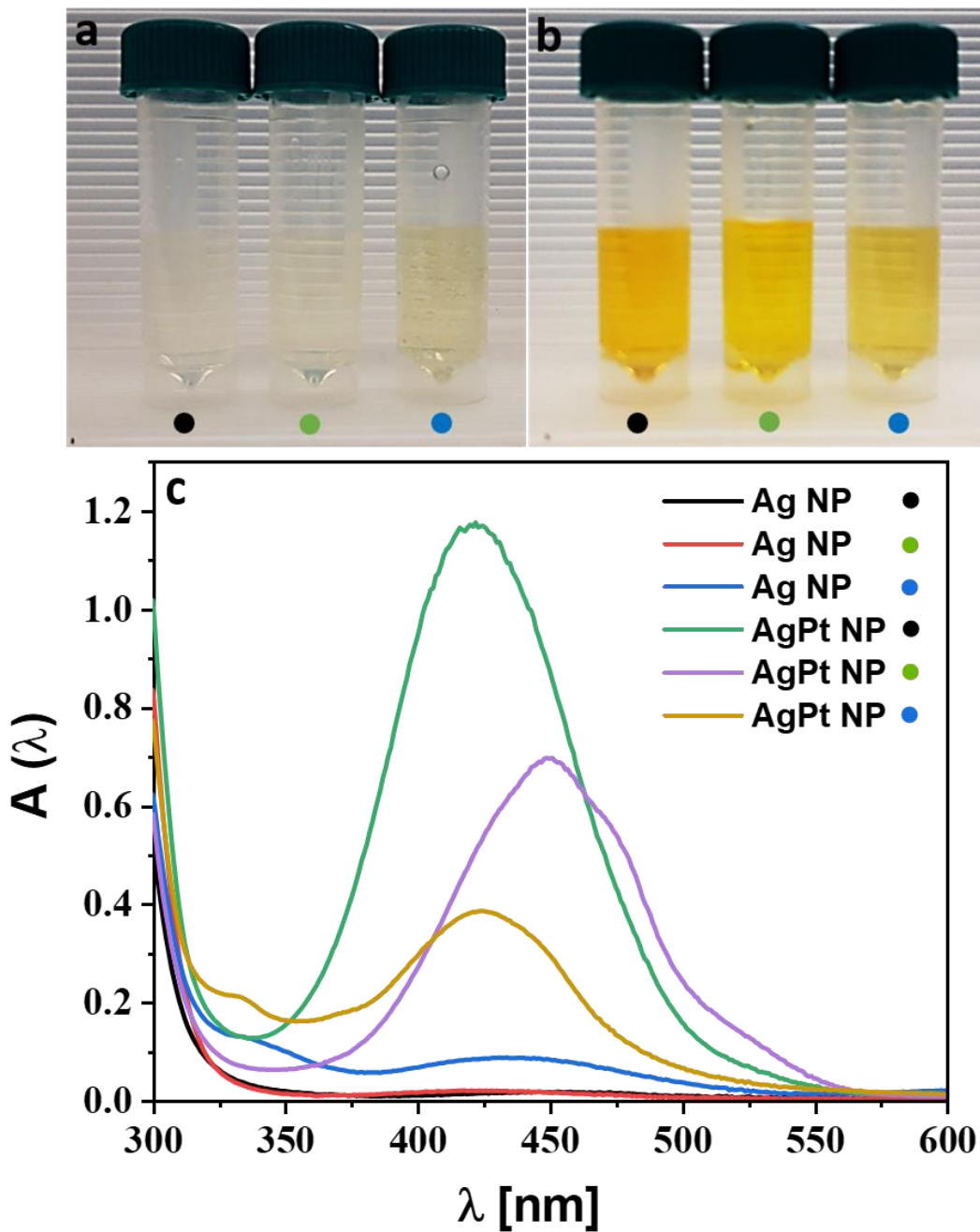


Figure 53. Peroxidase-like activity of Ag NP@SC and AgPt@SC NPs. Photographs of the peroxidase-like activity of a) Ag NP@SC and b) AgPt NPs@SC at different pH (pH 4: black circle, pH 7: green circle and pH 11: blue circle) and (c) their corresponding UV-vis absorption spectra. Prepublished in [206].

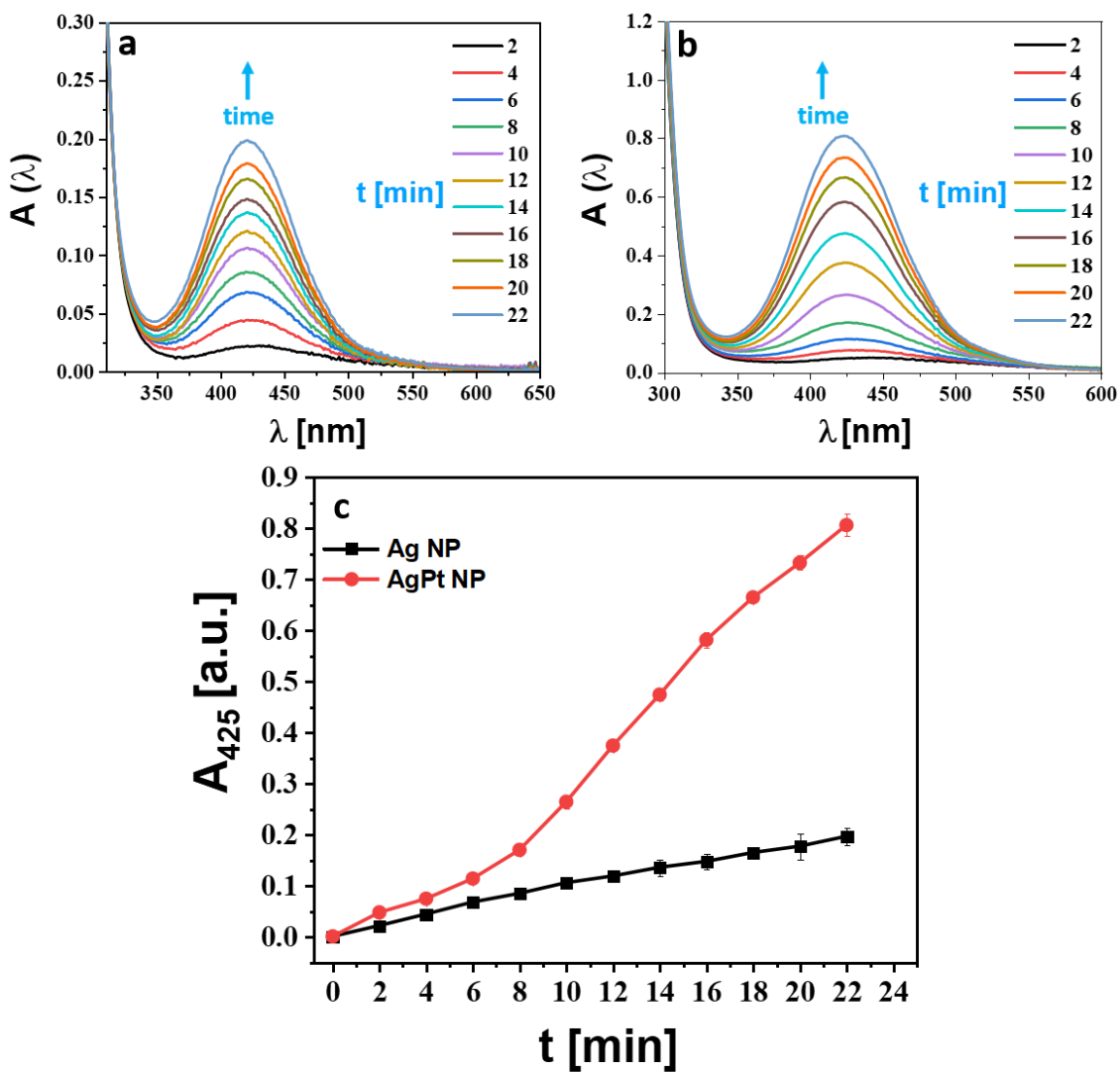
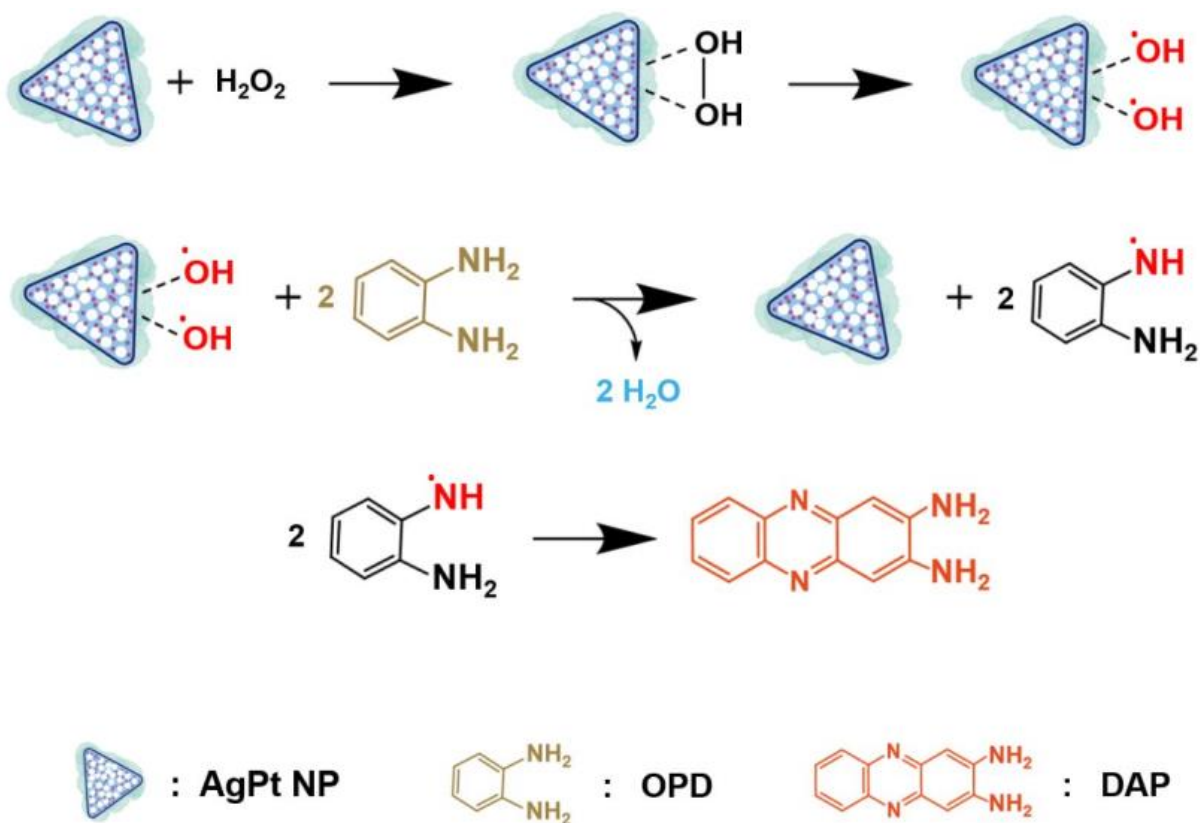


Figure 54. Kinetics of OPD oxidation using Ag NPs@SC and AgPt NPs@SC. Time-dependent absorbance spectra of the DAP generated upon oxidation of OPD in presence of a) Ag NPs@SC and b) AgPt NPs@SC at pH 4 and (c) their corresponding time-dependent absorbance changes at $\lambda = 425$ nm. Prepublished in [206].

The peroxidase-like activity exhibited by AgPt NPs follows most probably a radical chain mechanism, during which the hydroxyl radicals ($\cdot\text{OH}$) are generated after the catalytic base-like decomposition of H_2O_2 on the surfaces of AgPt NPs at acidic pH takes place (Eq. 2), a similar

H₂O₂ decomposition and [•]OH generation have been reported for a number of metals, metal oxides and metal ions.[217, 218] The accumulated [•]OH react with the OPD molecules adsorbed on the surfaces of the bimetallic NPs resulting in the formation of OPD radicals. Finally, the OPD radicals react with one another leading to the generation of the yellow-colored DAP (Scheme 1). It worth noting that in case of the absence of the peroxidase substrate, AgPt NPs catalytically decompose H₂O₂ in acidic media resulting in an accumulated production of the highly oxidative [•]OH (Eq. 2). Such intrinsic catalytic activity could be of significant importance for various biomedical applications, for instance, an accumulated production of the highly oxidative [•]OH in endosomes/lysosomes can elicit detrimental cytotoxic effects in tumor cells.



Scheme 1. Proposed mechanism of the peroxidase-like activity of AgPt NPs.. Prepublished in [206].

On the other hand, AgPt NPs show little to negligible peroxidase-like activity at neutral and alkaline pH ($\text{pH} \geq 7$), respectively (Figure 49 and Figure 50), this may be due to the lower concentration of $[\text{H}^+]$ which could not initiate the catalytic base-like decomposition of H_2O_2 (Eq. 2).

A set of experiments were carried out to determine the steady-state kinetics of the peroxidase-like activity of AgPt NPs. The catalytic rate of OPD oxidation by AgPt NPs at acidic pH as a function of substrate's -either H_2O_2 or OPD- concentration, were plotted and the curves follow typical Michaelis-Menten kinetics (Figures 49, 55 and 56).

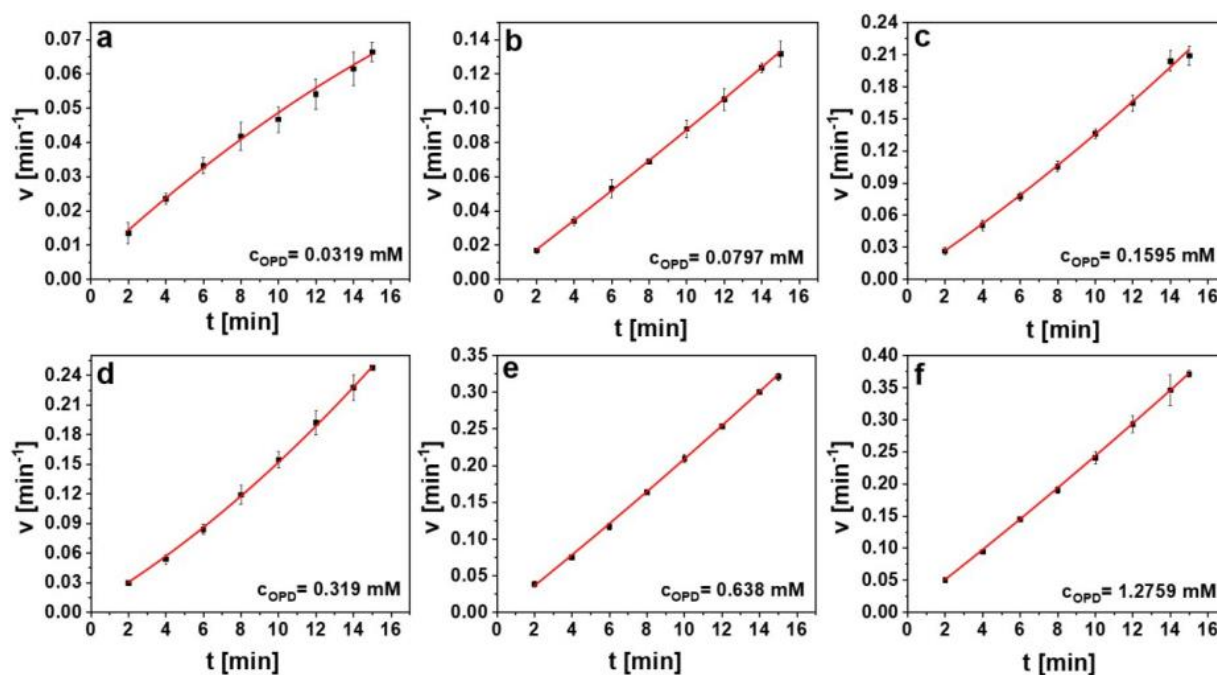


Figure 55. Apparent kinetics of AgPt NPs as peroxidase mimics using different concentrations of OPD. (a-f) Rate of the reaction (v)- time course (t) curves of OPD oxidation using different concentrations of OPD (C_{OPD}) while keeping the H_2O_2 concentration fixed. Prepublished in [206].

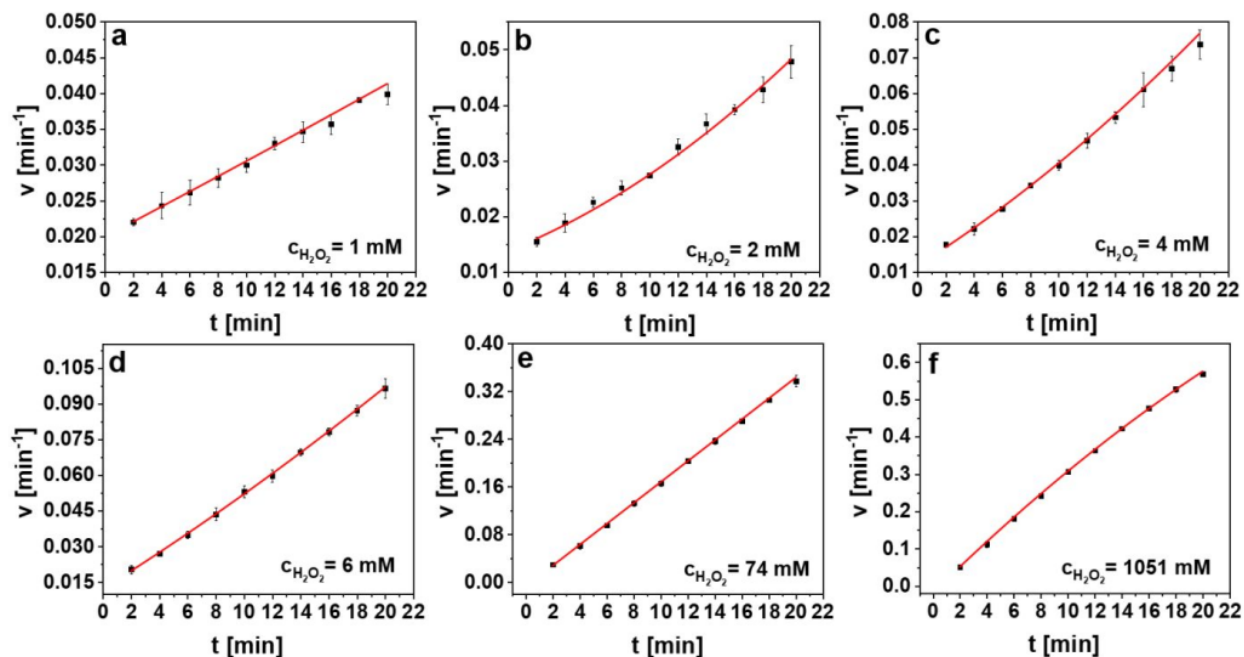


Figure 56. Apparent kinetics of AgPt NPs as peroxidase mimics using different concentrations of H_2O_2 . (a-f) Rate of the reaction (v)- time course (t) curves of OPD oxidation using different concentrations of H_2O_2 ($C_{H_2O_2}$) while keeping the OPD concentration fixed. Prepublished in [206].

The Michaelis–Menten kinetic parameters (Michaelis constant (K_m), maximum reaction velocity (V_{max}), were then extracted after fitting data fitting to the Michaelis–Menten equation and the turnover number (K_{cat}) was calculated ($K_{cat} = V_{max}/C_{cat}$), where C_{cat} is the concentration of AgPt NPs). The K_m value reflects the degree of affinity between the enzyme (AgPt NPs) and the substrate, V_{max} indicates the maximum catalytic activity when an enzyme is saturated with its substrate, and K_{cat} reflects the amount of DAP generated per a given concentration of AgPt NPs per unit time. The extracted kinetics parameters were then compared with those of the HRP enzyme (Table 1).

Table 1. Steady-State Kinetic Parameters of Peroxidase- and Catalase-Like Reactions Catalyzed by AgPt NPs. Prepublished in [206].

Type of enzyme catalysis	Catalyst	C _{Cat} [nM]	Substrate	K _m [mM]	V _{max} [$\mu\text{M s}^{-1}$]	K _{cat} [$\times 10^3 \text{ s}^{-1}$]	Ref.
Peroxidase-like activity	AgPt NPs	0.0332	OPD	0.129	0.0249	0.7510	Present study
		0.0332	H ₂ O ₂	76.05	0.0357	1.0751	[219]
	HRP	82.5	OPD	0.59	0.0465	0.0006	[219]
		82.5	H ₂ O ₂	0.34	0.0948	0.0011	[219]
Catalase-like activity	AgPt NPs	0.0332	H ₂ O ₂	62.98	6.1	183.735	Present study
	Catalase	0.266	H ₂ O ₂	54.30	16.2	60.902	[220]

With OPD as the substrate, the K_m value recorded in case of AgPt NPs is about 5 times lower than that recorded for HRP (0.129 mM in case of AgPt NPs and 0.59 mM for HRP) which suggests the stronger affinity of AgPt nanozyme for OPD compared to that expressed by HRP. Such higher affinity may be originating from the larger surface area of the nanozymes and the subsequent multiple accessible binding sites of AgPt NPs to the OPD compared to HRP, similar results have been reported for artificial nanozymes.[221] The higher K_m value obtained for H₂O₂ as the substrate in case of AgPt NPs (76 mM) suggests a higher concentration of H₂O₂ is needed for the AgPt NPs to express optimum peroxidase-like catalytic activity compared to HRP, this result is consistent with previous work on ferromagnetic nanozymes.[197] Moreover, the results revealed three orders of magnitude higher turnover numbers exhibited by the AgPt nanozymes compared to those showed by HRP, these results reflect the superior catalytic capability of AgPt nanozymes.

The ability of the bimetallic AgPt NPs to function as a nanozyme at neutral and alkaline pH conditions has been evaluated by studying the catalytic decomposition of H₂O₂ at such environments. The catalytic decomposition of H₂O₂ at pH 7.1 and 11 was accompanied by the formation of gas bubbles which is attributed to the liberation of molecular oxygen (O₂) (Figure 57), such catalytic behavior shown by AgPt NPs resembles the catalytic activity exhibited by natural catalase that catalyzes the decomposition of the oxidative H₂O₂ into O₂ into and water (H₂O). On the other hand, AgPt nanozymes did not exhibit a catalase-like activity at acidic pH (pH 4).

The artificial catalase activity of AgPt NPs is a composition-dependent and AgPt NPs synthesized using higher Ag:Pt molar ratio generally exhibit diminished catalytic activity (Figure 57f).

Our studies show that the bimetallic AgPt NPs exhibit greater catalase-like catalytic activity, when compared to the monometallic Pt NPs of equivalent Pt content (Figure 58). Hence, the catalytic activity of AgPt NPs could be tailored and optimized by tuning the Ag:Pt ratio, which brings some changes in the electronic structure of the resulted bimetallic system. Moreover, BSA-coated AgPt NPs showed greater catalase-like activity (Figure 57) in comparison to AgPt@SC NPs (Figure 59).

Increasing the levels of dissolved oxygen over time while incubating AgPt NPs with H_2O_2 in nearly neutral and alkaline pH indicate an acid-like decomposition of H_2O_2 , during which the highly oxidative H_2O_2 got adsorbed on the active sites of the nanozyme and subsequently interacts with the preadsorbed hydroxyl ions (OH^-). H_2O_2 passes a proton (H^+) to the OH^- resulting in the formation of OH_2 which interacts with another H_2O_2 yielding water and molecular oxygen trapped inside gas bubbles (Eq. 3–5).

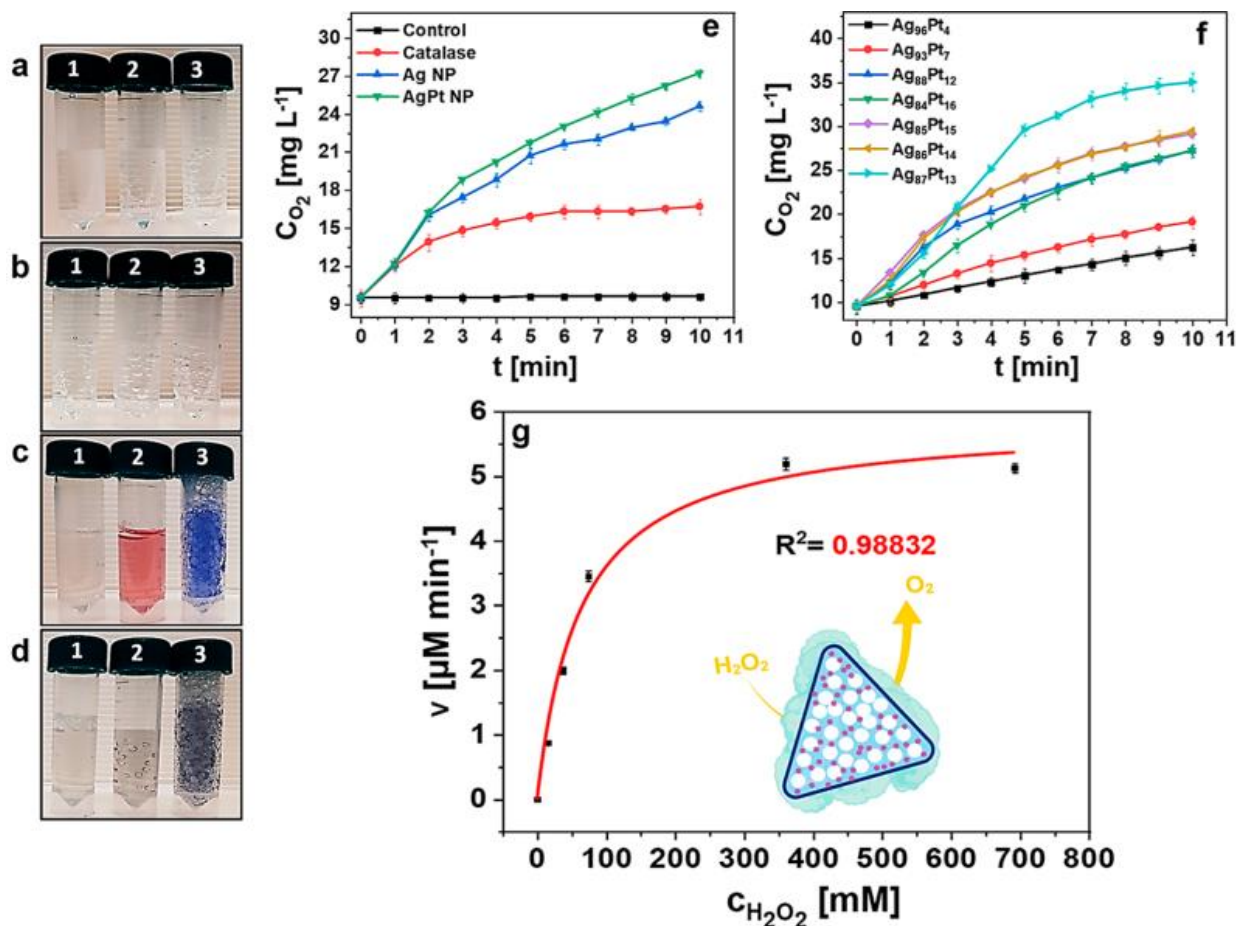


Figure 57. Catalase-like activity of AgPt NPs and steady-state kinetics of the catalytic reaction. (a–d) Photographs of the catalase-like activity of a) control, b) catalase, c) Ag NPs, and d) AgPt NPs at different pH (“1”, “2”, and “3” represent pH 4, pH 7, and pH 11, respectively) and e) their corresponding kinetics of catalytic activity at pH 11. f) Elemental composition-dependent catalase-like activity of AgPt NPs. g) Steady-state kinetics of the catalytic reaction where the rate of reaction (v) is plotted versus different concentrations of H_2O_2 ($C_{\text{H}_2\text{O}_2}$). The inset is the schematic illustration of the catalase-like activity of AgPt NPs. The error bars represent the standard deviation of three measurements. The (R^2) value represents the correlation coefficient. Prepublished in [206].

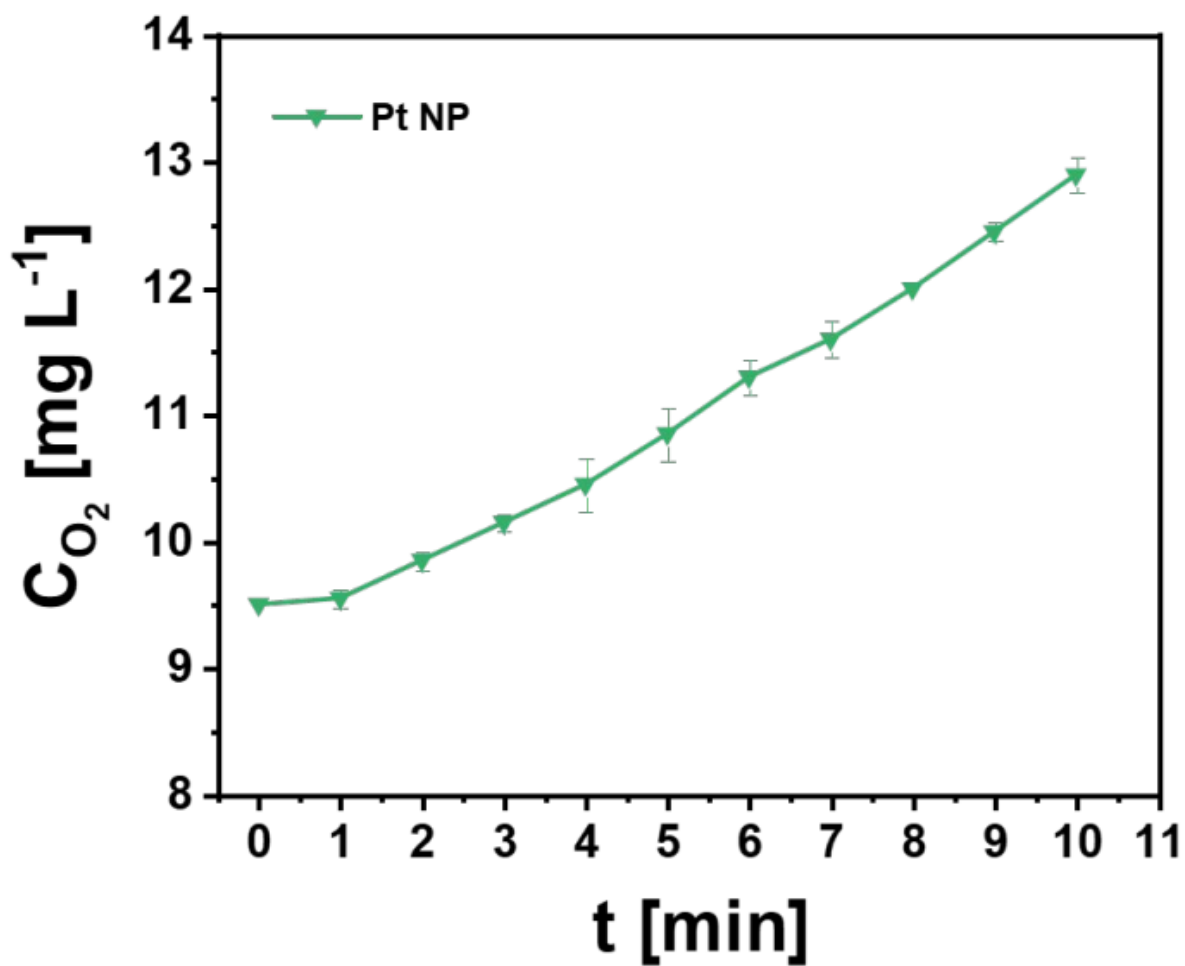


Figure 58. Catalase-like activity of Pt NPs@SC. Time-dependent changes in the concentration of liberated O₂ (C_{O₂}) during the catalytic decomposition of H₂O₂ in presence of Pt NPs@SC at pH 11. Prepublished in [206].

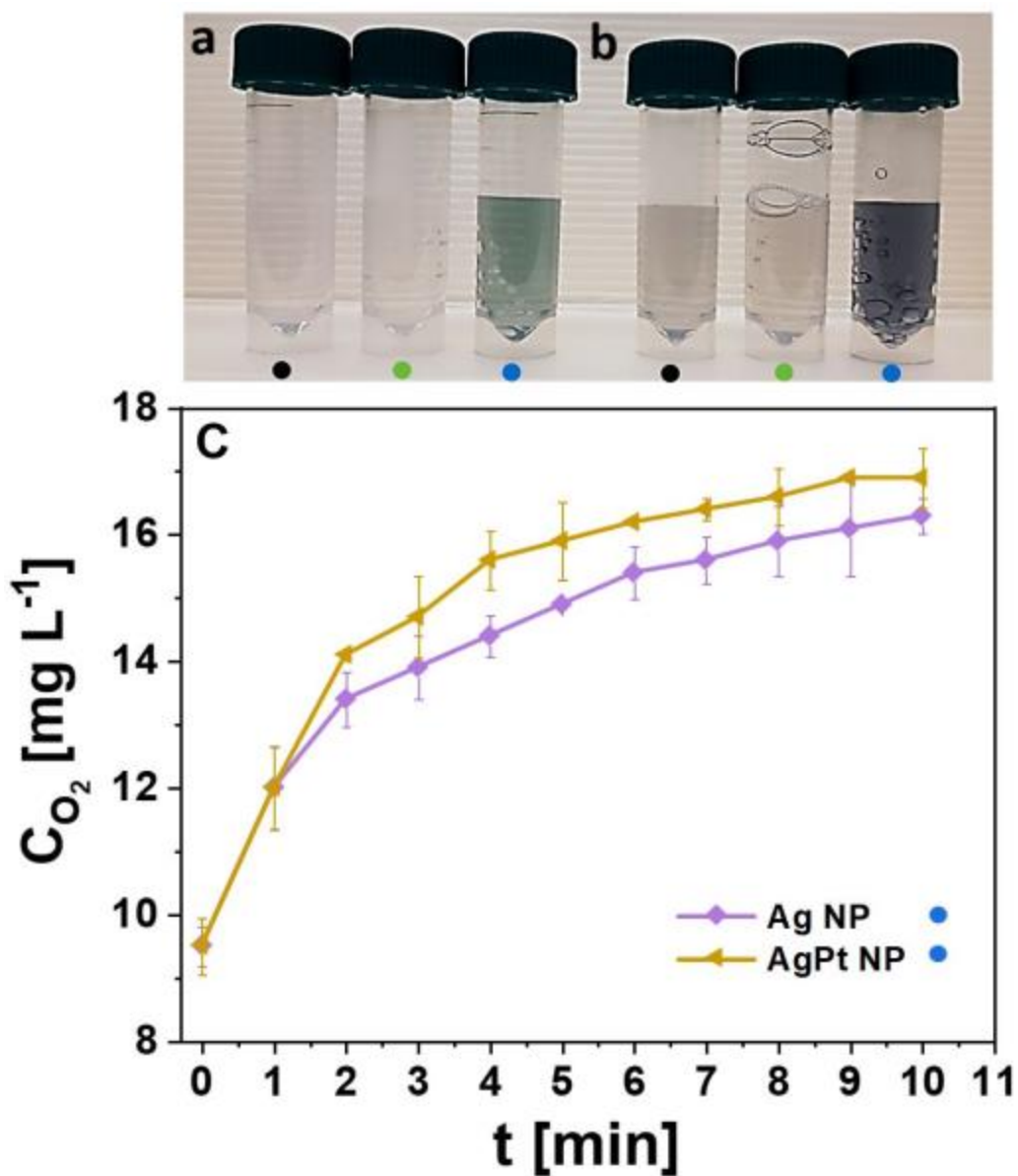


Figure 59. Catalase-like activity of Ag NPs@SC and AgPt NPs@SC. Photographs of catalase-like activity of a) Ag NPs and b) AgPt NPs at different pH (pH 4: black circle, pH 7: green circle and pH 11: blue circle). c) Time-dependent changes in the CO_2 during the catalytic decomposition of H_2O_2 in presence of Ag NPs and AgPt NPs at pH 11. Prepublished in [206].

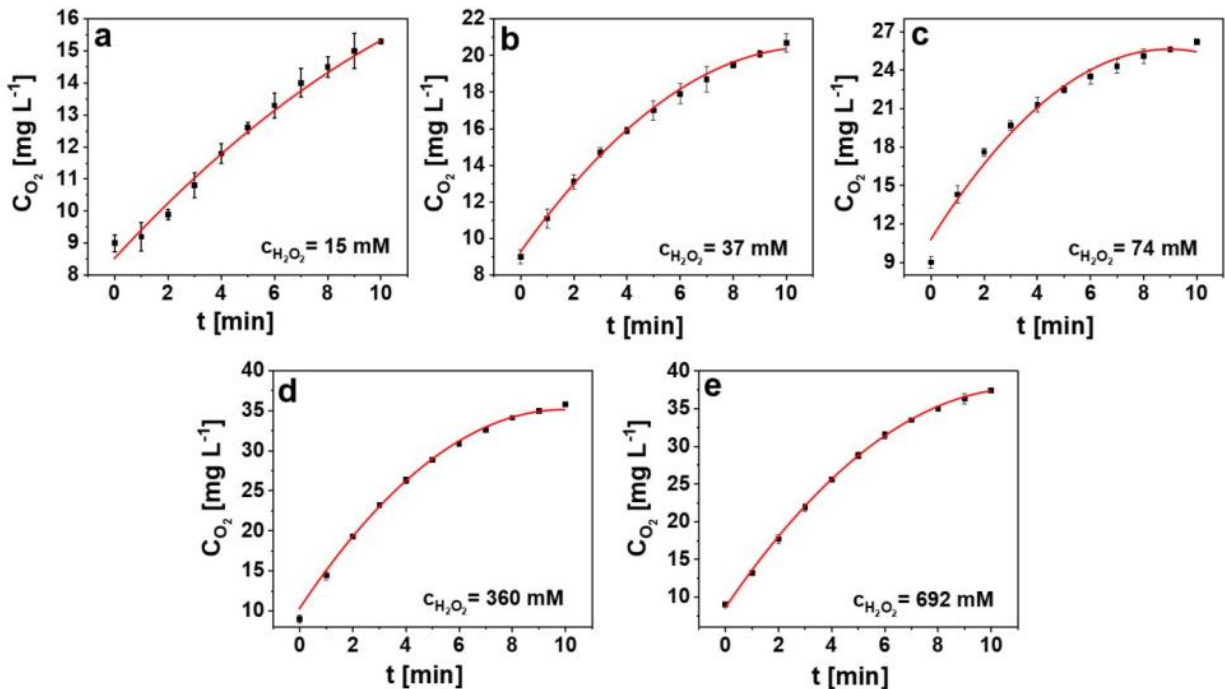


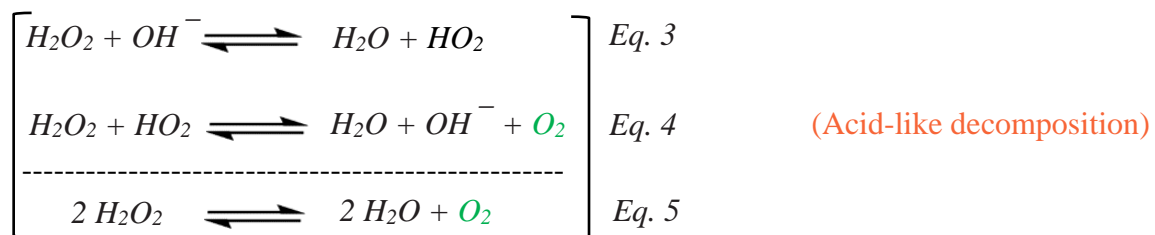
Figure 60. Apparent kinetics of AgPt NPs as catalase mimics. (a-e) concentration of liberated O_2 (C_{O_2})-time course (t) curves of H_2O_2 decomposition by AgPt NPs using different concentrations of H_2O_2 ($C_{H_2O_2}$). Prepublished in [206].

The rate of molecular oxygen liberation as a function of the H_2O_2 concentration was plotted and the data was fitted to Michaelis–Menten equation to evaluate the steady-state kinetics of the artificial catalase activity of AgPt nanozymes (Figure 60). The steady-state kinetic parameters were then determined thereof and compared to those of natural catalase (Table 1).

The K_m value recorded in case of AgPt nanozymes was 63.0 mM which is similar to the K_m value reported for catalase (54.3 mM) which suggests similar binding affinity AgPt nanozyme and catalase to H_2O_2 . However, the results revealed three times higher turnover numbers exhibited by the AgPt nanozymes ($K_{cat} = 1.84 \times 10^5 \text{ s}^{-1}$) compared to those showed by catalase ($K_{cat} = 6.1 \times 10^4 \text{ s}^{-1}$), these results reflect the superior catalytic capability of AgPt nanozymes.

Taken together, these results suggest that the pH-switchable H_2O_2 decomposition ability of AgPt nanozymes proceeds via two different catalytic routes; (1) at low pH, the peroxidase-like activity of AgPt NPs is activated and the H_2O_2 decomposition follows a base-like decomposition mechanism whereby an accumulated levels of $\cdot OH$ are formed (Eq. 2), and (2) at neutral and basic

pH, the artificial catalase activity of AgPt NPs is activated and an acid-like decomposition of H₂O₂ takes place resulting in the liberation of O₂ gas bubbles (Eq. 3-5).



This fascinating dual nanozymatic activity exhibited by AgPt NPs at different pH media could be an interesting property in various biomedical applications, for instance AgPt nanozymes could elicit oxidative damage (as a result of accumulated $\cdot OH$ levels) in acidic environments such as cancerous cells, while acting as antioxidants via reducing H₂O₂ levels attributed to their catalase-like activity at neutral pH compartments such as healthy cells (Figure 61).

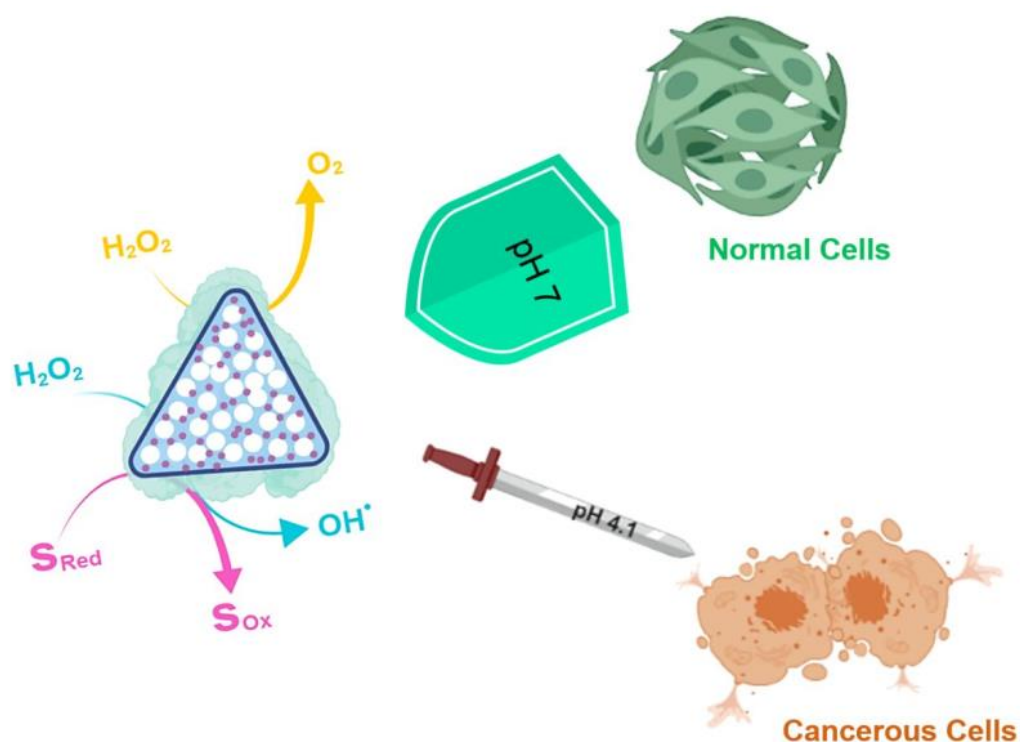


Figure 61. pH-switchable catalytic activity and the selectivity of AgPt NPs in different pH environments. Prepublished in [206].

3.2.4 Cargo-loading capacity of porous AgPt NPs

The porous nature and biocompatible surface ligand of AgPt NPs could offer an effective drug loading platform, whereas, their ability to decompose H_2O_2 may account for controlled drug release behavior.

The drug loading and release behavior of the porous AgPt nanozymes was evaluated using the highly fluorescent calcein as a model cargo. Using the same amount of NPs, the porous nature of AgPt nanozymes allowed them to entrap three times more calcein than entrapped by the solid structures of Ag NPs ($\sim 60 \mu\text{M}$ vs. $\sim 20 \mu\text{M}$) (Figure 62b and Figure 64).

The loading content (LC) and loading efficiency (LE (%)) are two important parameters used to evaluate the loading efficiency of drug carrier. The results show a significant increase in calcein loading content into the porous AgPt NPs by increasing the amount of added calcein to the NPs, for instance, about 5 times increase in the LC is observed when a small amount of NPs (0.1 mg) incubated with 1.3 mg of calcein compared to when the same amount of NPs incubated with 0.4 mg of the model dye (Figure 62c and Figure 65). On the other hand, a decrease in the LE of calcein into the AgPt NPs is observed by increasing the amount of added calcein, for instance the loading efficiency of calcein decreases from 65% to about 15% when the added calcein increases from 0.01 mg to 1.3 mg.

The affinity of AgPt NPs to the H_2O_2 as well as the strong etching ability of H_2O_2 to the Ag NPs facilitate the controlled release of the loaded calcein dye. The stimulated calcein-release from Ag NPs and the porous AgPt NPs upon H_2O_2 stimulus was investigated and the results showed about 28 and 16 fold increase in the fluorescence intensity of calcein-loaded AgPt and Ag NPs, respectively, after being reacted with H_2O_2 (Figures 62d and 62e). The larger surface area of the porous structure which offers higher calcein loading capacity accounts for this two-fold increase in the fluorescence intensity of calcein-loaded AgPt NPs compared to Ag counterparts. The triggered calcein release from AgPt NPs is mainly driven by two parallel pathways; 1) high affinity of AgPt NPs to H_2O_2 , their peroxidase-like activity and ability to decompose H_2O_2 , and 2) the strong etching ability of the highly oxidative H_2O_2 and their ability to elicit the oxidative dissolution of the Ag scaffold of AgPt NPs and the subsequent gradual disruption of the NPs followed by the release of calcein dye. These two pathways are parallel and control the release kinetics of calcein from the NPs (Figure 62a and Figure 66). It worth noting that the release kinetics

of calcein from AgPt NPs is much slower than that from Ag NPs, this effect results from the higher chemical stability of the bimetallic AgPt NPs compared with the monometallic Ag NPs, that means that the oxidative dissolution rate of AgPt NPs is lower than that of Ag NPs, as mentioned earlier.[182] Such cargo release mechanism could form the basis of smart drug carrier with sustainable cargo release behavior. The synergistic release of the cytotoxic Ag^+ ions, highly oxidative $\cdot\text{OH}$, as well as the cargo-loading efficiency and the triggered and sustainable release of the cargo make the AgPt NPs potential cancer treatment modality.

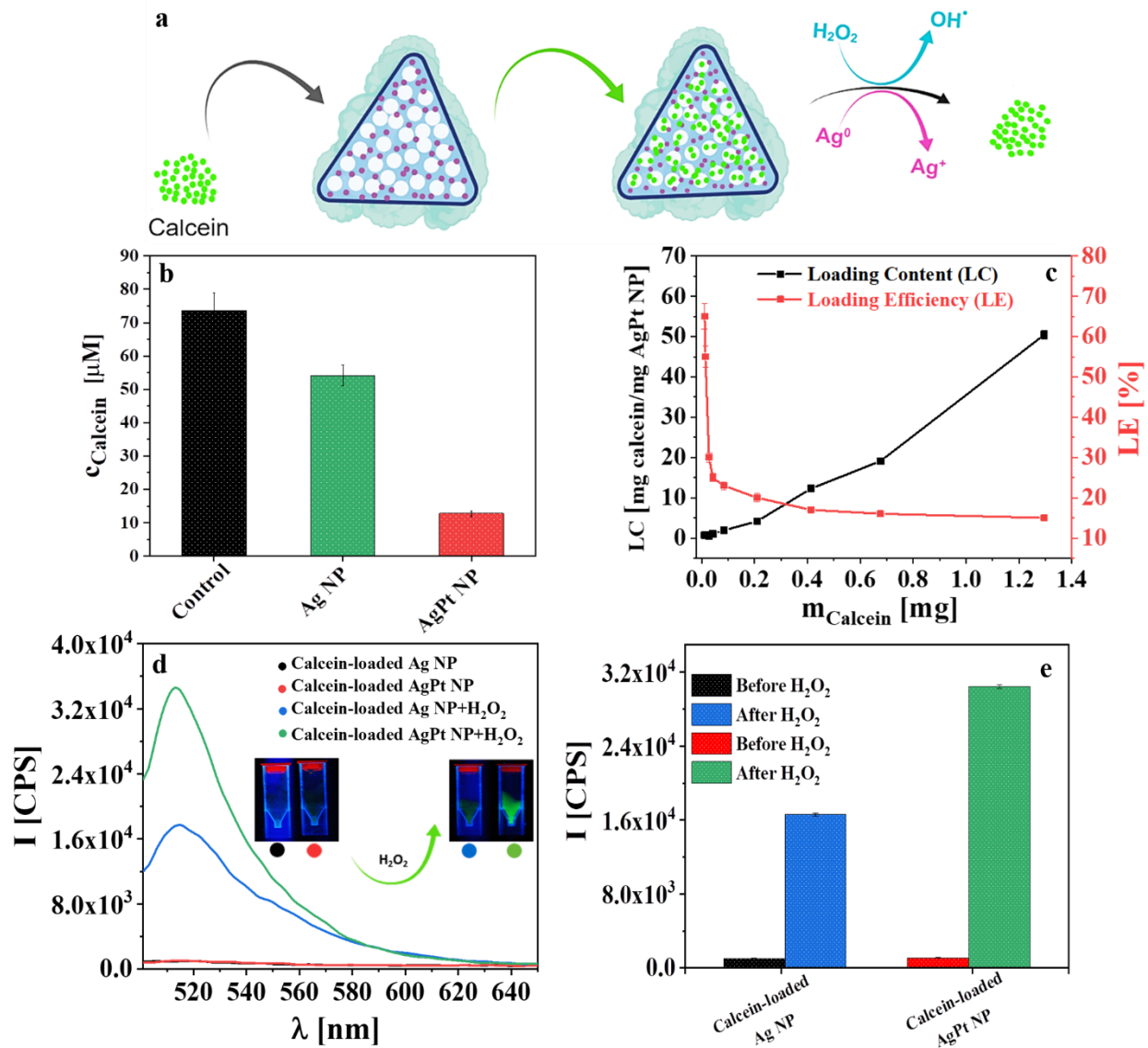


Figure 62. Cargo loading into porous AgPt NPs and their oxidative stress-triggered release. a) Schematic illustration of calcein-loading into AgPt NPs and its controlled release upon the addition of H₂O₂ stimulus. b) Quantitative assessment of calcein in the supernatants after reaction of Ag NPs and AgPt NPs with calcein using a calibration curve (see Figure 63). c) LC and LE values of Calcein loading into the AgPt NPs after reacting the AgPt NPs with different concentrations of calcein (Figure 65). d) Controlled release of calcein upon the addition of H₂O₂. The inset show photographs of the H₂O₂-triggered calcein release from the NPs. e) Column representation of the fluorescence intensities in (d) before and after triggered calcein release. Prepublished in [206].

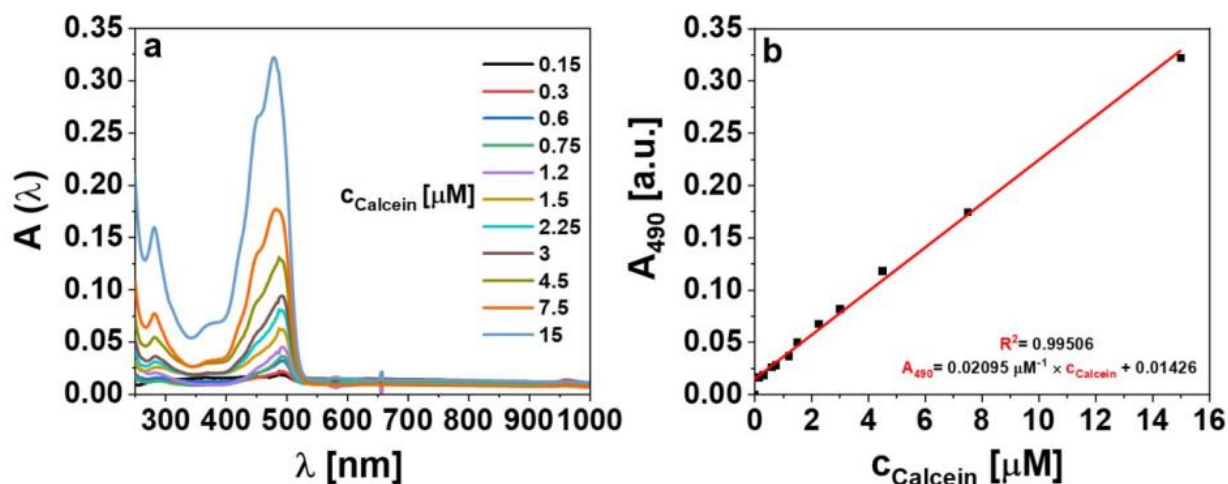


Figure 63. Calcein standard curve. (a) UV-vis absorption spectra of different calcein concentrations and b) calibration curve of calcein plotted by measuring the absorbance of different calcein concentrations in (a) at $\lambda = 490$ nm. The (R^2) value represents the correlation coefficient. Prepublished in [206].

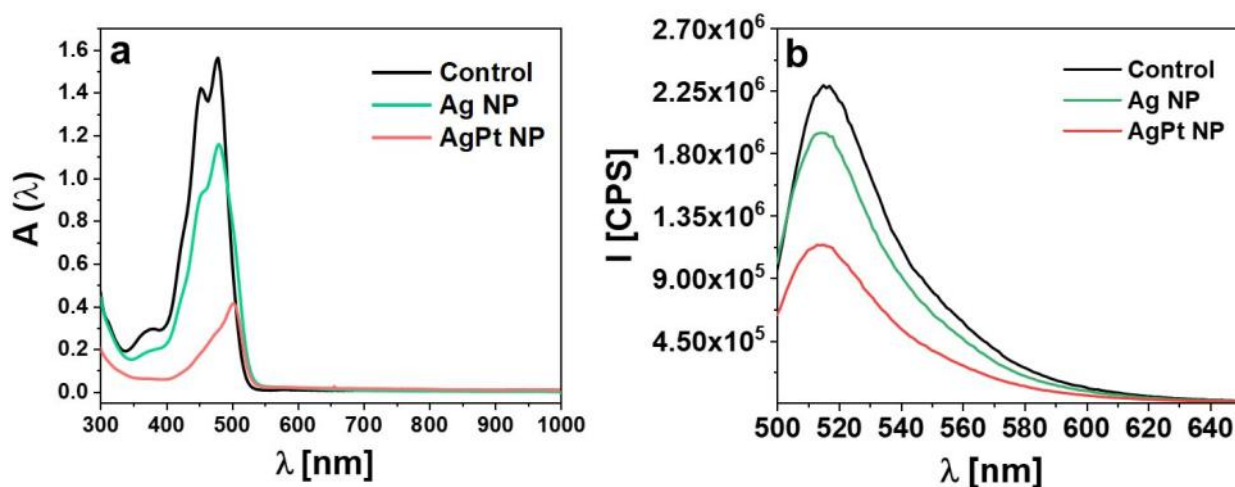


Figure 64. Calcein loading efficiency of NPs. a) UV-vis absorption spectra and b) emission spectra of the supernatants after reaction of Ag NPs and AgPt NPs with calcein, respectively, relative to control calcein solution. Prepublished in [206].

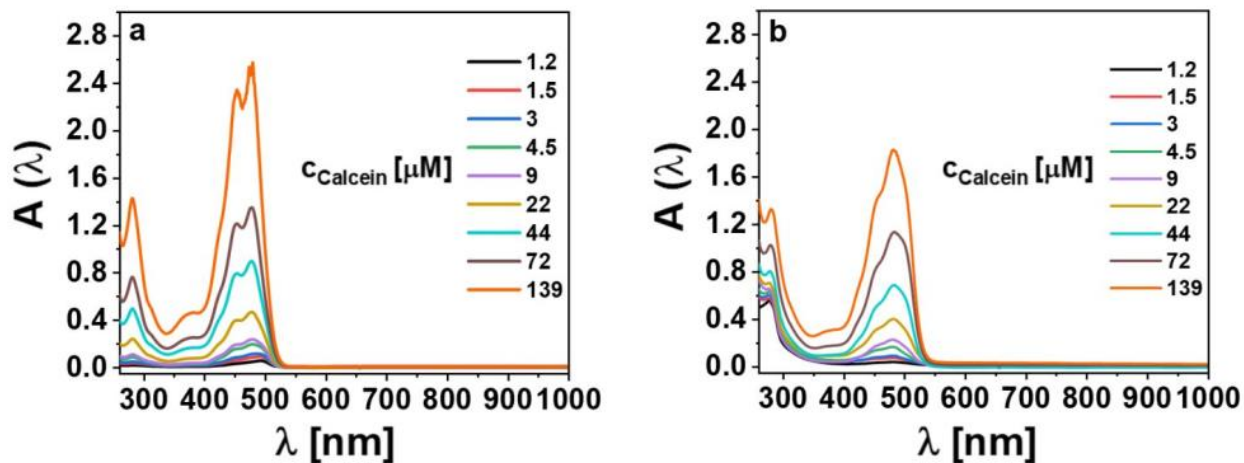


Figure 65. UV-vis absorption spectra of different calcein concentrations a) before and b) after reacting with AgPt NPs. Prepublished in [206].

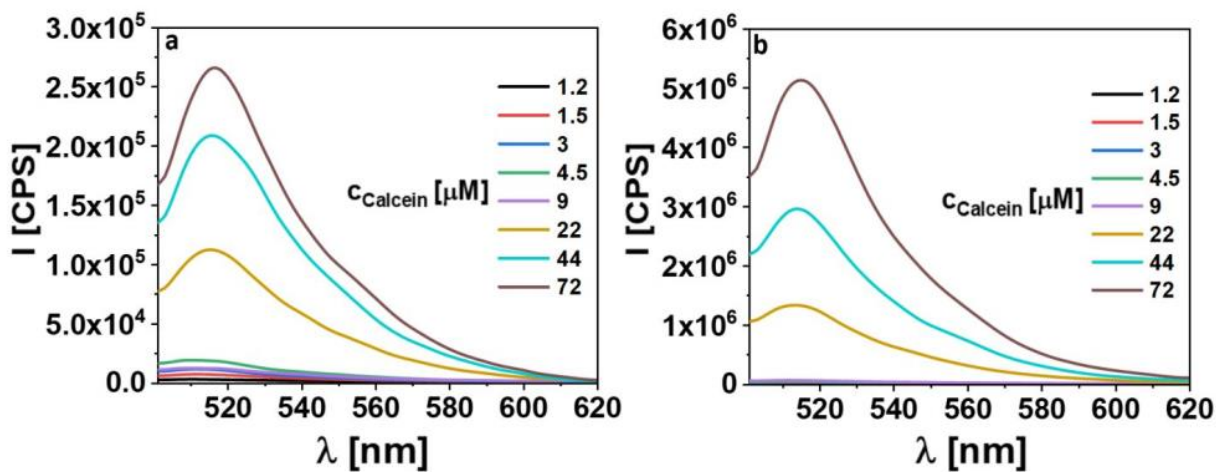


Figure 66. Controlled release of calcein after loading AgPt NPs with different concentrations of calcein. (a and b) Emission spectra of calcein before and after the addition of H_2O_2 stimulus to the calcein-loaded AgPt NPs, respectively. Prepublished in [206].

4. Conclusion and Outlook

This work showed the use of benign and biocompatible surface ligands in such a way they serve either as: i) surface capping agents in order to direct the growth of different anisotropic NPs, for instance we have used the BSA protein for the synthesis of popcorn-shaped Au NPs as well as prism-shaped bimetallic NPs, or as ii) surface passivating agent to passivate the surface of an already synthesized anisotropic NPs, for eg. the surfaces of CTAB-coated GNRs were passivated with biocompatible silica layer. In either way the resultant nanoparticles retain their physicochemical properties and gain new properties in addition to their biocompatible nature.

In the current work a plasmophore composed of GNC-functionalized silica-overcoated GNRs (GNR@SiO₂@GNC) showed enhanced colloidal, thermal and photothermal stability while retaining the original optical properties of GNRs and the fluorescence behavior of GNCs. Passivating the cationic CTAB layer of GNRs with a biocompatible SiO₂ shells reduces the cytotoxicity of pristine GNRs. Moreover, the photothermal as well as the fluorescence behavior of GNR composites could be tuned by adjusting the silica shell thickness. The nanocomposites hold a great promise for diverse applications such as multimodal imaging, PTT and the high surface area of silica coating facilitates efficient drug loading capability.

The current work also reports the efficient, facile, and sustainable synthesis route of colloiddally stable anisotropic GNPCs using BSA protein. The synthetic route is scalable and liters of GNPCs could be synthesized in a single batch. The BSA-capped GNPCs have shown to be non-cytotoxic to HeLa cells and MRC-5 cells, while, a similar size CTAB-coated GNPCs elicited apparent cytotoxicity in the same cells.

Moreover, this work pointed out the use of BSA to direct the shape of the grown nanoparticles. In the third chapter, BSA protein biotemplate was used for the synthesis of biocompatible porous AgPt bimetallic NPs. The porous AgPt NPs exhibit pH-switchable peroxidase-/catalase-mimetic activity which could be easily tuned by adjusting their elemental composition. This fascinating dual nanozymatic activity exhibited by AgPt NPs at different pH media could be an interesting property in various biomedical applications, for instance AgPt nanozymes could elicit oxidative damage (as a result of accumulated $\cdot\text{OH}$ levels) in acidic environments such as cancerous cells, while acting as antioxidants via reducing H₂O₂ levels attributed to their catalase-like activity at neutral pH compartments such as healthy cells. In addition, the porous nature, biocompatible

surface ligand of AgPt NPs as well as their profound cargo-loading capacity could offer an effective drug loading platform, whereas, triggered cargo release driven by H_2O_2 etching stimulus of their Ag backbone may account for controlled drug release behavior.

With the basic enhancement of the physicochemical properties as well as the biocompatibility demonstrated, further work needed to be done firstly to implement such interesting nanostructures to various in vitro studies to evaluate their efficacy. The easily functionalizable-surfaces of the nanostructures described in this work thanks to their BSA and silica coating, allow for equipping them with wide variety of targeting moieties, imaging and therapeutic agents which make them a great choice in many biomedical applications. Of great importance, the unprecedented enzyme-mimicking activity of the bimetallic AgPt lies in the oxidoreductases family (peroxidase and catalase are two examples), future work to explore the possibility of using such NPs in other enzymatic category such as hydrolases or lyases would contribute a lot to the current research. In addition, the high loading capacity of their porous structure and their cargo release response upon reacting with specific stimulus could also be of paramount importance to the field of drug nanocarriers. Furthermore, the interesting results exhibited by the $\text{GNRs@SiO}_2\text{@GNCs}$ plasmophores could pave the way for future work to explore the using of such plasmonic antennas to control the fluorescence behavior of many fluorophores by simply tuning the distance at which the fluorophores is located from the plasmonic surfaces and holds therefore great promise for super-resolution bioimaging. The interesting photothermal behavior of the $\text{GNRs@SiO}_2\text{@GNCs}$ should be further explained for other AR of GNRs and with various laser wavelengths. Besides the great biocompatibility exhibited by the gold nanopopcorn, future work on tuning its plasmonic peak to reach NIR and testing their photodynamic and photothermal activity. The multiple hot spots formed around and between the tips of such BSA-coated gold nanopopcorn should also be tested in many SERS application especially for immunoassays.

5. Appendix

5.1 Materials

Before use, all glassware was appropriately washed with aqua regia (3:1 (v/v) conc. HCl/conc. HNO₃) followed by rinsing with copious amounts of Milli-Q water. Chloroauric acid (HAuCl₄) was purchased from Alfa Aesar, sodium citrate, L-Glutathione (GSH), silver nitrate (AgNO₃), ascorbic acid (AA), sodium borohydride (NaBH₄), hexadecyltrimethylammonium bromide (CTAB), hydrochloric acid (HCl), Methanol (MeOH), tetraethyl orthosilicate (TEOS), N-hydroxysuccinimide (NSH), 1-Ethyl-3-(3-dimethylaminopropyl)carbodiimide (EDC), polyvinylpyrrolidone (PVP), bovine serum albumin (BSA), chloroplatinic acid hexahydrate (H₂PtCl₆·6H₂O), palladium chloride (PdCl₂, 99%), L-glutamine, L-arginine, L-lysine, lysozyme from chicken egg white (Lys), L-methionine, catalase (Cat), pepsin of porcine gastric mucosa (Pep), L-phenylalanine, L-histidine, L-isoleucine, L-valine, beta-lactoglobulin from bovine milk (Blg), hemoglobin (Hem), L-tryptophan, myoglobin (Mb), L-alanine, human serum albumin (HSA), casein from bovine milk (Cas), L-leucine, L-asparagine, L-aspartic acid, L-proline, L-serine, L-threonine, L-tyrosine, ortho-phenylenediamine (OPD, 98%), peroxidase from horseradish (HRP) (150 U/mg), and calcein were purchased from Sigma-Aldrich, (3-Aminopropyl)triethoxysilane (APTES) was purchased from Fluka, 4-(2-hydroxyethyl)-1-piperazineethanesulfonic acid (HEPES) was purchased from Biochrom, sodium oleate (NaOL) was purchased from TCI, glycine, glutamic, Sodium chloride (NaCl, 99.9%) and hydrogen peroxide (30% in H₂O acid sodium hydroxide (NaOH) were purchased from Roth. Phosphate-buffered saline (PBS), Dulbecco's Modified Eagle Medium (DMEM), Roswell Park Memorial Institute culture medium (RPMI), and fetal bovine serum (FBS) were purchased from ThermoFischer.

5.2 Characterization of NPs

The successful synthesis of different NPs used in this work and their functionalization was confirmed using different spectroscopic measurements. The UV-vis absorption spectra as well as fluorescence spectra were recorded with an Agilent 8453 UV-vis spectrophotometer and a Fluorolog fluorescence spectrophotometer equipped with a 450 W Xe-lamp (FL3-22, Horiba Jobin Yvon Inc.), respectively, using 10 mm path length quartz cuvettes. The hydrodynamic diameters and zeta potential measurements of NPs was carried out using a Malvern Zetasizer Nanoparticle

analyzer (ZEN 3600) instrument. The morphology of different NPs mentioned in this work was analyzed using JEOL JEM-2100F-UHR field emission gun transmission electron microscope (TEM) (JEOL, Japan), equipped with high angle annular dark field (HAADF) and HRTEM images were recorded with TVIPS F216 CMOS camera (2k x 2k). Scanning transmission electron microscopy (STEM) studies were performed in STEM mode. The TEM was operated at an accelerating voltage of 200 kV. Elemental distribution within the NPs was recorded through energy-dispersive X-ray spectroscopy (EDS) spot analysis using a Philips CM 300 UT (LaB6) TEM operating at 200 kV, supplied with SDD EDX detector (Ametek) and Gatan CCD camera. All samples were drop-casted on ultrathin carbon-coated copper grids (300-400 mesh square) and left to dry in a Petri dish before imaging.

For GNRs work, In order to gain more insights into the spatial distribution and assembly of GSH-coated GNCs on the GNRs@SiO₂ surfaces, STEM tomography reconstruction (3D TEM) was carried out by retrieving the 3D structure of the NPs through acquiring TEM images over a tilt of $\pm 74^\circ$, then the acquired images were aligned and processed in respect to each other which results ultimately in the 3D reconstruction of the NPs morphology.

For AgPt work, X-ray photoelectron spectroscopy (XPS) measurements were performed using a high-resolution two-dimensional delay line 230 detector. [222] A monochromatic X-ray source (photon energy 1486.6 eV; anode operating at 15 kV) was used. The XPS spectra were recorded in fixed transmission mode with pass energy of 20 eV and 40 eV chosen for the region and survey, respectively. The binding energies were calibrated based on the graphitic carbon 1s peak at 285 eV and the charging effects were compensated by using a flood gun. The base pressure was around 2×10^{-10} bar. The NPs were concentrated, drop-casted on a copper film, dried and then inserted in the instrument for the measurement. Casa XPS software was used to analyze and deconvolute all XPS spectra.

To reveal the role of BSA in directing the shape of the synthesized GNPCs, Ag nanoprism and AgPt NPs and to obtain insights into the evolution of secondary structure elements of BSA during the synthesis of the NPs, the conformational modifications, folding and binding properties of BSA molecules were evaluated using circular dichroism (CD). Circular dichroism measurements were carried out on a ChiralScan™ Circular Dichroism Spectrometer (Applied Photophysics Ltd., UK). CD spectra of different controls and NPs were recorded at 25 °C from 190 to 260 nm with a

bandwidth of 1 nm and a 2 mm path length quartz cuvettes was used. The CD spectra were recorded, averaged over three scans and the data were then introduced to a freely available web server “<http://bestsel.elte.hu>” that uses the Beta Structure Selection method (BeStSel), which implements an algorithm used for the secondary structure determination and fold recognition of a protein and takes into consideration the twist of β -structures. This method can effectively estimate the secondary structure for a broad range of proteins.[169, 223]

To further investigate the structural changes of BSA during the synthesis of GNPCs, Ag NPs and AgPt NPs, fluorescence experiments were carried out. The intrinsic fluorescence behavior of BSA originates from two tryptophan residues (Trp-134 in domain I and Trp-213 in domain II). It had been shown that the fluorescence intensity and the emission maxima depend on the degree of exposure of the Trp-side chains to polar solvents[224, 225] as well as the properties of the environment around the Trp residues,[226] respectively. The conformational alternation of BSA during the synthesis of Ag NPs could be probed by the selective excitation of Trp-residues at 295 nm.[166]

5.3 Experimental Design

5.3.1 Surface passivation of CTAB-coated GNRs using biocompatible silica shell and fluorescent GNCs

5.3.1.1 Synthesis of GNRs@CTAB

GNRs of different aspect ratios have been synthesized using the previously reported seed-mediated route[83] with minor modifications. In brief, the seed solution was synthesized by mixing 5 mL of HAuCl₄ solution (0.5 mM) with 5 mL of CTAB solution (200 mM) for 5 minutes. Then 1 mL of freshly prepared NaBH₄ solution (6 mM) was injected to the reaction mixture under vigorous stirring. The color changes immediately into brownish yellow. After 2 minutes of stirring, the solution was then removed and the seed solution was left to age for 30 min at room temperature before further use. Then the growth of GNRs was performed using a mixture of binary surfactants (CTAB and sodium oleate (NaOL)). In the growth step, 7 g of CTAB solution and 1.234 g of NaOL were completely dissolved in 250 mL of warm MQ water. The solution was then cooled down to 30° C and different volumes of AgNO₃ (4 mM) were added in order to grow GNRs of different AR. After 15 min, 250 mL of HAuCl₄ solution (1 mM) was injected to the reaction mixture under moderate stirring for 90 min. then the pH of the growth solution was adjusted using

different volumes of HCl (12.1 M) to obtain the desired AR. After 15 min of slow stirring, 1.25 mL of 64 mM ascorbic acid was injected under vigorous stirring for 30 seconds. Afterwards, different amounts of seed solution was added under vigorous stirring for another 30 seconds to obtain the desired AR. The GNRs of desired AR were then obtained after leaving the reaction mixture undisturbed at 30° C for 12 h. The purification of GNRs was then performed in order to remove excess CTAB and other unreacted impurities. Of particular importance, the CTAB concentration in the as-prepared GNR solutions should be adjusted for the subsequent silanization of GNRs.

To do that, the as-synthesized GNR solution was divided into equal volumes (~50 mL) in 50 mL falcon tubes and was subsequently washed by two consecutive cycles of centrifugation at 8000 rpm for 20-30 min. The resultant pellets were resuspended in 5 mL of MQ water and pooled together so that to bring the total volume of GNR solution into 50 mL with a final CTAB concentration of about 15 mM (initial concentration of CTAB in the as-synthesized GNR solution is 37 mM).

The concentration of GNRs was then determined based on their absorption values at LSPR maxima via the Beer-Lambert law using previously reported molar extinction coefficients (ϵ) values of GNRs of different aspect ratios.[227]

5.3.1.2 Synthesis of fluorescent GSH-capped GNCs

The GSH-capped GNCs were synthesized according to a previously reported method[228] with a slight modification. In brief, 10 mL of freshly prepared aqueous solution of HAuCl₄ (20 mM) and 3 mL of GSH (100 mM) were mixed with 87 mL of MQ water under moderate stirring. The reaction mixture was subsequently heated to 70°C under reflux for 24 h. The appearance of a yellow colored solution with orange fluorescence indicates the successful synthesis of GSH-capped GNCs. The resultant GNCs were purified by ultrafiltration (MWCO= 3 kDa) and suspended in MQ water for further experiments.

5.3.1.3 Synthesis of GNRs@GNCs and GNRs@LBL@GNCs

Two methods, namely, direct electrostatic interaction and the layer-by-layer (LBL) technique have been firstly checked for their applicability to functionalize the GNRs with GNCs. The former

technique was performed by incubating 1 mL of the positively charged GNRs@CTAB (1nM) with 1 mL of the as-synthesized negatively charged GSH-capped GNCs under moderate stirring for 2 h. The resultant solution was then purified by 2 cycles of centrifugation and the pellet was then redispersed in MQ water. The LBL process was carried out by overcoating GNRs@CTAB with consecutive layers of differently charged polyelectrolytes as previously described[59] with slight modification. In brief, 1 mL of the as-synthesized GNRs were transferred into centrifuge vials and centrifuged at 8000 rpm for 20 min. The pellets were then resuspended in 1 mL of NaCl (1 mM) and 200 μ L of the negatively charged PSS polyelectrolyte (10 mg/mL in 1mM NaCl) and vials were immediately sonicated for 30 min. The excess polyelectrolyte was removed by centrifugation at 8000 rpm for 20 min. The pellets were then resuspended in 1 mL of NaCl (1 mM) and 200 μ L of the positively charged PDADMAC polyelectrolyte (10 mg/mL in 1mM NaCl) and sonicated for 30 min. The GNRs can be coated by multiple polyelectrolyte layers of opposite charges in the same manner. The GNR were purified at the end of the coating process by two cycles of centrifugation at 8000 rpm for 20 min and the pellets were resuspended in MQ water. The conjugation of GNCs to the PDADMAC-coated GNRs was carried out by adding 1 mL of PDADMAC-coated GNRs with 1 mL of the as-synthesized negatively charged GNCs under moderate stirring for 2 h. The resultant solution was then purified by 2 cycles of centrifugation and the pellet was then redispersed in MQ water.

5.3.1.4 Silanization of GNRs@CTAB

The silanization of GNRs was carried out through modification of the Stöber method[229] which proceeds via the hydrolysis of alkyl silicates and the subsequent condensation of the hydrolyzed product (orthosilicic acid) in alcoholic solutions at alkaline pH to form silica NPs. In order to functionalize GNRs with silica shells of different thickness, the concentration of CTAB, which will serve as the template for silica deposition, should be firstly adjusted in the as-synthesized GNRs solution.[89] To do that, the as-synthesized GNRs@CTAB solution was divided into equal volumes (~50 mL) in 50 mL falcon tubes and was subsequently washed by two consecutive cycles of centrifugation at 8000 rpm for 20-30 min. The resultant pellet was resuspended in 5 mL of MQ water and pooled together so that to bring the total volume of GNR solution into 50 mL with a final CTAB concentration of about 15 mM (initial concentration of CTAB in the as-synthesized GNR solution is 37 mM).

To start the silanization of GNRs, 10 mL of 1 nM GNRs was mixed with different volumes of CTAB solution (100 mM) in 20 mL scintillation vials for 12 h to bring the final concentration of CTAB below or well close to the critical micelle concentration of CTAB (0.90–0.98 mM).[90] Adjusting the CTAB concentration is very crucial to obtain different thickness of silica shells.[89] The pH of the resultant solutions was adjusted to 10.3–10.6 by mixing them with 40–50 μL of NaOH (100 mM) for 30 min, afterwards, 90 μL of methanolic TEOS solution (20%) was added dropwise over a period of 3 min at a low stirring rate for 30 min, after which, the vials were removed and incubated at 30° C undisturbed for 24 h. The resultant solutions were transferred to 50 mL centrifugation tubes and were purified under centrifugation at 9000 rpm for 30 min. The purification was accomplished by 3–5 centrifugation cycles using methanol to remove free silica formed apart from the plasmonic cores. The final pellets were redispersed in 5 mL of methanol for further use.

5.3.1.5 Functionalization of GNRs@SiO₂ with GNCs

The conjugation of the silanized GNRs (GNRs@SiO₂) with the fluorescent glutathione-capped GNCs was performed through our developed method. To functionalize the silanized GNRs with GNCs, the surfaces of the silanized GNRs were first modified with amino groups through their reaction with APTES. In brief, 2 mL of the previously obtained GNRs@SiO₂ was mixed with 0.5 mL of methanolic APTES solution (20%) under moderate stirring at 37° C for 24 h. The reaction mixtures were then transferred into centrifuge tubes and washed two times by MQ water by centrifugation at 5000 rpm for 45 min and the pellets were resuspended in 2 mL MQ water. The silanized GNRs with terminal amino groups after APTES functionalization are now ready to interact with the activated carboxylic groups of GSH-capped GNCs. The terminal carboxylic groups of GNCs@GSH were activated through the EDC chemistry to facilitate their interaction with NH₂-functionalized GNRs. In a typical experiment, 0.5 mL of GSH-capped GNCs was allowed to react with a mixture of 50 μL of EDC solution (100 mM) and 150 μL of NHS (100 mM) in a 3 mL of HEPES buffer (20 mM, pH 7.4) under vigorous stirring for 10 min at 37° C. Afterwards, 1.5 mL of amine terminated GNRs@SiO₂ was injected to the reaction mixture. The reaction mixture was stirred at moderate rate while incubated for 12 h at 37° C in the dark. The resultant GNC-functionalized GNRs@SiO₂ solutions were purified by 2–3 cycles of centrifugation at 5000 rpm for 45 min until all the free GNCs are collected in supernatants. The pellets were resuspended in 2 mL of MQ water for further assessments.

5.3.1.6 Colloidal stability studies

The colloidal stability of GNRs, GNRs@GNCs, GNRs@LBL and GNRs@SiO₂@GNCs have been studied in different ionic strength solutions of NaCl as well as in different biological media such as PBS, FBS-supplemented DMEM, FBS-free DMEM, FBS-supplemented RPMI, and FBS-free RPMI by recording the change in their UV-vis extinction spectra over time. For that, 0.1 mL of GNRs solutions was incubated with 0.9 mL of NaCl solutions of different ionic strengths (25 - 1250 mM) or with 0.9 mL of PBS, FBS-supplemented DMEM, FBS-free DMEM, FBS-supplemented RPMI, and FBS-free RPMI and the UV-vis of different GNRs were recorded directly after incubation (0 h) as well as after 6 h and 24 h post-incubation.

5.3.1.7 Evaluating plasmon-enhanced fluorescence of GNRs@SiO₂@GNCs as a function of distance from plasmonic GNRs

The fluorescence behavior of GNCs as a function of distance from the surfaces of the plasmonic GNRs have been studied using the silica shell dielectric spacer. The GNRs were firstly coated with different silica shell thickness (~ 21-29 nm) and the resultant silica-coated GNRs were then functionalized by GNCs as described above. The as-synthesized GNRs@SiO₂@GNCs were purified by 2-3 cycles of centrifugation at 5000 rpm for 45 min until all the free GNCs are collected in supernatants. The pellets were resuspended in 2 mL of MQ water and the supernatants were saved for further assessments. The fluorescence intensity of NPs was then recorded under UV lamp and was evaluated using spectrofluorometer (λ_{exc} = 365 nm).

5.3.1.8 Evaluating the thermal stability of GNRs

To study the thermal stability of GNRs before and after functionalization with silica shell and GNCs, in situ TEM heating experiments were carried out. The in situ heating was carried out in a TEM facility equipped with a high-temperature specimen stage which allows the heating of samples at different temperature (25-1000°C). The in situ TEM facilitates the real-time imaging of heating-induced morphological and structural changes of GNRs systems as well as the conjugated GNCs. The TEM images were taken after approx. 60 min dwell time at a given temperature.

5.3.1.9 Evaluating the photothermal stability of GNRs

The photothermal stability of GNRs of different AR (LSPR= 800 nm and 975), GNRs@SiO₂ of different thickness and their corresponding GNRs@SiO₂@GNCs were studied by recording the optical changes in the UV-vis spectra as well as the morphological changes through TEM imaging after irradiating the NPs with different nanosecond (ns) laser pulses. In brief, 500 μL sample of different GNRs was transferred into a glass cuvette with a path length of 10 mm and was stirred during laser irradiation in order to ensure all NPs will be homogeneously irradiated with laser pulses. Nanosecond laser pulses were generated by a Nd:YAG laser source (Innolas, SpitLight DPSS250-100) with a pulse width of 9 ns and a wavelength of 1064 nm. The pulse repetition frequency was set at 100 Hz. This produced pulse energy of 10 mJ and total energy fluence per pulse of 320 mJ/cm². After the GNRs were irradiated with different laser pulses (200-9000 pulses), the changes in their optical properties were studied by recording the UV-vis spectra of the irradiated GNRs using UV-vis spectroscopy, whereas, the morphological and structural changes of GNRs and GNCs were probed by TEM imaging of a drop-casted specimen of the irradiated samples. The fluorescence of the irradiated samples of GNRs@SiO₂@GNCs was also recorded to check the robustness of the conjugated GNCs after the ns laser irradiation.

5.3.2 BSA-directed synthesis of colloidally stable and biocompatible Au nanopopcorn

5.3.2.1 Synthesis of NPs

The BSA-protected GNPCs were synthesized via a two-step seed-mediated route. The seeds were first prepared by mixing 25 μL of 100 mM sodium citrate with 10 mL of Milli-Q water in 40 mL scintillation vial and was then heated to 90 °C. Then, 25 μL of 100 mM HAuCl₄ and 50 μL of 20 mM freshly prepared NaBH₄ were simultaneously injected to the reaction mixture under moderate stirring for 30 s. The resulting seed NP solution was allowed to cool down to room temperature and was aged for 24 h in the fridge before any further use. The growth of the seed was carried out by mixing 50 μL of 100 mM HAuCl₄, 60 μL of 750 μM BSA, 300 μL of seed NPs, and 60 μL of 100 mM ascorbic acid with 10 mL of MQ water in a 40 mL scintillation vial under moderate stirring for 30 min. The successful synthesis of GNPC@BSA was confirmed by the appearance of deep blue color.

Similar procedure was followed to check whether different surface ligands are able to produce the popcorn by replacing the BSA with other ligands. The scale-up synthesis of GNPCs was carried out by simply increasing the volumes of all solution by a factor of 25.

The role of surface capping agents in dictating the physicochemical and biological properties of NPs, three NPs of almost similar size were prepared for the sake of comparing their colloidal stability and cytotoxicity with those of our GNPCs@BSA.

The **50 nm citrate-capped GNP** was synthesized according to a previously reported method.[230] Briefly, seeds of 18 nm diameter were firstly synthesized by heating 150 mL of 1.32 mM sodium citrate until boiling in a 250 mL three-necked flask under reflux. Then, 1.5 mL of 25 mM HAuCl₄ was injected to the reaction mixture after 5-10 minutes of boiling under vigorous stirring. An immediate color change to soft red indicates the successful synthesis of NPs. The resultant solution was boiled for additional 10 min before being removed.

The growth of seeds was performed as follows: 1 mL of 25 mM HAuCl₄ solution was mixed with the seed solution at 90 °C and HAuCl₄ under moderate stirring for 30 min. Two more injections of HAuCl₄ separated by 30 min interval were done. Then, 55 mL was taken out from the reaction vessel followed by the addition of 53 mL of MQ water and 2 mL of 60 mM SC. The previous procedure was repeated for 4 times after which GNPs of 50 nm can be obtained.

The synthesis of **surfactant-free gold nanostars** was performed using a previously reported seed-mediated approach.[231] The seed NPs were firstly prepared by mixing 15 mL of 1% sodium citrate solution with 100 mL of 1 mM boiling solution of HAuCl₄ under vigorous stirring for 15 min. The resultant solution was then cooled down to room temperature and filtered using a 0.22 μm nitrocellulose membrane and was kept subsequently at 4 °C. The growth of GNS was carried out by mixing 10 mL of 0.25 mM HAuCl₄ with 100 μL of the seed solution. Shortly after that, 50 μL of 100 mM ascorbic acid and 100 μL of 3 mM AgNO₃ were simultaneously injected under vigorous stirring for 30 s. The appearance of greenish-black color confirms the formation of GNS.

The synthesis of **CTAB-protected GNPC** was performed through the seed-mediated growth.[36] The seed solution was firstly prepared by mixing 60 μL of 100 mM freshly prepared NaBH₄ with 20 mL solution composed of 0.1 mM sodium citrate and 0.25 mM HAuCl₄ under vigorous stirring. The color turns immediately into wine red which confirms the formation of seed GNPs.

The growth of GNPC was then carried out by mixing 46.88 mL of 3 mM CTAB with 2 mL of 10 mM HAuCl₄ and 0.3 mL of 10 mM AgNO₃ under moderate stirring. Then, 0.32 mL of 100 mM ascorbic acid was added drop wise and the color immediately changed to colorless. Then, 500 µL of seed solution was subsequently injected. The color instantly turns to deep blue within 2 min, which indicates the formation of GNPC@CTAB.

5.3.2.2 Colloidal stability Studies

The colloidal stability of GNPs in MQ water and biological media was studied by DLS.[150] To assess their colloidal stability, 100 µL of different GNP solutions was incubated with 900 µL of MQ water, PBS, and DMEM+FBS for up to 36 h (up to 7days for GNPC@BSA and GNPC@CTAB). The hydrodynamic diameter (d_h) of the respected GNP was then measured over time using DLS and the mean d_h values were determined from the intensity distribution curves.

5.3.2.3 Biocompatibility studies of NPs

The cytotoxicity of GNPs was evaluated in HeLa cells as well as the Medical Research Council cell strain 5 (MRC-5) cells using the previously reported Resazurin assay.[65] In brief, HeLa and MRC-5 cells were plated in 96 well plate (cell density= 7500 cells/well) and kept for 24 h (37°C, 5% CO₂). The cells were then incubated with different concentrations of NPs (C_{Au} , mass concentration elemental gold as determined by inductively coupled plasma-mass spectrometry (ICP-MS)) for 24 and 48 h. The cells were subsequently washed with PBS and was incubated with 10% Resazurin solution for another 4 h (37°C, 5% CO₂). The fluorescence intensity of wells was then recorded using a spectrofluorometer equiposed with microplate reader and the % cell viability after exposure to different NPs was assessed compared to the control (untreated cells). Viability data are provided as mean value \pm SD from three independent experiments at different passage number.

The membrane integrity of HeLa cells and MRC-5 cells was evaluated using the Promega CytoTox-ONE™ Homogeneous Membrane Integrity Assay (Promega, USA) according to the manufacturer's instructions. In brief, cells were seeded in 96 well plate at a density of 7500 cells/well and were kept for 24 h (37°C, 5% CO₂). The cells were then incubated with different concentrations of NPs for 24 and 48 h. Then, 100 µL of CytoTox-ONE™ Reagent containing diaphorase and resazurin was added to 100 µL of cell culture medium present in each well, and the plate was shaken for 30 s and incubated at room temperature for 10 min. The reaction was

subsequently terminated by adding 50 μL of stop solution to each well, and the plate was shaken for 10 s. The fluorescence intensity of each well was recorded using microreader-equipped spectrofluorometer ($\lambda_{\text{exc}}= 560 \text{ nm}$ and $\lambda_{\text{em}}= 590 \text{ nm}$). The maximum LDH release ($R_{\text{LDH}} = 100\%$) was carried out by lysing the cells using Triton X-100 solution (9% wt./vol.) and was defined as 100% leakage (positive control), with the fluorescence intensity $I_{\text{cells+Triton}}$. The % LDH release ($R_{\text{LDH}} \%$) due to exposure of cells to NPs is proportional to the percentage of dead cells in each well and can be calculated as follows:

$$R_{\text{LDH}}(\%) = \frac{(I_{\text{Cells+NPs}} - I_{\text{Cells}})}{(I_{\text{Cells+Triton}} - I_{\text{Cells}})} \times 100$$

5.3.3 BSA-directed synthesis of Porous Bimetallic AgPt NPs with pH-switchable nanozyme activity and cargo loading capability

5.3.3.1 Synthesis of NPs

The synthesis of silver nanoprism was carried out using a seed-mediated approach.[65] First, the seed NPs were prepared by mixing 25 μL of 100 mM AgNO_3 and 25 μL of 100 mM sodium citrate in a scintillation vial containing 10 mL of MQ water and the mixture was heated to 90 $^\circ\text{C}$ under vigorous stirring for 15-20 min. Then, 100 μL of 20 mM freshly prepared NaBH_4 was injected rapidly to the reaction mixture. The color turns light-yellow instantly, which confirms the successful synthesis of seed NPs. The solution was then cooled down to room temperature, after which the vial was covered with aluminum foil and was aged for 24 h at 4 $^\circ\text{C}$. The growth of Ag nanoprism was carried out by mixing 10 mL of MQ water with 50 μL of 100 mM AgNO_3 , 120 μL of 752 μM BSA, and 300 μL of seed solution in a 20 mL scintillation vial under vigorous stirring. Then, 60 μL of 100 mM ascorbic acid was subsequently injected and the solution kept under stirring for 25 min. The successful synthesis of Ag nanoprism was confirmed by the appearance of violet color and the characteristic plasmonic peaks of Ag nanoprism.[232] The NPs were then purified by two cycles of centrifugation at 9000 rpm for 15 minutes. The pellet was redispersed in MQ water for further work.

The synthesis of porous bimetallic AgPt NPs was carried out by mixing 50 μL of 25 mM platinum precursor (H_2PtCl_6) with 10 mL of purified Ag nanoprism solution under vigorous stirring for 15 min. After which the color of the solution turns dark navy blue. The NPs were then

purified by two consecutive cycles of centrifugation (9000 rpm, 15 minutes). The pellet was redispersed in MQ water for further work. The effect of changing the amount and concentration of H_2PtCl_6 on the properties of the resultant AgPt bimetallic NPs was investigated by mixing the Ag nanoprism solution with different amounts of 2 mM and 25 mM H_2PtCl_6 . Similar procedure was used for the synthesis of AgPd and AgAu bimetallic NPs by replacing the H_2PtCl_6 solution with PdCl_2 and HAuCl_4 solutions, respectively.

The effect of changing the Ag:Pt molar ratio of the AgPt NPs on the elemental composition of the resulting AgPt NPs was evaluated by inductively coupled plasma mass spectrometry (ICP-MS) using a previously reported method.⁵

5.3.3.2 Concentration determination of NPs

Determining of the concentration of complex-shaped NPs is complicated and often can only be estimated.^[233] One approach lies in calculating the volume and mass of NP using the density of the NP material. Using the elemental concentration in a NP solution using ICP-MS results allows then for estimating the molar concentration of NPs in the solution.^[150] It has to be pointed out, however, that these calculations are rough estimates.

To calculate the concentration of AgPt NPs, the surface area of the triangular prism (A_{NP}) was calculated using the Heron's formula^[234] as follows:

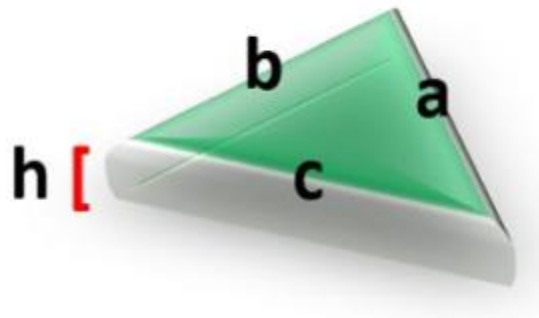
$$A_{NP} = \sqrt{S(S-a)(S-b)(S-c)}$$

Where side lengths of the triangular prism $a \simeq b \simeq c \simeq LE \approx 45$ nm (values roughly estimated from the TEM images) and S is the semiperimeter of the prism and calculated using the following formula:

$$S = \frac{1}{2} (a + b + c)$$

The volume of each triangle (V_{NP}) was then calculated as follows.

$$V_{NP} = \frac{1}{4} h \sqrt{2(ab)^2 - a^4 + 2(ac)^2 - b^4 + 2(bc)^2 - c^4}$$



Where h is the height of the prisms and is ≈ 15 nm.

The volume of single NP (V_{NP}) is therefore $\approx 1.3 \times 10^{-17}$ cm³. The mass of single NP (m_{NP}) can be calculated as follows:

$$m_{NP} = V_{NP} \times \rho_{NP}$$

Where ρ_{NP} is the material density and is equal to that of Ag, $\rho_{NP} = \rho_{Ag} = 10.5$ g/cm³.

Therefore, the mass of single NP is $= 1.4 \cdot 10^{-13}$ mg.

The concentration of the NPs could be then estimated using the elemental concentration measured by ICP-MS. The number concentration of NPs in the solution (N_{NP}) can be calculated as follows:

$$N_{NP} = C_{Ag} / m_{NP}$$

Where C_{Ag} is the elemental concentration of Ag. In one representative experiment C_{Ag} was measured 84 mg/L and this led to $N_{NP} \approx 6 \times 10^{14}$ NPs/L. The molar concentration of the NPs (c_{NP}) can be then calculated as follows:

$$c_{NP} = N_{NP} / N_A$$

Where N_A is the Avogadro's number. Hence the concentration of NPs (c_{NP}) in the example is ≈ 0.996 nM ≈ 1 nM.

We want to emphasize again that this calculations are rough estimates and the concentration of AgPt NPs is assumed to be equivalent to the concentration of original Ag NPs sacrificial templates.

5.3.3.3 Colloidal stability studies

The colloidal stability of Ag NPs and AgPt NPs in NaCl solutions and different biological media was studied by DLS.[150] To assess the colloidal stability, 100 μ L of different NP solutions was incubated with 900 μ L of different ionic strength NaCl, PBS, DMEM-FBS, DMEM+FBS, RPMI-FBS, or RPMI+FBS for up to 24 h. The hydrodynamic diameter (d_h) of the respected NP was then measured over time (0 h, 6 h, 12 h, and 24 h post-incubation) using DLS and the mean d_h values were determined from the intensity distribution curves.

5.3.3.4 Peroxidase-like activity of AgPt NPs

The peroxidase-mimic activity of NPs was investigated through the catalytic oxidation of the colorless peroxidase substrate ortho-phenylenediamine (OPD) in the presence of H_2O_2 to produce a yellow colored 2,3-diaminophenazine (DAP). In brief, 25 μ L of AgPt NPs (final concentration, $c_{NP} = 0.0332$ nM) was mixed with 3 mL sodium acetate buffer (pH 4) and freshly prepared OPD (0.32 mM) in the presence of H_2O_2 (312.6 mM) at 37°C. UV-vis absorption spectra were recorded at 2 min time interval, for a period of 22 min and the reaction kinetics were determined thereof.

The peroxidase-like activity of the AgPt NPs was compared to that of the standard horseradish peroxidase (HRP) by replacing the NPs with the same amount of HRP (final concentration, $c_{HRP} = 0.1$ nM). Control experiments were carried out where MQ water, Pt NPs of an equivalent Pt content, Ag nanoprisms, Ag NPs@SC and AgPt NPs@SC replaced the AgPt NPs. The peroxidase-like activity of AgPt NPs was also investigated at pH 7 and 11 following the same protocol with replacing the sodium acetate buffer with phosphate buffer solutions of pH 7 and 11, respectively. The effect of changing the elemental composition of AgPt NPs on their peroxidase-like activity was also investigated following the same protocol.

The reaction rates (V) of OPD oxidation which also corresponds to the amount of DAP produced in a unit time using different NPs and different concentration of the substrates (OPD and H_2O_2) have been calculated by plotting the absorption values at $\lambda = 425$ nm as a function of time, then the data points have been fitted using second-order polynomial fit. The reaction rate (V) could be then

calculated by dividing the regression coefficient (B1) values extracted from the quadratic equation ($y = \text{Intercept} + B1 \cdot x1 + B2 \cdot x2$) of the fit model by the extinction coefficient of DAP.

The steady-state kinetic parameters of the OPD oxidation reaction, K_m , and V_{max} , were evaluated by plotting the obtained reaction rate values, while varying the concentration of either the peroxidase substrate, OPD or H_2O_2 and keeping the other constant. The K_m and V_{max} values are generated after fitting the substrate concentration dependent reaction rate curves to the Michaelis-Menten fit model.

5.3.3.5 Catalase-like activity of AgPt NPs

The catalase-mimic activity of AgPt NPs was evaluated by monitoring their ability to decompose H_2O_2 and the generation of O_2 . In a typical experiment, the catalase-like activity was performed by mixing 1 mL of AgPt NPs ($C_{NP} = 0.0332 \text{ nM}$) with 5 mL of phosphate buffer solution (pH 11) in the presence of H_2O_2 (750 mM) at room temperature and the dissolved oxygen levels (C_{O_2}) were recorded using an Extech DO210 model dissolved oxygen meter every minute over a period of 10 min and the reaction rates of the catalase-like activity were evaluated by plotting concentrations of the liberated oxygen versus time.

The catalase-like activity of the AgPt NPs was compared to that of the catalase by replacing the NPs with the same amount of catalase (20 U/mL).

Control experiments were carried out where MQ water, Pt NPs of an equivalent Pt content, Ag nanoprisms, Ag NPs@SC and AgPt NPs@SC replaced the AgPt NPs. The catalase-like activity of AgPt NPs was also investigated at pH 4 and 7 following the same protocol with replacing the phosphate buffer solution (pH 11) with sodium acetate buffer (pH 4) and phosphate buffer solutions (pH 7), respectively. The effect of changing the elemental composition of AgPt NPs on their peroxidase-like activity was also investigated following the same protocol.

The rate of catalytic reaction and steady state kinetics as a function of varying the concentrations of H_2O_2 were evaluated as described above in case of peroxidase-like activity.

5.3.3.6 Cargo-loading/controlled-release into/from the AgPt NPs

In order to evaluate the cargo-loading efficiency of the porous AgPt NPs, the hydrophilic calcein dye was used as model cargo. In brief, 10 mL of NPs solutions was mixed with 1.5 mL calcein solution of different concentrations in a 20 mL scintillation vial under moderate stirring for 60 min. Unbound calcein dye was then removed by repetitive centrifugation and washing with MQ water until no further calcein could be detected. The concentration of free unbound calcein in the supernatants could be evaluated by recording the absorption and fluorescence spectra ($\lambda_{ex} = 490$ nm and $\lambda_{em} = 515$ nm) using a calibration curve.

AgPt NPs were then incubated with different amounts of calcein dye, to assess their loading content (LC) (mg calcein/mg AgPt NPs) and % loading efficiency (LE) using the following formulas:

$$\text{Calcein loading content} = \frac{\text{Weight of entrapped calcein}}{\text{Weight of NPs}}$$

$$\text{Loading efficiency (\%)} = \frac{\text{Weight of entrapped calcein}}{\text{Total weight of added calcein}} \times 100$$

The triggered calcein release from AgPt NPs was evaluated by recording the fluorescence intensity of calcein-loaded NPs before and after the addition of H₂O₂. In brief, 20 μ L of 30% H₂O₂ was added to 1 mL of calcein-loaded NPs. The fluorescence intensity was then immediately recorded at $\lambda_{em} = 515$ nm.

5.4 List of hazardous substances used in the work

Chemical	CAS-No.	GHS Pictogram(s)	H-Sentences (Hazard)	P-Sentences (Precaution)
Silver nitrate	7761-88-8		H272-H290-H314-H410	P210-P220-P260-P273-P280-P303 + P361 + P353-P304 + P340 + P310-P305 + P351 + P338-P370 + P378-P391
CTAB	57-09-0		H302-H315-H318-H335-H373-H400	P260-P280-P301 + P312 + P330-P305 + P351 + P338 + P310
NaBH ₄	16940-66-2		H260-H301-H314-H360F	P201-P231 + P232-P280-P308 + P313-P370 + P378-P402 + P404
HAuCl ₄	27988-77-8		H302-H314-H317	P280-P305 + P351 + P338-P310
HCl	7647-01-0		H290-H314-H335	P260-P280-P303 + P361 + P353-P304 + P340 + P310-P305 + P351 + P338 + P310
TEOS	78-10-4		H226-H319-H332-H335	P210-P261-P280-P303 + P361 + P353-P304 + P340 + P312-P370 + P378
APTES	919-30-2		H302-H314-H317	P280-P305 + P351 + P338-P310
EDC	1892-57-5		H314	P280-P305 + P351 + P338-P310

H ₂ PtCl ₆	18497-13-7		H301-H314- H317-H334	P261-P280-P301 + P310-P305 + P351 + P338- P310
PdCl ₂	7647-10-1		H301-H317	P280-P301 + P310
Methanol	67-56-1		H225 - H301+H311 +H331 - H370	P210 - P233 - P240 - P241 - P242 - P243 - P260 - P264 - P270 - P271 - P280 - P301+P310 - P303+P361+P35 3 - P304+P340 - P330 - P361+P364 - P370+P378 - P501
Calcein	154071-48- 4		H302- H312- H315- H319- H332- H335	P261, P264, P270, P271, P280, P301+P312, P302+P352, P304+P312, P304+P340, P305+P351+P33 8, P312, P321, P322, P330, P332+P313, P337+P313, P362, P363, P403+P233, P405, and P501
Nitric acid	7697-37-2		H272-H290- H314	P210-P220- P260-P280-P305 + P351 + P338- P370 + P378
o- Phenylenediamin e	95-54-5		H301-H312 + H332- H317-H319- H341-H351- H410	P261-P280-P305 + P351 + P338
Hydrogen peroxide	7722-84-1		H302-H318- H412	P280-P301 + P312 + P330- P305 + P351 + P338 + P310

Triton™ X-100	9002-93-1		H302-H315-H318-H410	P280-P301 + P312 + P330-P305 + P351 + P338 + P310
Resazurin	62758-13-8		H315 -H319-H335	P264- P280-P362+364-P261-P302+352-P332+313-P305+351+338-P337+313-P309+311-P304+340
NaOH	1310-73-2		H290-H314	P260-P280-P303 + P361 + P353-P304 + P340 + P310-P305 + P351 + P338
Bovine serum albumin	9048-46-8	Not hazardous substance		
GSH	70-18-8	Not hazardous substance		
Ascorbic Acid	50-81-7	Not hazardous substance		
NaOL	143-19-1	Not hazardous substance		
NHS	6066-82-6	Not hazardous substance		
Sodium citrate	6132-04-3	Not hazardous substance		

References

1. Dreaden, E.C., et al., *The golden age: gold nanoparticles for biomedicine*. Chemical Society Reviews, 2012. **41**(7): p. 2740-2779.
2. Bhatia, S., *Nanoparticles types, classification, characterization, fabrication methods and drug delivery applications*, in *Natural polymer drug delivery systems*. 2016, Springer. p. 33-93.
3. Taniguchi, N., *On the basic concept of nanotechnology*. Proceeding of the ICPE, 1974.
4. Feynman, R.P., *There's plenty of room at the bottom*. California Institute of Technology, Engineering and Science magazine, 1960.
5. Faraday, M., X. *The Bakerian Lecture. —Experimental relations of gold (and other metals) to light*. Philosophical Transactions of the Royal Society of London, 1857(147): p. 145-181.
6. Zhang, Y., et al., *Chemical reactivities of magnesium nanopowders*. Journal of Nanoparticle Research, 2001. **3**(1): p. 23-26.
7. Gao, J. and M. Xu, *Metal nanoparticles of various shapes*. Advantages of Metal Nanoparticles, 2007.
8. Orendorff, C.J. and C.J. Murphy, *Quantitation of metal content in the silver-assisted growth of gold nanorods*. The Journal of Physical Chemistry B, 2006. **110**(9): p. 3990-3994.
9. Rana, S. and P. Kalaichelvan, *Antibacterial activities of metal nanoparticles*. Antibacterial Activities of Metal Nanoparticles, 2011. **11**(02): p. 21-23.
10. Nel, A.E., et al., *Understanding biophysicochemical interactions at the nano–bio interface*. Nature materials, 2009. **8**(7): p. 543-557.
11. Stoeva, S., et al., *Gram-scale synthesis of monodisperse gold colloids by the solvated metal atom dispersion method and digestive ripening and their organization into two-and three-dimensional structures*. Journal of the American Chemical Society, 2002. **124**(10): p. 2305-2311.
12. Prasad, B., et al., *Digestive-ripening agents for gold nanoparticles: alternatives to thiols*. Chemistry of Materials, 2003. **15**(4): p. 935-942.
13. Jana, N.R., L. Gearheart, and C.J. Murphy, *Wet chemical synthesis of high aspect ratio cylindrical gold nanorods*. The Journal of Physical Chemistry B, 2001. **105**(19): p. 4065-4067.
14. Wu, H.-L., C.-H. Kuo, and M.H. Huang, *Seed-mediated synthesis of gold nanocrystals with systematic shape evolution from cubic to trisoctahedral and rhombic dodecahedral structures*. Langmuir, 2010. **26**(14): p. 12307-12313.
15. Sun, S. and H. Zeng, *Size-controlled synthesis of magnetite nanoparticles*. Journal of the American Chemical Society, 2002. **124**(28): p. 8204-8205.
16. Sánchez-Iglesias, A., et al., *Binary Self-Assembly of Gold Nanowires with Nanospheres and Nanorods*. Angewandte Chemie International Edition, 2010. **49**(51): p. 9985-9989.
17. Habouti, S., et al., *Self-standing corrugated Ag and Au-nanorods for plasmonic applications*. Journal of Materials Chemistry, 2011. **21**(17): p. 6269-6273.
18. Rodríguez-Lorenzo, L., et al., *Reshaping and LSPR tuning of Au nanostars in the presence of CTAB*. Journal of Materials Chemistry, 2011. **21**(31): p. 11544-11549.
19. Huang, X., et al., *Photochemically controlled synthesis of anisotropic Au nanostructures: platelet-like Au nanorods and six-star Au nanoparticles*. ACS nano, 2010. **4**(10): p. 6196-6202.
20. Zhang, H., et al., *Shape-controlled synthesis of Pd nanocrystals and their catalytic applications*. Accounts of chemical research, 2012. **46**(8): p. 1783-1794.
21. Ke, F.-S., et al., *Enhanced electrocatalytic activity on gold nanocrystals enclosed by high-index facets for oxygen reduction*. Nano Energy, 2014. **7**: p. 179-188.
22. Huang, X., et al., *Cancer cell imaging and photothermal therapy in the near-infrared region by using gold nanorods*. Journal of the American Chemical Society, 2006. **128**(6): p. 2115-2120.

23. Park, J.H., et al., *Systematic surface engineering of magnetic nanoworms for in vivo tumor targeting*. *small*, 2009. **5**(6): p. 694-700.
24. Geng, Y., et al., *Shape effects of filaments versus spherical particles in flow and drug delivery*. *Nature nanotechnology*, 2007. **2**(4): p. 249-255.
25. Iijima, S., *Helical microtubules of graphitic carbon*. *nature*, 1991. **354**(6348): p. 56-58.
26. Willets, K.A. and R.P. Van Duyne, *Localized surface plasmon resonance spectroscopy and sensing*. *Annu. Rev. Phys. Chem.*, 2007. **58**: p. 267-297.
27. Murphy, C.J., et al., *Anisotropic metal nanoparticles: synthesis, assembly, and optical applications*. 2005, ACS Publications.
28. Chen, D., et al., *Effects of morphologies on acetone-sensing properties of tungsten trioxide nanocrystals*. *Sensors and Actuators B: Chemical*, 2011. **153**(2): p. 373-381.
29. Jiang, R., et al., *Metal/semiconductor hybrid nanostructures for plasmon-enhanced applications*. *Advanced materials*, 2014. **26**(31): p. 5274-5309.
30. Banholzer, M.J., et al., *Rationally designed nanostructures for surface-enhanced Raman spectroscopy*. *Chemical Society Reviews*, 2008. **37**(5): p. 885-897.
31. Norman, R.S., et al., *Targeted photothermal lysis of the pathogenic bacteria, *Pseudomonas aeruginosa*, with gold nanorods*. *Nano letters*, 2008. **8**(1): p. 302-306.
32. Smith, A.M., M.C. Mancini, and S. Nie, *Bioimaging: second window for in vivo imaging*. *Nature nanotechnology*, 2009. **4**(11): p. 710.
33. Niidome, T., et al., *PEG-modified gold nanorods with a stealth character for in vivo applications*. *Journal of Controlled Release*, 2006. **114**(3): p. 343-347.
34. Reguera, J., et al., *Anisotropic metal nanoparticles for surface enhanced Raman scattering*. *Chemical Society Reviews*, 2017. **46**(13): p. 3866-3885.
35. Alkilany, A.M. and C.J. Murphy, *Toxicity and cellular uptake of gold nanoparticles: what we have learned so far?* *Journal of nanoparticle research*, 2010. **12**(7): p. 2313-2333.
36. Lu, W., et al., *Gold nano-popcorn-based targeted diagnosis, nanotherapy treatment, and in situ monitoring of photothermal therapy response of prostate cancer cells using surface-enhanced Raman spectroscopy*. *Journal of the American Chemical Society*, 2010. **132**(51): p. 18103-18114.
37. Yin, Y. and A.P. Alivisatos, *Colloidal nanocrystal synthesis and the organic-inorganic interface*. *Nature*, 2005. **437**(7059): p. 664-670.
38. Yu, W.W., Y.A. Wang, and X. Peng, *Formation and stability of size-, shape-, and structure-controlled CdTe nanocrystals: ligand effects on monomers and nanocrystals*. *Chemistry of Materials*, 2003. **15**(22): p. 4300-4308.
39. Shenhar, R., T.B. Norsten, and V.M. Rotello, *Polymer-mediated nanoparticle assembly: structural control and applications*. *Advanced Materials*, 2005. **17**(6): p. 657-669.
40. Lin, Y., et al., *Nanoparticle assembly and transport at liquid-liquid interfaces*. *Science*, 2003. **299**(5604): p. 226-229.
41. Balazs, A.C., T. Emrick, and T.P. Russell, *Nanoparticle polymer composites: where two small worlds meet*. *Science*, 2006. **314**(5802): p. 1107-1110.
42. Aldana, J., Y.A. Wang, and X. Peng, *Photochemical instability of CdSe nanocrystals coated by hydrophilic thiols*. *Journal of the American Chemical Society*, 2001. **123**(36): p. 8844-8850.
43. Sau, T.K. and C.J. Murphy, *Room temperature, high-yield synthesis of multiple shapes of gold nanoparticles in aqueous solution*. *Journal of the American Chemical Society*, 2004. **126**(28): p. 8648-8649.
44. Goodman, C.M., et al., *Toxicity of gold nanoparticles functionalized with cationic and anionic side chains*. *Bioconjugate chemistry*, 2004. **15**(4): p. 897-900.
45. Ling, D. and T. Hyeon, *Chemical design of biocompatible iron oxide nanoparticles for medical applications*. *small*, 2013. **9**(9-10): p. 1450-1466.

46. Chou, L.Y., K. Ming, and W.C. Chan, *Strategies for the intracellular delivery of nanoparticles*. Chemical Society Reviews, 2011. **40**(1): p. 233-245.
47. Verma, A., et al., *Surface-structure-regulated cell-membrane penetration by monolayer-protected nanoparticles*. Nature materials, 2008. **7**(7): p. 588-595.
48. Smith, A.M., et al., *Bioconjugated quantum dots for in vivo molecular and cellular imaging*. Advanced drug delivery reviews, 2008. **60**(11): p. 1226-1240.
49. Kievit, F.M. and M. Zhang, *Surface engineering of iron oxide nanoparticles for targeted cancer therapy*. Accounts of chemical research, 2011. **44**(10): p. 853-862.
50. Hauck, T.S., A.A. Ghazani, and W.C. Chan, *Assessing the effect of surface chemistry on gold nanorod uptake, toxicity, and gene expression in mammalian cells*. small, 2008. **4**(1): p. 153-159.
51. Alkilany, A.M., et al., *Cellular uptake and cytotoxicity of gold nanorods: molecular origin of cytotoxicity and surface effects*. small, 2009. **5**(6): p. 701-708.
52. Qiu, Y., et al., *Surface chemistry and aspect ratio mediated cellular uptake of Au nanorods*. Biomaterials, 2010. **31**(30): p. 7606-7619.
53. Vigderman, L., P. Manna, and E.R. Zubarev, *Quantitative replacement of cetyl trimethylammonium bromide by cationic thiol ligands on the surface of gold nanorods and their extremely large uptake by cancer cells*. Angewandte Chemie International Edition, 2012. **51**(3): p. 636-641.
54. Wang, L., et al., *Surface chemistry of gold nanorods: origin of cell membrane damage and cytotoxicity*. Nanoscale, 2013. **5**(18): p. 8384-8391.
55. Shen, S., et al., *Targeting mesoporous silica-encapsulated gold nanorods for chemo-photothermal therapy with near-infrared radiation*. Biomaterials, 2013. **34**(12): p. 3150-3158.
56. Åkerman, M.E., et al., *Nanocrystal targeting in vivo*. Proceedings of the National Academy of Sciences, 2002. **99**(20): p. 12617-12621.
57. Elzoghby, A.O., W.M. Samy, and N.A. Elgindy, *Protein-based nanocarriers as promising drug and gene delivery systems*. Journal of Controlled Release, 2012. **161**(1): p. 38-49.
58. Mizrahy, S. and D. Peer, *Polysaccharides as building blocks for nanotherapeutics*. Chemical Society Reviews, 2012. **41**(7): p. 2623-2640.
59. Gole, A. and C.J. Murphy, *Polyelectrolyte-coated gold nanorods: synthesis, characterization and immobilization*. Chemistry of Materials, 2005. **17**(6): p. 1325-1330.
60. Hu, X., et al., *Fabrication, characterization, and application in SERS of self-assembled polyelectrolyte-gold nanorod multilayered films*. The Journal of Physical Chemistry B, 2005. **109**(41): p. 19385-19389.
61. Shi, Z., et al., *Stability enhanced polyelectrolyte-coated gold nanorod-photosensitizer complexes for high/low power density photodynamic therapy*. Biomaterials, 2014. **35**(25): p. 7058-7067.
62. Irvani, S., *Green synthesis of metal nanoparticles using plants*. Green Chemistry, 2011. **13**(10): p. 2638-2650.
63. Virkutyte, J. and R.S. Varma, *Green synthesis of metal nanoparticles: biodegradable polymers and enzymes in stabilization and surface functionalization*. Chemical Science, 2011. **2**(5): p. 837-846.
64. Chauhan, B.P., *Novel Nanoscale Hybrid Materials*. 2018: John Wiley & Sons.
65. Chakraborty, I., et al., *Protein-mediated shape control of silver nanoparticles*. Bioconjugate chemistry, 2018. **29**(4): p. 1261-1265.
66. Zeng, Y., et al., *Understanding the Interaction of Glutamate Salts with Serum Albumin Protected Prism-Shaped Silver Nanoparticles toward Glutamate Sensing*. Particle & Particle Systems Characterization, 2019. **36**: p. 1800229.
67. Chakraborty, I. and W.J. Parak, *Protein-Induced Shape Control of Noble Metal Nanoparticles*. Advanced Materials Interfaces, 2019. **6**: p. 2196-7350.

68. Au, L., et al., *Synthesis of gold microplates using bovine serum albumin as a reductant and a stabilizer*. Chemistry—An Asian Journal, 2010. **5**(1): p. 123-129.
69. Yuan, H., et al., *Thousand-fold enhancement of single-molecule fluorescence near a single gold nanorod*. Angewandte Chemie International Edition, 2013. **52**(4): p. 1217-1221.
70. Yu, K., et al., *Damping of acoustic vibrations of immobilized single gold nanorods in different environments*. Nano letters, 2013. **13**(6): p. 2710-2716.
71. Schuller, J.A., et al., *Plasmonics for extreme light concentration and manipulation*. Nature materials, 2010. **9**(3): p. 193-204.
72. Mubeen, S., et al., *An autonomous photosynthetic device in which all charge carriers derive from surface plasmons*. Nature nanotechnology, 2013. **8**(4): p. 247-251.
73. Atwater, H.A. and A. Polman, *Plasmonics for improved photovoltaic devices*, in *Materials For Sustainable Energy: A Collection of Peer-Reviewed Research and Review Articles from Nature Publishing Group*. 2011, World Scientific. p. 1-11.
74. Petrova, H., et al., *On the temperature stability of gold nanorods: comparison between thermal and ultrafast laser-induced heating*. Physical Chemistry Chemical Physics, 2006. **8**(7): p. 814-821.
75. Khalavka, Y., et al., *Enhanced thermal stability of gold and silver nanorods by thin surface layers*. The Journal of Physical Chemistry C, 2007. **111**(35): p. 12886-12889.
76. Taylor, A.B., A.M. Siddiquee, and J.W. Chon, *Below melting point photothermal reshaping of single gold nanorods driven by surface diffusion*. ACS nano, 2014. **8**(12): p. 12071-12079.
77. Chen, Y.-S., et al., *Enhanced thermal stability of silica-coated gold nanorods for photoacoustic imaging and image-guided therapy*. Optics express, 2010. **18**(9): p. 8867-8878.
78. Chen, L.-C., et al., *Enhanced photoacoustic stability of gold nanorods by silica matrix confinement*. Journal of Biomedical optics, 2010. **15**(1): p. 016010.
79. Mitamura, K. and T. Imae, *Functionalization of gold nanorods toward their applications*. Plasmonics, 2009. **4**(1): p. 23.
80. Pastoriza-Santos, I., J. Pérez-Juste, and L.M. Liz-Marzán, *Silica-coating and hydrophobation of CTAB-stabilized gold nanorods*. Chemistry of Materials, 2006. **18**(10): p. 2465-2467.
81. Wu, Q., et al., *Quantum dots decorated gold nanorod as fluorescent-plasmonic dual-modal contrasts agent for cancer imaging*. Biosensors and Bioelectronics, 2015. **74**: p. 16-23.
82. Koole, R., et al., *On the incorporation mechanism of hydrophobic quantum dots in silica spheres by a reverse microemulsion method*. Chemistry of Materials, 2008. **20**(7): p. 2503-2512.
83. Ye, X., et al., *Using binary surfactant mixtures to simultaneously improve the dimensional tunability and monodispersity in the seeded growth of gold nanorods*. Nano letters, 2013. **13**(2): p. 765-771.
84. Gerion, D., et al., *Synthesis and properties of biocompatible water-soluble silica-coated CdSe/ZnS semiconductor quantum dots*. The Journal of Physical Chemistry B, 2001. **105**(37): p. 8861-8871.
85. Tang, F., L. Li, and D. Chen, *Mesoporous silica nanoparticles: synthesis, biocompatibility and drug delivery*. Advanced materials, 2012. **24**(12): p. 1504-1534.
86. Jalil, R.A. and Y. Zhang, *Biocompatibility of silica coated NaYF₄ upconversion fluorescent nanocrystals*. Biomaterials, 2008. **29**(30): p. 4122-4128.
87. Li, H., et al., *Near-infrared light-responsive supramolecular nanovalve based on mesoporous silica-coated gold nanorods*. Chemical Science, 2014. **5**(7): p. 2804-2808.
88. Gorelikov, I. and N. Matsuura, *Single-step coating of mesoporous silica on cetyltrimethyl ammonium bromide-capped nanoparticles*. Nano letters, 2008. **8**(1): p. 369-373.
89. Abadeer, N.S., et al., *Distance and plasmon wavelength dependent fluorescence of molecules bound to silica-coated gold nanorods*. ACS nano, 2014. **8**(8): p. 8392-8406.

90. Cifuentes, A., J.L. Bernal, and J.C. Diez-Masa, *Determination of critical micelle concentration values using capillary electrophoresis instrumentation*. Analytical Chemistry, 1997. **69**(20): p. 4271-4274.
91. Nooney, R.I., et al., *Self-assembly of mesoporous nanoscale silica/gold composites*. Langmuir, 2003. **19**(18): p. 7628-7637.
92. Rowe, L.R., B.S. Chapman, and J.B. Tracy, *Understanding and Controlling the Morphology of Silica Shells on Gold Nanorods*. Chemistry of Materials, 2018. **30**(18): p. 6249-6258.
93. Wang, C., et al., *Ultrathin Au nanowires and their transport properties*. Journal of the American Chemical Society, 2008. **130**(28): p. 8902-8903.
94. Geddes, C.D. and J.R. Lakowicz, *Metal-enhanced fluorescence*. Journal of Fluorescence, 2002. **12**(2): p. 121-129.
95. Lakowicz, J.R., *Radiative decay engineering 5: metal-enhanced fluorescence and plasmon emission*. Analytical biochemistry, 2005. **337**(2): p. 171-194.
96. Bardhan, R., et al., *Fluorescence enhancement by Au nanostructures: nanoshells and nanorods*. ACS nano, 2009. **3**(3): p. 744-752.
97. Fu, Y., J. Zhang, and J.R. Lakowicz, *Plasmon-enhanced fluorescence from single fluorophores end-linked to gold nanorods*. Journal of the American Chemical Society, 2010. **132**(16): p. 5540-5541.
98. Nepal, D., et al., *Large scale solution assembly of quantum dot–gold nanorod architectures with plasmon enhanced fluorescence*. Acs Nano, 2013. **7**(10): p. 9064-9074.
99. Gandra, N., et al., *Probing distance-dependent plasmon-enhanced near-infrared fluorescence using polyelectrolyte multilayers as dielectric spacers*. Angewandte Chemie International Edition, 2014. **53**(3): p. 866-870.
100. Bauch, M., et al., *Plasmon-enhanced fluorescence biosensors: a review*. Plasmonics, 2014. **9**(4): p. 781-799.
101. Kulakovich, O., et al., *Enhanced luminescence of CdSe quantum dots on gold colloids*. Nano Letters, 2002. **2**(12): p. 1449-1452.
102. Schmelzeisen, M., et al., *Fluorescence enhancement from individual plasmonic gap resonances*. Acs Nano, 2010. **4**(6): p. 3309-3317.
103. Chen, Y., K. Munechika, and D.S. Ginger, *Dependence of fluorescence intensity on the spectral overlap between fluorophores and plasmon resonant single silver nanoparticles*. Nano letters, 2007. **7**(3): p. 690-696.
104. Schietinger, S., et al., *Plasmon-enhanced single photon emission from a nanoassembled metal–diamond hybrid structure at room temperature*. Nano letters, 2009. **9**(4): p. 1694-1698.
105. Schietinger, S., et al., *Plasmon-enhanced upconversion in single NaYF₄: Yb³⁺/Er³⁺ codoped nanocrystals*. Nano letters, 2010. **10**(1): p. 134-138.
106. Munechika, K., et al., *Spectral control of plasmonic emission enhancement from quantum dots near single silver nanoprisms*. Nano letters, 2010. **10**(7): p. 2598-2603.
107. Abalde-Cela, S., et al., *Surface-enhanced Raman scattering biomedical applications of plasmonic colloidal particles*. Journal Of The Royal Society Interface, 2010. **7**: p. S435-S450.
108. Song, J.-H., et al., *Large enhancement of fluorescence efficiency from CdSe/ZnS quantum dots induced by resonant coupling to spatially controlled surface plasmons*. Nano letters, 2005. **5**(8): p. 1557-1561.
109. Gong, H.M., et al., *Illuminating dark plasmons of silver nanoantenna rings to enhance exciton–plasmon interactions*. Advanced Functional Materials, 2009. **19**(2): p. 298-303.
110. Ming, T., et al., *Strong polarization dependence of plasmon-enhanced fluorescence on single gold nanorods*. Nano letters, 2009. **9**(11): p. 3896-3903.
111. Kinkhabwala, A., et al., *Large single-molecule fluorescence enhancements produced by a bowtie nanoantenna*. Nature Photonics, 2009. **3**(11): p. 654-657.

112. Tam, F., et al., *Plasmonic enhancement of molecular fluorescence*. Nano letters, 2007. **7**(2): p. 496-501.
113. Bek, A., et al., *Fluorescence enhancement in hot spots of AFM-designed gold nanoparticle sandwiches*. Nano Letters, 2008. **8**(2): p. 485-490.
114. Viste, P., et al., *Enhancement and quenching regimes in metal– semiconductor hybrid optical nanosources*. ACS nano, 2010. **4**(2): p. 759-764.
115. Donehue, J.E., et al., *Plasmon-enhanced brightness and photostability from single fluorescent proteins coupled to gold nanorods*. The Journal of Physical Chemistry C, 2014. **118**(27): p. 15027-15035.
116. Fu, B., et al., *Super-resolving the distance-dependent plasmon-enhanced fluorescence of single dye and fluorescent protein molecules*. The Journal of Physical Chemistry C, 2015. **119**(33): p. 19350-19358.
117. DeVetter, B.M., R. Bhargava, and C.J. Murphy, *Computational Study of the Surface-Enhanced Raman Scattering from Silica-Coated Silver Nanowires*. Photochemistry and photobiology, 2014. **90**(2): p. 415-418.
118. Rodríguez-Fernández, J., et al., *The effect of silica coating on the optical response of sub-micrometer gold spheres*. The Journal of Physical Chemistry C, 2007. **111**(36): p. 13361-13366.
119. Wang, Y., S. Teitel, and C. Dellago, *Surface-driven bulk reorganization of gold nanorods*. Nano letters, 2005. **5**(11): p. 2174-2178.
120. Inasawa, S., M. Sugiyama, and Y. Yamaguchi, *Laser-induced shape transformation of gold nanoparticles below the melting point: the effect of surface melting*. The Journal of Physical Chemistry B, 2005. **109**(8): p. 3104-3111.
121. Link, S., et al., *Laser-induced shape changes of colloidal gold nanorods using femtosecond and nanosecond laser pulses*. The Journal of Physical Chemistry B, 2000. **104**(26): p. 6152-6163.
122. Smith, D.J., et al., *Dynamic atomic-level rearrangements in small gold particles*. Science, 1986. **233**(4766): p. 872-875.
123. Buffat, P. and J.P. Borel, *Size effect on the melting temperature of gold particles*. Physical review A, 1976. **13**(6): p. 2287.
124. Goldstein, A., C. Echer, and A. Alivisatos, *Melting in semiconductor nanocrystals*. Science, 1992. **256**(5062): p. 1425-1427.
125. Mohamed, M.B., Z.L. Wang, and M.A. El-Sayed, *Temperature-dependent size-controlled nucleation and growth of gold nanoclusters*. The Journal of Physical Chemistry A, 1999. **103**(49): p. 10255-10259.
126. Adair, J.H., et al., *Recent developments in the preparation and properties of nanometer-size spherical and platelet-shaped particles and composite particles*. Materials Science & Engineering R-Reports, 1998. **23**(4-5): p. 139-242.
127. Wang, Y. and C. Dellago, *Structural and morphological transitions in gold nanorods: A computer simulation study*. The Journal of Physical Chemistry B, 2003. **107**(35): p. 9214-9219.
128. Borisyuk, P., et al., *Method for measuring the melting temperature of gold nanoclusters on substrate surfaces*. Measurement Techniques, 2010. **53**(2): p. 128-133.
129. Chang, S.-S., et al., *The shape transition of gold nanorods*. Langmuir, 1999. **15**(3): p. 701-709.
130. Link, S., et al., *Laser photothermal melting and fragmentation of gold nanorods: energy and laser pulse-width dependence*. The Journal of Physical Chemistry A, 1999. **103**(9): p. 1165-1170.
131. Link, S., et al., *How long does it take to melt a gold nanorod?: A femtosecond pump–probe absorption spectroscopic study*. Chemical Physics Letters, 1999. **315**(1-2): p. 12-18.
132. Wenzel, T., et al., *Shaping nanoparticles and their optical spectra with photons*. Applied Physics B, 1999. **69**(5-6): p. 513-517.

133. Kurita, H., A. Takami, and S. Koda, *Size reduction of gold particles in aqueous solution by pulsed laser irradiation*. Applied Physics Letters, 1998. **72**(7): p. 789-791.
134. Takami, A., H. Kurita, and S. Koda, *Laser-induced size reduction of noble metal particles*. The Journal of Physical Chemistry B, 1999. **103**(8): p. 1226-1232.
135. Bosbach, J., et al. *Mechanistic studies and applications of laser-induced desorption from metal surfaces*. in *Laser Applications in Microelectronic and Optoelectronic Manufacturing IV*. 1999. International Society for Optics and Photonics.
136. González-Rubio, G., et al., *Femtosecond laser reshaping yields gold nanorods with ultranarrow surface plasmon resonances*. Science, 2017. **358**(6363): p. 640-644.
137. González-Rubio, G., A.s. Guerrero-Martínez, and L.M. Liz-Marzán, *Reshaping, fragmentation, and assembly of gold nanoparticles assisted by pulse lasers*. Accounts of chemical research, 2016. **49**(4): p. 678-686.
138. Horiguchi, Y., et al., *Photothermal reshaping of gold nanorods depends on the passivating layers of the nanorod surfaces*. Langmuir, 2008. **24**(20): p. 12026-12031.
139. Plech, A., et al., *Femtosecond laser near-field ablation from gold nanoparticles*. Nature Physics, 2006. **2**(1): p. 44-47.
140. Albrecht, W., et al., *Single particle deformation and analysis of silica-coated gold nanorods before and after femtosecond laser pulse excitation*. Nano letters, 2016. **16**(3): p. 1818-1825.
141. Saha, K., et al., *Gold nanoparticles in chemical and biological sensing*. Chemical Reviews, 2012. **112**(5): p. 2739-2779.
142. Daniel, M.C. and D. Astruc, *Gold Nanoparticles: Assembly, Supramolecular Chemistry, Quantum-Size-Related Properties, and Applications toward Biology, Catalysis, and Nanotechnology*. Chemical Reviews, 2004. **104**(1): p. 293-346.
143. Chakraborty, I. and T. Pradeep, *Atomically Precise Clusters of Noble Metals: Emerging Link between Atoms and Nanoparticles*. Chemical Reviews, 2017. **117**(12): p. 8208-8271.
144. Grzelczak, M., et al., *Shape control in gold nanoparticle synthesis*. Chemical Society Reviews, 2008. **37**(9): p. 1783-1791.
145. Li, N., P. Zhao, and D. Astruc, *Anisotropic Gold Nanoparticles: Synthesis, Properties, Applications, and Toxicity*. ANGEWANDTE CHEMIE-INTERNATIONAL EDITION, 2014. **53**(7): p. 1756-1789.
146. Giljohann, D.A., et al., *Gold Nanoparticles for Biology and Medicine*. Angewandte Chemie, International Edition, 2010. **49**(19): p. 3280-94.
147. Alvarez-Puebla, R.A., et al., *Self-assembled nanorod supercrystals for ultrasensitive SERS diagnostics*. Nano Today, 2012. **7**(1): p. 6-9.
148. Nel, A., et al., *Toxic potential of materials at the nanolevel*. Science, 2006. **311**(5761): p. 622-627.
149. Alkilany, A.M., et al., *Cellular uptake and cytotoxicity of gold nanorods: molecular origin of cytotoxicity and surface effects*. Small, 2009. **5**(6): p. 701-8.
150. Hühn, J., et al., *Selected Standard Protocols for the Synthesis, Phase Transfer, and Characterization of Inorganic Colloidal Nanoparticles*. Chemistry of Materials, 2017. **29**: p. 399-461.
151. Soliman, M.G., et al., *Phase transfer and polymer coating methods toward improving the stability of metallic nanoparticles for biological applications*. Chemistry of Materials 2015. **27**: p. 990-997.
152. Locatelli, E., I. Monaco, and M. Comes Franchini, *Surface modifications of gold nanorods for applications in nanomedicine*. RSC Advances, 2015. **5**(28): p. 21681-21699.
153. Pierrat, S., et al., *Self-assembly of small gold colloids with functionalized gold nanorods*. Nano Letters, 2007. **7**(2): p. 259-263.
154. Liao, H. and J.H. Hafner, *Gold Nanorod Bioconjugates*. Chemistry of Materials, 2005. **17**: p. 4636-4641.

155. Yu, C.X., L. Varghese, and J. Irudayaraj, *Surface modification of cetyltrimethylammonium bromide-capped gold nanorods to make molecular probes*. *Langmuir*, 2007. **23**(17): p. 9114-9119.
156. Menon, S., R. S, and V.K. S, *A review on biogenic synthesis of gold nanoparticles, characterization, and its applications*. *Resource-Efficient Technologies*, 2017. **3**(4): p. 516-527.
157. Xie, J., J.Y. Lee, and D.I.C. Wang, *Seedless, Surfactantless, High-Yield Synthesis of Branched Gold Nanocrystals in HEPES Buffer Solution*. *Chemistry of Materials*, 2007. **19**(11): p. 2823-2830.
158. Roth, K.L., X. Geng, and T.Z. Grove, *Bioinorganic Interface: Mechanistic Studies of Protein-Directed Nanomaterial Synthesis*. *Journal of Physical Chemistry C*, 2016. **120**(20): p. 10951-10960.
159. Lynch, I., et al., *The nanoparticle - protein complex as a biological entity; a complex fluids and surface science challenge for the 21st century*. *Advances In Colloid And Interface Science*, 2007. **134-35**: p. 167-174.
160. Carril, M., et al., *In situ detection of the protein corona in complex environments*. *Nature Communications*, 2017. **8**: p. 1542.
161. Monopoli, M.P., et al., *Physical-Chemical Aspects of Protein Corona: Relevance to in Vitro and in Vivo Biological Impacts of Nanoparticles*. *Journal of the American Chemical Society*, 2011. **133**(8): p. 2525-2534.
162. Corbo, C., et al., *The impact of nanoparticle protein corona on cytotoxicity, immunotoxicity and target drug delivery*. *Nanomedicine*, 2016. **11**(1): p. 81-100.
163. Mahmoudi, M., et al., *Protein-Nanoparticle Interactions: Opportunities and Challenges*. *Chemical Reviews*, 2011. **111**(9): p. 5610-5637.
164. Li, J., et al., *Controllable Synthesis of Stable Urchin-like Gold Nanoparticles Using Hydroquinone to Tune the Reactivity of Gold Chloride*. *The Journal of Physical Chemistry C*, 2011. **115**(9): p. 3630-3637.
165. Paul Reddy, K., et al., *High yield synthesis of branched gold nanoparticles as excellent catalysts for the reduction of nitroarenes*. *New Journal of Chemistry*, 2017. **41**(19): p. 11250-11257.
166. Gharib, M., et al., *Sustainable Synthesis and Improved Colloidal Stability of Popcorn-Shaped Gold Nanoparticles*. *ACS Sustainable Chemistry & Engineering*, 2019. **7**: p. 9834-9841.
167. Treuel, L., et al., *The Influence of Surface Composition of Nanoparticles on their Interactions with Serum Albumin*. *Chemphyschem*, 2010. **11**(14): p. 3093-3099.
168. Itri, R., et al., *Effect of urea on bovine serum albumin in aqueous and reverse micelle environments investigated by small angle X-ray scattering, fluorescence and circular dichroism*. *Brazilian Journal of Physics*, 2004. **34**: p. 58-63.
169. Micsonai, A., et al., *Accurate secondary structure prediction and fold recognition for circular dichroism spectroscopy*. *Proceedings of the National Academy of Sciences*, 2015: p. 201500851.
170. Lin, J., et al., *Biomimetic one-pot synthesis of gold nanoclusters/nanoparticles for targeted tumor cellular dual-modality imaging*. *Nanoscale Research Letters*, 2013. **8**(1): p. 170.
171. Chakraborty, I., et al., *Ion-selective ligands: how colloidal nano- and mirco-particles can introduce new functionalities*. *Zeitschrift für Physikalische Chemie*, 2018. **232**: p. 1307-1317.
172. Toshima, N. and T. Yonezawa, *Bimetallic nanoparticles—novel materials for chemical and physical applications*. *New Journal of Chemistry*, 1998. **22**(11): p. 1179-1201.
173. Koh, S. and P. Strasser, *Electrocatalysis on bimetallic surfaces: modifying catalytic reactivity for oxygen reduction by voltammetric surface dealloying*. *Journal of the American Chemical Society*, 2007. **129**(42): p. 12624-12625.
174. Link, S., Z.L. Wang, and M.A. El-Sayed, *Alloy formation of gold-silver nanoparticles and the dependence of the plasmon absorption on their composition*. *The Journal of Physical Chemistry B*, 1999. **103**(18): p. 3529-3533.

175. Sun, S., et al., *Monodisperse FePt Nanoparticles and Ferromagnetic FePt Nanocrystal Superlattices*. Science, 2000. **287**(March 17): p. 1989-1992.
176. Zaleska-Medynska, A., et al., *Noble metal-based bimetallic nanoparticles: the effect of the structure on the optical, catalytic and photocatalytic properties*. Advances in colloid and interface science, 2016. **229**: p. 80-107.
177. Liu, H., et al., *Etching-Free Epitaxial Growth of Gold on Silver Nanostructures for High Chemical Stability and Plasmonic Activity*. Advanced Functional Materials, 2015. **25**(34): p. 5435-5443.
178. Sun, M., et al., *A flexible conductive film prepared by the oriented stacking of Ag and Au/Ag alloy nanoplates and its chemically roughened surface for explosive SERS detection and cell adhesion*. RSC Advances, 2017. **7**(12): p. 7073-7078.
179. Li, J., et al., *Bifunctional Ag@ Pd-Ag nanocubes for highly sensitive monitoring of catalytic reactions by surface-enhanced Raman spectroscopy*. Journal of the American Chemical Society, 2015. **137**(22): p. 7039-7042.
180. Chen, L., J.M. Chabu, and Y. Liu, *Bimetallic AgM (M= Pt, Pd, Au) nanostructures: synthesis and applications for surface-enhanced Raman scattering*. RSC Advances, 2013. **3**(13): p. 4391-4399.
181. Lee, C.-L. and C.-M. Tseng, *Ag- Pt Nanoplates: Galvanic Displacement Preparation and Their Applications As Electrocatalysts*. The Journal of Physical Chemistry C, 2008. **112**(35): p. 13342-13345.
182. He, W., et al., *Formation of AgPt alloy nanoislands via chemical etching with tunable optical and catalytic properties*. Langmuir, 2009. **26**(6): p. 4443-4448.
183. Aherne, D., et al., *From Ag nanoprisms to triangular AuAg nanoboxes*. Advanced Functional Materials, 2010. **20**(8): p. 1329-1338.
184. Zhang, Q., et al., *Synthesis of Ag@ AgAu metal core/alloy shell bimetallic nanoparticles with tunable shell compositions by a galvanic replacement reaction*. small, 2008. **4**(8): p. 1067-1071.
185. He, W., et al., *Design of AgM bimetallic alloy nanostructures (M= Au, Pd, Pt) with tunable morphology and peroxidase-like activity*. Chemistry of Materials, 2010. **22**(9): p. 2988-2994.
186. Wang, L. and Y. Yamauchi, *Strategic synthesis of trimetallic Au@ Pd@ Pt core- shell Nanoparticles from poly (vinylpyrrolidone)-based aqueous solution toward highly active electrocatalysts*. Chemistry of Materials, 2011. **23**(9): p. 2457-2465.
187. Lee, Y.W., et al., *Synthesis and characterization of flower-shaped porous Au- Pd alloy nanoparticles*. The Journal of Physical Chemistry C, 2008. **112**(17): p. 6717-6722.
188. He, S., et al., *Biosynthesis of gold nanoparticles using the bacteria Rhodospseudomonas capsulata*. Materials Letters, 2007. **61**(18): p. 3984-3987.
189. Chen, J., et al., *Optical properties of Pd- Ag and Pt- Ag nanoboxes synthesized via galvanic replacement reactions*. Nano letters, 2005. **5**(10): p. 2058-2062.
190. Lin, Y., J. Ren, and X. Qu, *Catalytically active nanomaterials: a promising candidate for artificial enzymes*. Accounts of chemical research, 2014. **47**(4): p. 1097-1105.
191. Singh, S., *Cerium oxide based nanozymes: Redox phenomenon at biointerfaces*. Biointerphases, 2016. **11**(4): p. 04B202.
192. Singh, R., et al., *Redox-sensitive cerium oxide nanoparticles protect human keratinocytes from oxidative stress induced by glutathione depletion*. Langmuir, 2016. **32**(46): p. 12202-12211.
193. Kotov, N.A., *Inorganic Nanoparticles as Protein Mimics*. Science, 2010. **330**(6001): p. 188-189.
194. Korschelt, K., M.N. Tahir, and W. Tremel, *A Step into the Future: Applications of Nanoparticle Enzyme Mimics*. Chemistry – A European Journal, 2018. **24**(39): p. 9703-9713.
195. Huang, Y., J. Ren, and X. Qu, *Nanozymes: Classification, Catalytic Mechanisms, Activity Regulation, and Applications*. Chemical Reviews, 2019. **119**(6): p. 4357-4412.
196. Hou, J., et al., *Catalyzed and Electrocatalyzed Oxidation of L-Tyrosine and L-Phenylalanine to Dopachrome by Nanozymes*. Nano Letters, 2018. **18**(6): p. 4015-4022.

197. Gao, L., et al., *Intrinsic peroxidase-like activity of ferromagnetic nanoparticles*. Nature nanotechnology, 2007. **2**(9): p. 577.
198. Pirmohamed, T., et al., *Nanoceria exhibit redox state-dependent catalase mimetic activity*. Chemical communications, 2010. **46**(16): p. 2736-2738.
199. Shah, K., et al., *Novel synthesis of polyoxyethylene cholesteryl ether coated Fe-Pt nanoalloys: a multifunctional and cytocompatible bimetallic alloy exhibiting intrinsic chemical catalysis and biological enzyme-like activities*. Colloids and Surfaces A: Physicochemical and Engineering Aspects, 2018. **553**: p. 50-57.
200. Zhang, K., et al., *Formation of PdPt alloy nanodots on gold nanorods: tuning oxidase-like activities via composition*. Langmuir, 2011. **27**(6): p. 2796-2803.
201. Wei, H. and E. Wang, *Fe₃O₄ magnetic nanoparticles as peroxidase mimetics and their applications in H₂O₂ and glucose detection*. Analytical Chemistry, 2008. **80**(6): p. 2250-2254.
202. Vallabani, N.S., A.S. Karakoti, and S. Singh, *ATP-mediated intrinsic peroxidase-like activity of Fe₃O₄-based nanozyme: One step detection of blood glucose at physiological pH*. Colloids and Surfaces B: Biointerfaces, 2017. **153**: p. 52-60.
203. Singh, R. and S. Singh, *Redox-dependent catalase mimetic cerium oxide-based nanozyme protect human hepatic cells from 3-AT induced acatalasemia*. Colloids and Surfaces B: Biointerfaces, 2019. **175**: p. 625-635.
204. Singh, S., *Nanomaterials exhibiting enzyme-like properties (Nanozymes): Current advances and future perspectives*. Frontiers in chemistry, 2019. **7**: p. 46.
205. Karim, M.N., et al., *Nanostructured silver fabric as a free-standing NanoZyme for colorimetric detection of glucose in urine*. Biosensors and Bioelectronics, 2018. **110**: p. 8-15.
206. Gharib, M., et al., *Protein-Protected Porous Bimetallic AgPt Nanoparticles with pH-Switchable Peroxidase/ Catalase-Mimicking Activity*. ACS Materials Letters, 2019. **1**: p. 310-319.
207. Smith, J.G., I. Chakraborty, and P.K. Jain, *In Situ Single-Nanoparticle Spectroscopy Study of Bimetallic Nanostructure Formation*. Angewandte Chemie International Edition, 2016. **55**(34): p. 9979-9983.
208. Kumar-Krishnan, S., et al., *A general seed-mediated approach to the synthesis of AgM (M= Au, Pt, and Pd) core-shell nanoplates and their SERS properties*. RSC Advances, 2017. **7**(44): p. 27170-27176.
209. Han, S., et al., *The alloying effect and AgCl-directing growth for synthesizing a trimetallic nanoring with improved SERS*. Nanoscale, 2015. **7**(48): p. 20414-20425.
210. Bujacz, A., *Structures of bovine, equine and leporine serum albumin*. Acta Crystallographica Section D, 2012. **68**(10): p. 1278-1289.
211. Peters Jr, T., *All about albumin: biochemistry, genetics, and medical applications*. 1995: Academic press.
212. Wright, A. and M. Thompson, *Hydrodynamic structure of bovine serum albumin determined by transient electric birefringence*. Biophysical Journal, 1975. **15**(2 Pt 1): p. 137-141.
213. Brewer, S.H., et al., *Probing BSA Binding to Citrate-Coated Gold Nanoparticles and Surfaces*. Langmuir, 2005. **21**(20): p. 9303-9307.
214. Gambinossi, F., S.E. Mylon, and J.K. Ferri, *Aggregation kinetics and colloidal stability of functionalized nanoparticles*. Advances in colloid and interface science, 2015. **222**: p. 332-349.
215. Aiuchi, T., S. Nakajo, and K. Nakaya, *Reducing activity of colloidal platinum nanoparticles for hydrogen peroxide, 2, 2-diphenyl-1-picrylhydrazyl radical and 2, 6-dichlorophenol indophenol*. Biological and Pharmaceutical Bulletin, 2004. **27**(5): p. 736-738.
216. Anan'ev, A., et al., *Catalytic decomposition of hydrazine in weakly alkaline solutions on platinum nanoparticles*. Radiochemistry, 2004. **46**(6): p. 578-582.

217. Mochida, I. and K. Takeshita, *Transition metal ions on molecular sieves. II. Catalytic activities of transition metal ions on molecular sieves for the decomposition of hydrogen peroxide*. The Journal of Physical Chemistry, 1974. **78**(16): p. 1653-1657.
218. Kitajima, N., S. Fukuzumi, and Y. Ono, *Formation of superoxide ion during the decomposition of hydrogen peroxide on supported metal oxides*. The Journal of Physical Chemistry, 1978. **82**(13): p. 1505-1509.
219. Liu, X., et al., *BSA-templated MnO₂ nanoparticles as both peroxidase and oxidase mimics*. Analyst, 2012. **137**(19): p. 4552-4558.
220. Mu, J., et al., *Co₃O₄ nanoparticles as an efficient catalase mimic: Properties, mechanism and its electrocatalytic sensing application for hydrogen peroxide*. Journal of Molecular Catalysis A: Chemical, 2013. **378**: p. 30-37.
221. Asati, A., et al., *Oxidase-like activity of polymer-coated cerium oxide nanoparticles*. Angewandte Chemie International Edition, 2009. **48**(13): p. 2308-2312.
222. Stierle, A., et al., *DESY NanoLab*. Journal of large-scale research facilities, 2016. **2**: p. A76.
223. Micsonai, A., et al., *BeStSel: a web server for accurate protein secondary structure prediction and fold recognition from the circular dichroism spectra*. Nucleic Acids Research, 2018. **46**(W1): p. 315-322.
224. Halfman, C.J. and T. Nishida, *Influence of pH and electrolyte on the fluorescence of bovine serum albumin*. Biochimica et Biophysica Acta (BBA)-Protein Structure, 1971. **243**(2): p. 284-293.
225. Halfman, C.J. and T. Nishida, *Nature of the alteration of the fluorescence spectrum of bovine serum albumin produced by the binding of dodecyl sulfate*. Biochimica et Biophysica Acta (BBA)-Protein Structure, 1971. **243**(2): p. 294-303.
226. Steinhardt, J., J. Krijn, and J.G. Leidy, *Differences between bovine and human serum albumins. Binding isotherms, optical rotatory dispersion, viscosity, hydrogen ion titration, and fluorescence effects*. Biochemistry, 1971. **10**(22): p. 4005-4015.
227. Orendorff, C.J. and C.J. Murphy, *Quantitation of Metal Content in the Silver-Assisted Growth of Gold Nanorods*. J. Phys. Chem. B, 2006. **110**(9): p. 3990-3994.
228. Luo, Z., et al., *From aggregation-induced emission of Au (I)-thiolate complexes to ultrabright Au (0)@ Au (I)-thiolate core-shell nanoclusters*. Journal of the American Chemical Society, 2012. **134**(40): p. 16662-16670.
229. Stöber, W., A. Fink, and E. Bohn, *Controlled growth of monodisperse silica spheres in the micron size range*. Journal of colloid and interface science, 1968. **26**(1): p. 62-69.
230. Bastus, N.G., J. Comenge, and V. Puntes, *Kinetically Controlled Seeded Growth Synthesis of Citrate-Stabilized Gold Nanoparticles of up to 200 nm: Size Focusing versus Ostwald Ripening*. Langmuir, 2011. **27**(17): p. 11098-11105.
231. Yuan, H., et al., *Gold nanostars: surfactant-free synthesis, 3D modelling, and two-photon photoluminescence imaging*. NANOTECHNOLOGY, 2012. **23**(7).
232. Jin, R., et al., *Controlling anisotropic nanoparticle growth through plasmon excitation*. Nature, 2003. **425**: p. 487-490.
233. Feliu, N., et al., *Nanoparticle dosage-a nontrivial task of utmost importance for quantitative nanosafety research*. Wiley Interdiscip Rev Nanomed Nanobiotechnol, 2016. **8**: p. 479-492.
234. Weisstein, E.W. *Heron's formula*. MathWorld--A Wolfram Web Resource 2003; Available from: <http://mathworld.wolfram.com/HeronsFormula.html>.

Acknowledgements

I am really grateful to many wonderful people who have been always standing by me during my PhD.

I would like to thank in the first place Prof. Dr. Wolfgang Parak who gave me the freedom to explore interesting paths and exciting research directions during my PhD in his group. His instructive guidance, illuminating suggestions and kind advice really encouraged me throughout the PhD.

I would like also to thank Prof. Dr. Alf Mews for being my co-supervisor.

I am sincerely grateful to my mentor Dr. Indranath Chakraborty for suggesting the plane of this work as well as his continuous guidance and support, valuable suggestions and helpful discussions throughout the entire course of the PhD.

As successful and great work could not be pursued without great colleagues. I would like to thank all the current and former members of the Biophotonik group, especially the ones with whom I have worked, collaborated, shared science, and those who helped me along the PhD journey. I am very grateful to my office mates with whom I have unforgettable moments and nice and cheerful atmosphere.

A special thanks is due to all collaborators without whom this work would not have been brought to completion. I would like to take advantage of this opportunity to thank Anna Rosa Ziefuß, Dr. Christoph Rehbock, Prof. Dr. Stephan Barcikowski who I collaborated with at the University of Duisburg-Essen to explore the photothermal behavior of my gold nanorods project. I acknowledge the work of Ms. Marta Gallego Gonzalez from CIC Biomagune and Mr. Andreas Kornowski from the chemistry department, Universität Hamburg for their assistance in recording the TEM, STEM images and elemental EDX mapping of the nanoparticles used in this work. I thank Dr. Heshmat Noei from DESY NanoLab and Dr. Nonappa from Aalto University for their assistance in acquiring and

interpreting the XPS and 3D TEM data. I am also acknowledge the contribution of the undergraduate student Johannes Gebauer to the gold nanorods work.

Special thanks to Prof. Dr. Alaaldin Alkilany from school of Pharmacy, the University of Jordan as well as my colleague Saad Megahed for their helpful discussion and endless support and encouragement. I have truly been blessed with the opportunity being with you throughout my entire PhD.

I thank my entire family especially my parents from the bottom of my heart for their continuous encouragement and support, I would not have been go that far without them being standing by me.

I register my sincere appreciation to the PIER Helmholtz Graduate School for giving me the opportunity to develop my academic and research skills through their amazing workshops and courses. I do really acknowledge their financial support as well that enabled me to travel abroad for joining one of the international conferences.

I am incredibly grateful to the German Academic Exchange Service (DAAD 'Deutscher Akademischer Austauschdienst') and the Ministry of Higher Education and Scientific Research for generously granting me the GERLS scholarship without which this work would not have been possible. I will never be thankful enough to them for the financial support throughout the entire PhD.